

A simulation of ^{14}C synchronicity for the Laacher See volcanic eruption and hypothesized Younger Dryas extraterrestrial impact

Supplemental Information Appendix

Ian A. Jorgeson, Ryan P. Breslawski, Abigail E. Fisher

[Contents](#)

1.	Detailed Description of Simulation Steps	2
2.	Guide to Running the Simulation.....	11
3.	Laboratory Measurement Bias and Repeatability Model (LBM)	13
4.	Site and ^{14}C Sample Selection for the YDB and LST.....	24
5.	Simulations of Alternative Dataseto	30
6.	References for Supplemental Information Appendix	51

1. Detailed Description of Simulation Steps

The main paper provides a general outline of the simulation, while this section describes the simulation steps in detail. A more detailed overview of the simulation can be obtained by downloading the R script and the comments contained within. Section 2 provides instructions for running this script.

The simulation is performed for unique events e . Here, e corresponds to either the hypothesized Younger Dryas Impact or the Laacher See Volcanic Eruption. For each event e , we performed the simulation for 10,000 iterations in each year $x_{e,i}$ in a vector x_e of calendar years. For the former event, we used dates corresponding to the purported Younger Dryas Boundary (YDB), and for the latter event we used dates associated with the Laacher See Tephra (LST). For the YDB, x_{YDB} spans 151 years within 12,860—12,710 cal BP, and for the LST, x_{LST} spans 151 years within 12,991—12,841 cal BP. The central 101 years in each x_e corresponds to a range of possible calendar years for each hypothesized event. We simulated over a 25-year buffer on each side of the hypothesized range to observe how expectations vary for calendar years proximate to the possible calendar years for each hypothesized event.

For each of the 10,000 iterations in year $x_{e,i}$, the simulation performs four main steps:

- (1) A vector of true calendar ages C is selected for the synchronous event. The length of C depends on the number of ^{14}C measurements in the observed sample (30 for the YDB and 19 for the LST).
- (2) Expected target ^{14}C values are generated for each calendar age in C .
- (3) For each target ^{14}C value, an expected ^{14}C value as *measured* by a laboratory is generated.
- (4) Each measured ^{14}C value is calibrated with the IntCal13 ^{14}C calibration curve (1).

The remainder of this section describes each of the four steps. These descriptions concern a single iteration for a single calendar age $x_{e,i}$. To help illustrate these steps, Table S1.1 provides a toy set of reported ^{14}C measurements that could be used as simulation input for a hypothetical synchronous event. We expand on this table with each simulation step. All references to “calendar ages/years/dates” indicate years BP. AMS refers to accelerator mass spectrometry, GPC refers to gas proportional counting, and LSC refers to liquid scintillation counting.

1.1. True Calendar Ages

For each iteration within calendar year $x_{e,i}$, a vector of repeating $x_{e,i}$ values is first generated. The length of this vector is determined by the existing ^{14}C datasets for each event. The YDB dataset consists of 30 reported dates, which creates a vector of 30 $x_{e,i}$ values for these simulations. The corresponding LST vector length is 19. For simulations that lack “old wood” effects, these repeated vectors are treated as the true calendar ages for each simulated ^{14}C measurement.

Some versions of the simulation account for “old wood” effects with an “old wood” model (OWM). These versions add a calendar year offset to each $x_{e,i}$. Additional years are added only to the $x_{e,i}$ values that correspond to dated materials from organisms that may have died prior to the event of interest. 24 of 30 reported YDB dates originate from such materials, and 18 of 19 reported LST dates correspond to these materials. Short-lived samples, such as those from grasses or seeds, do not receive age offsets. The new vector of calendar years that includes offset values is referred to here as x_e^o (Table S1.2).

Table S1.1. A toy dataset of reported ^{14}C measurements for five samples associated with a hypothesized event e. These measurements were made by three laboratories with codes ABCD, EFGH, and IJKLM. The first and last laboratories measure ^{14}C via AMS, while EFGH measures ^{14}C via GPC. Three of the five measurements are on wood, indicating that they may correspond to calendar ages older than the event of interest. The simulation generates expected ^{14}C values (i.e., what might be observed in the μ column given a true synchronous event), while all other columns in this table provide context dependent input for the simulation itself.

Sample ID	Reported ^{14}C		“old wood”?	Lab type
	μ	σ		
ABCD-0001	10,251	25	No (seed)	AMS
ABCD-0002	10,290	35	No (seed)	AMS
EFGH-0001	10,295	75	Yes (wood)	GPC
EFGH-0003	10,299	55	Yes (wood)	GPC
IJKLM-0001	10,321	40	Yes (wood)	AMS

OWM age offsets are drawn randomly from an exponential distribution, with offsets near zero more likely. In other words, OWM offsets assume that organism death most likely occurred shortly before the calendar year of the event e, with the probability of an earlier death event decreasing with temporal distance from event e. We considered two exponential distributions, one with the λ parameter set to 0.04 and one with λ set to 0.01 (Figure S1.1). The former distribution is a conservative scenario in which old samples predate the event by few years ($\mu = 25$, 95% HDI = 0–75), while the latter distribution results in larger age offsets on average ($\mu = 100$, 95% HDI = 0–300; Figure S1.1b,c). New values are drawn from each exponential distribution for each of the 10,000 iterations, allowing for λ specific variability in “old wood” effects to be estimated across 10,000 iterations. These distributions were selected to bound the extremes of realistic offsets that might be expected given “old wood” effects.

Table S1.2. The initial step in a single simulation iteration. Here, the toy dataset is used as input for a simulation iteration at 12,000 cal BP. The reported ^{14}C means have been removed, as these do not serve as input for the simulation. The age offsets are shown for hypothetical values drawn from an exponential distribution with $\lambda = 0.04$.

Sample ID	Reported ^{14}C		“old wood”?	Lab type	$x_{e,i}$	Offset	$x_{e,i}^o$
	μ	σ					
ABCD-0001	-	25	No	AMS	12,000	N/A	12,000.0
ABCD-0002	-	35	No	AMS	12,000	N/A	12,000.0
EFGH-0001	-	75	Yes	GPC	12,000	27.5	12,027.5
EFGH-0003	-	55	Yes	GPC	12,000	6.1	12,006.1
IJKLM-0001	-	40	Yes	AMS	12,000	88.5	12,088.5

Most of the wood samples for Laacher See are *Populus* (2), which is most likely Eurasian aspen (*Populus tremula*) or black poplar (*Populus nigra*). The former species lives an average of 50-100 years (3) and can live up to 200 years (4). In contrast, black poplar generally live only 20-50 years. As such, the conservative exponential model ($\lambda = 0.04$) generally gives offsets intermediate between the lifespans of these species (Figure S1.1b). The latter “old wood” exponential function ($\lambda = 0.01$) is more consistent with aspen and produces occasional offsets several centuries older than the lifespan of aspen (Figure S1.1c). This can accommodate scenarios in which dead wood on the landscape is incorporated into the geological stratum of

interest. We assume that true “old wood” effects for the YDB and LST wood and charcoal ^{14}C samples fall somewhere between the two extremes defined by these exponential functions, and neither exponential function is intended to match precisely the “old wood” effects in either context, which are probably unknowable.

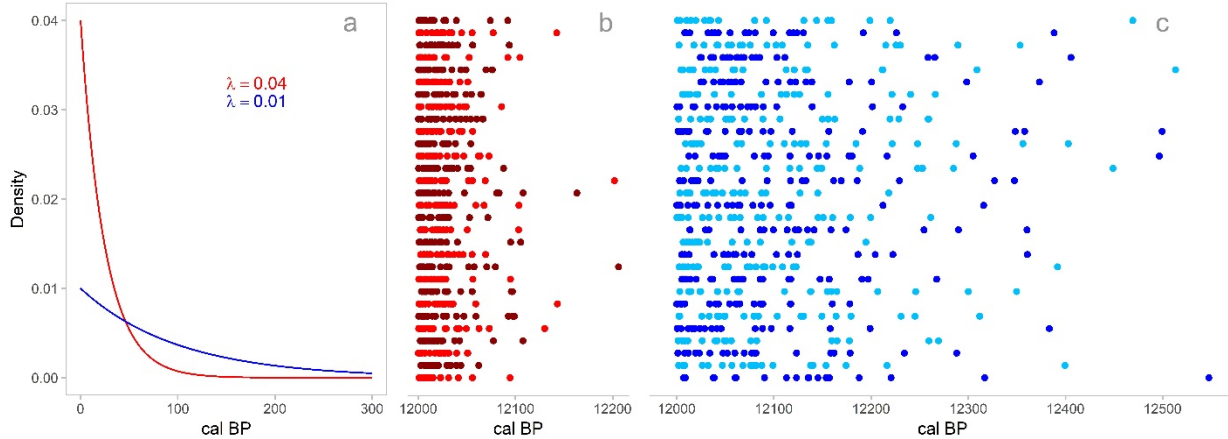


Figure S1.1. Exponential distributions used for versions of the simulation employing an OWM. (a) Probability density functions for each offset. (b and c) 30 examples of 20 “old wood” dates for a synchronous event at 12,000 cal BP, where each row is a sample of 20 dates. Panel b corresponds to an exponential distribution with $\lambda = 0.04$, and panel c corresponds to an exponential distribution with $\lambda = 0.01$.

1.2. Target ^{14}C Values

We generated a target ^{14}C value for each $x_{e,i}^0$ value in two steps. First, mean ^{14}C values were obtained by “uncalibrating” $x_{e,i}^0$ values with the *uncalibrate* function in the *rcarbon* R package (5). This function works by drawing from a normal distribution of ^{14}C values associated with a calendar year, where the distribution corresponds to the calibration curve error in the IntCal13 ^{14}C calibration curve (Figure S1.2a). This produces a hypothetical mean atmospheric ^{14}C value for the calendar year (Table S1.3). $x_{e,i}^0$ that share identical values receive the same uncalibrated mean atmospheric ^{14}C value since they correspond to a calendar year with the same hypothetical mean atmospheric ^{14}C value. Mean atmospheric ^{14}C values are resampled for each of the 10,000 iterations.

Second, we account for intra-annual variability around the mean atmospheric ^{14}C value in a calendar year. We estimated the difference between seasonal extremes of atmospheric ^{14}C variability using data from McDonald et al. (6). They estimate the distance between seasonal extremes of atmospheric ^{14}C with two calculation methods, each of which is performed for situations in which atmospheric ^{14}C production is in increasing and decreasing states (Table S1.4). We also consider stable atmospheric ^{14}C production, treated here as the midpoint between McDonald et al.’s (6) values for increasing and decreasing production.

Table S1.3. The first part of step two for a single simulation iteration. Here, the toy dataset is used as input for a simulation iteration at 12,000 cal BP. The reported ^{14}C means have been removed, as these do not serve as simulation input. Mean atmospheric ^{14}C values have been sampled from the IntCal13 ^{14}C calibration curve error distribution around each calendar age $x_{e,i}^0$.

Sample ID	Reported ^{14}C		“old wood”?	Lab type	$x_{e,i}^0$	Mean atmospheric ^{14}C
	μ	σ				
ABCD-0001	-	25	No	AMS	12,000.0	10,222
ABCD-0002	-	35	No	AMS	12,000.0	10,222
EFGH-0001	-	75	Yes	GPC	12,027.5	10,261
EFGH-0003	-	55	Yes	GPC	12,006.1	10,300
IJKL-0001	-	40	Yes	AMS	12,088.5	10,366

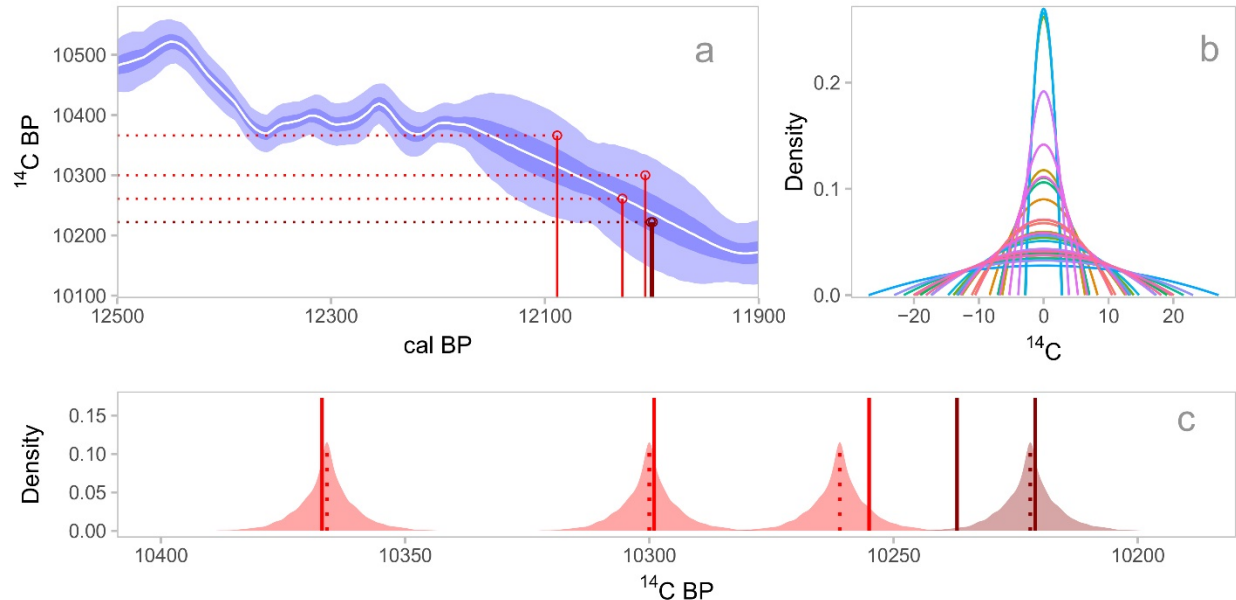


Figure S1.2. A visual schematic of simulated target ^{14}C values based on context dependent input from the toy dataset: (a) “Uncalibrating” five calendar ages (i.e., converting $x_{e,i}^0$ values into mean atmospheric ^{14}C values; Table S1.3 for details). The blue calibration curve bands show the 50% and 95% error regions, and the white line shows the mean value of the curve. (b) 30 randomly sampled beta distributions that represent possible intra-annual distributions of ^{14}C variability. (c) Mean “uncalibrated” ^{14}C values (dotted lines), intra-annual ^{14}C variability around those values based on 10,000 randomly sampled beta distributions (red semitransparent regions), and ^{14}C values sampled from those intra-annual ^{14}C variability distributions (solid lines). The ^{14}C values sampled from each intra-annual distribution comprise the target ^{14}C values. These are the values that laboratories attempt to measure. In panels a and c, light red geometry corresponds to three calendar ages with “old wood” effects, and dark red geometry corresponds to two overlapping calendar ages that date the event of interest.

Table S1.4. Estimates of the intra-annual distance between atmospheric ^{14}C extremes ((6) for increasing and decreasing values. The stable values are the midpoints between the increasing and decreasing values).

Intra-annual distance	Error	Atmospheric ^{14}C trend	Calculation method
18.0	13.0	Increasing	First
23.0	16.0	Decreasing	First
20.5	14.5	Stable	First
26.0	16.0	Increasing	Second
22.0	13.0	Decreasing	Second
24.0	14.5	Stable	Second

To estimate intra-annual atmospheric ^{14}C variability, we first modelled possible values as sparsely beta distributed $\beta(2, 2)$, centered on 0, and scaled by the intra-annual distance. Since the intra-annual distance is imprecisely known, we simulated 10,000 beta distributions scaled by samples drawn from $N(\text{Intra-annual distance}, \text{Error})$ (Figure S1.2b). For each of the 10,000 samples, we randomly selected one of the six possible distance and error pairings. Therefore, these distributions average across atmospheric ^{14}C production trends and calculation methods. For each of the 10,000 simulation iterations, a random value is drawn from one of the 10,000 centered and scaled beta distributions. This random value is then added to the mean atmospheric ^{14}C value to estimate a target ^{14}C value that reflects both inter- and intra-annual ^{14}C variability (Table S1.5; Figure S1.2c).

Table S1.5. The second part of step two for a single simulation iteration. Here, the toy dataset is used as input for a simulation iteration at 12,000 cal BP. The reported ^{14}C means have been removed, as these do not serve as input for the simulation.

Sample ID	Reported ^{14}C		“old wood”?	Lab type	Mean atmospheric ^{14}C	Intra-annual variation offset	Target ^{14}C
	μ	σ					
ABCD-0001	-	25	No	AMS	10,222	15	10,237
ABCD-0002	-	35	No	AMS	10,222	-1	10,221
EFGH-0001	-	75	Yes	GPC	10,261	-6	10,255
EFGH-0003	-	55	Yes	GPC	10,300	-1	10,299
IJKL-0001	-	40	Yes	AMS	10,366	1	10,367

1.3. Measured ^{14}C Values

Given minor inter-laboratory variability that conditions systematic biases, as well as minor instrumental error that shapes intra-laboratory measurement repeatability, measured ^{14}C values depart from their target values (7–12). As such, the dispersion of reported ^{14}C values should vary based on the number of laboratories that have contributed to a reported ^{14}C dataset, as well as based on laboratory specific characteristics that might further influence the repeatability of measurements. These sources of inter- and intra-laboratory variability can be used to model expected departures of ^{14}C measurements from their target values, given known numbers of laboratories and measurements per laboratory.

To estimate this variability, we fit a Bayesian multilevel model to data reported in the Fifth International Radiocarbon Intercomparison (VIRI) (7, 13, 14). We refer to this model as the Laboratory Measurement Bias and Repeatability Model, or LBM. The LBM treats ^{14}C measurements as a normally distributed outcome. We defined a three-parameter linear model for

the outcome mean: a categorical intercept for each sample material, a random categorical effect for laboratory ID, and a scaling parameter that adjusts the random laboratory ID effect based on whether the laboratory performs AMS or GPC/LSC measurements. We defined a four-parameter linear model for the outcome standard deviation. Parameters consist of a baseline intercept, a random categorical effect for laboratory ID, a linear effect for reported measurement error, and a categorical effect that accounts for whether laboratories perform AMS or GPC/LSC measurements. Section 3 describes this model in detail, including the model formula, prior distributions for model parameters, and a posterior predictive check.

The simulation samples 10,000 sets of values from the posterior distributions of the LBM parameters, with a unique set of parameter values applied to each of the 10,000 simulation iterations (Figure S1.3). Therefore, uncertainty in the model parameters is distributed across iterations within each calendar year $x_{e,i}$.

1. A random offset from the target ^{14}C value representing the mean observed value within each laboratory. The number of sampled offsets is determined by the number of laboratories that contributed to the reported ^{14}C dataset (Table S1.6).
2. A multiplier term that rescales the offset for GPC/LSC laboratories (Table S1.6).
3. A random within-laboratory standard deviation that is rescaled by an additional multiplier value for GPC/LSC laboratories (σ_L). This standard deviation further varies by the error reported for each ^{14}C measurement (Table S1.7).
4. Values are then drawn from laboratory and sample specific distributions defined by $N(\text{Mean laboratory specific } ^{14}\text{C}, \sigma_L)$, representing ^{14}C values that might be measured by each laboratory (Table S1.8).

The standard deviation for expected within lab measured ^{14}C variability depends on the reported error of the sample (σ). It takes the form,

$$\sigma_L = \exp(\text{Lab effect} + \text{GPC|LSC effect} + \log(\sigma) * \sigma \text{ effect}) * 100.01. \quad (\text{Equation S1.1})$$

Possible values for each effect are presented in Table S1.7. The 100.01 value to the right of the exponential transformation puts the result on the scale of ^{14}C years (the LBM is fitted to ^{14}C year z-scores, and therefore, the output of this linear model needs to be put back on the ^{14}C year scale).

The measured ^{14}C values comprise an expected set of observations generated for a single iteration. The simulation records the expected standard deviation of these values, $^{14}\text{C}_E^q$ (69.8 for the toy dataset detailed here), as a measure of dispersion for a series of ^{14}C measurements, given a synchronous event. This is completed over 10,000 iterations for each calendar year $x_{e,i}$, yielding a distribution of $^{14}\text{C}_E^q$ given the number of labs, lab types (AMS or GPC/LSC), reported measurement errors, and potential “old wood” effects associated with a reported ^{14}C dataset. For versions of the simulation that exclude the LBM, these $^{14}\text{C}_E^q$ values are calculated with the target ^{14}C values rather than the measured ^{14}C values (as calculated in Step 2).

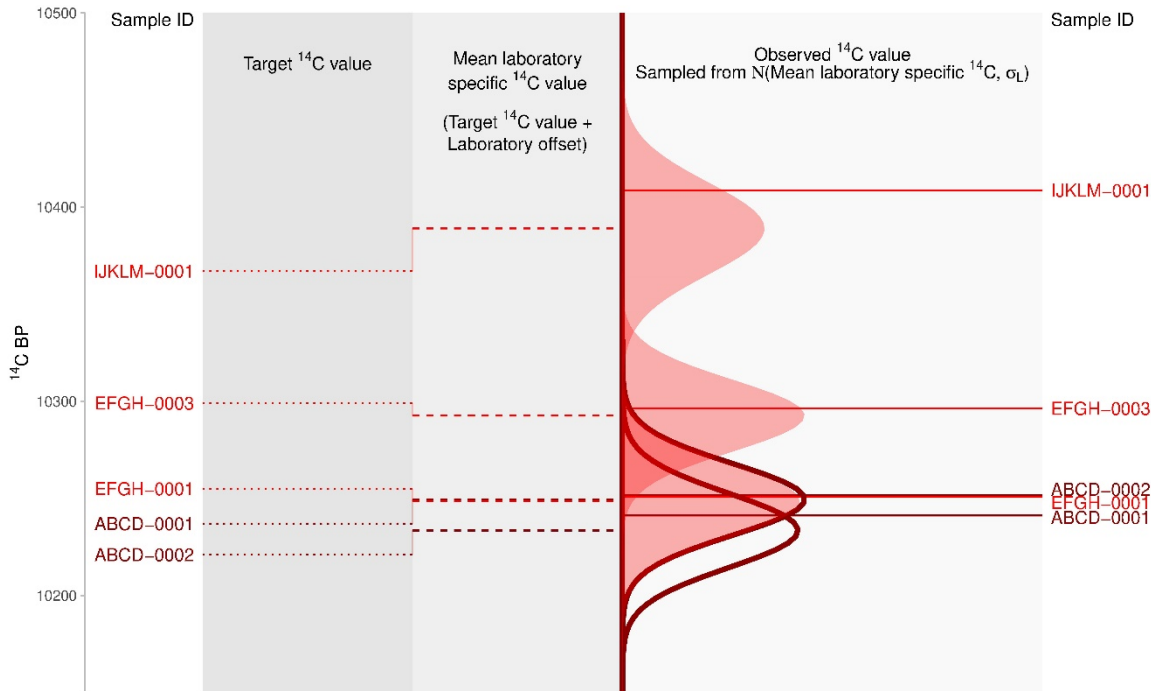


Figure S1.3. An example of five target ^{14}C values being converted to measured ^{14}C values via sampling from the LBM. Refer to Tables S1.6, S1.7, and S1.8 for the values depicted in this figure. Light red lines correspond to three calendar ages with “old wood” effects, and dark red lines correspond to two calendar ages that date the event of interest. Rotated normal distributions illustrate intra-laboratory sampling distributions for each measured ^{14}C value; They correspond to the distribution of repeated measurements for a given laboratory at a given reported measurement error, centered on the mean laboratory specific ^{14}C value for a target ^{14}C value. Two normal distributions with empty fills and dark red outlines depict calendar ages that lack “old wood” effects, and three normal distributions with light red fills and no outlines show calendar ages with “old wood” effects. Note, the intra-laboratory sampling distributions for ABCD-0001 and EFGH-0001 overlap nearly completely, and the values sampled for ABCD-002 and EFGH-0001 are very similar.

Table S1.6. Obtaining mean laboratory offset values for measured ^{14}C in a single simulation iteration. Here, the toy dataset is used as input for a simulation iteration at 12,000 cal BP. The reported ^{14}C means have been removed, as these do not serve as input for the simulation. The laboratory offset and GPC/LSC multiplier values are sampled from the LBM parameters, which vary across the 10,000 simulation iterations.

Sample ID	Reported ^{14}C		Target ^{14}C	Lab offset	GPC LSC multiplier	Mean lab specific ^{14}C
Sample ID	μ	σ	Lab type			
ABCD-0001	-	25	AMS	10,237	12.5	N/A
ABCD-0002	-	35	AMS	10,221	12.5	N/A
EFGH-0001	-	75	GPC	10,255	-5.8	1.1
EFGH-0003	-	55	GPC	10,299	-5.8	1.1
IJKLM-0001	-	40	AMS	10,367	22.0	N/A

Table S1.7. Parameters for sampling measured ^{14}C values. Here, the toy dataset is used as input for a simulation iteration at 12,000 cal BP. The reported ^{14}C means have been removed, as these do not serve as input for the simulation. Laboratory effects, GPC/LSC effects, and σ effects are sampled from the posterior distributions of the LBM parameters, which vary across the 10,000 simulation iterations.

Sample ID	Reported ^{14}C		Lab type	Mean lab specific ^{14}C	Within lab std. deviation (σ_L) parameters		
	μ	σ			Lab effect	GPC LSC effect	σ effect
ABCD-0001	-	25	AMS	10,249.5	-2.1	N/A	0.35
ABCD-0002	-	35	AMS	10,233.5	-2.1	N/A	0.35
EFGH-0001	-	75	GPC	10,248.6	-2.5	0.32	0.35
EFGH-0003	-	55	GPC	10,292.6	-2.5	0.32	0.35
IJKL-0001	-	40	AMS	10,389.0	-1.9	N/A	0.35

Table S1.8. Sampled measured ^{14}C values. Here, the toy dataset is used as input for a simulation iteration at 12,000 cal BP. The reported means have been removed, as these do not serve as input for the simulation. Lab/sample deviations were calculated with the “Within lab std. deviation parameters” from Table S1.7 using Equation S1.1.

Sample ID	Reported ^{14}C		Lab type	Within lab sampling parameters		Measured ^{14}C value
	μ	σ		$^{14}\text{C } \mu$	Std. deviation (σ_L)	
ABCD-0001	-	25	AMS	10,249.5	18.4	10,241.2
ABCD-0002	-	35	AMS	10,233.5	19.1	10,251.7
EFGH-0001	-	75	GPC	10,248.6	18.9	10,250.8
EFGH-0003	-	55	GPC	10,292.6	18.4	10,296.3
IJKL-0001	-	40	AMS	10,389.0	23.6	10,408.6

1.4. Calibrated ^{14}C Measurements

The simulation then calibrates the measured ^{14}C values using the errors described in the reported dataset, producing a probability density across calendar ages for each measurement (Table S1.9; Figure S1.4). This is accomplished with the *calibrate* function in the *rcarbon* R package (5).

Table S1.9. Sampled measured ^{14}C values and the 95% highest density intervals (HDI) for their calibrated age densities. Here, the toy dataset is used as input for a simulation iteration at 12,000 cal BP. The reported means have been removed, as these do not serve as input for the simulation. Note that the measured ^{14}C values in the simulation are calibrated with σ values for the reported measurements.

Sample ID	Reported ^{14}C		Measured ^{14}C		Cal BP (95% HDIs)
	μ	σ	μ	σ	
ABCD-0001	-	25	10,241.2	25	12,111—11,921; 11,915—11,827
ABCD-0002	-	35	10,251.7	35	12,130—11,826
EFGH-0001	-	75	10,250.8	75	12,384—12,264; 12,246—11,711
EFGH-0003	-	55	10,296.3	55	12,386—12,262; 12,249—11,929; 11,894—11,829
IJKL-0001	-	40	10,408.6	40	12,517—12,482; 12,424—12,085

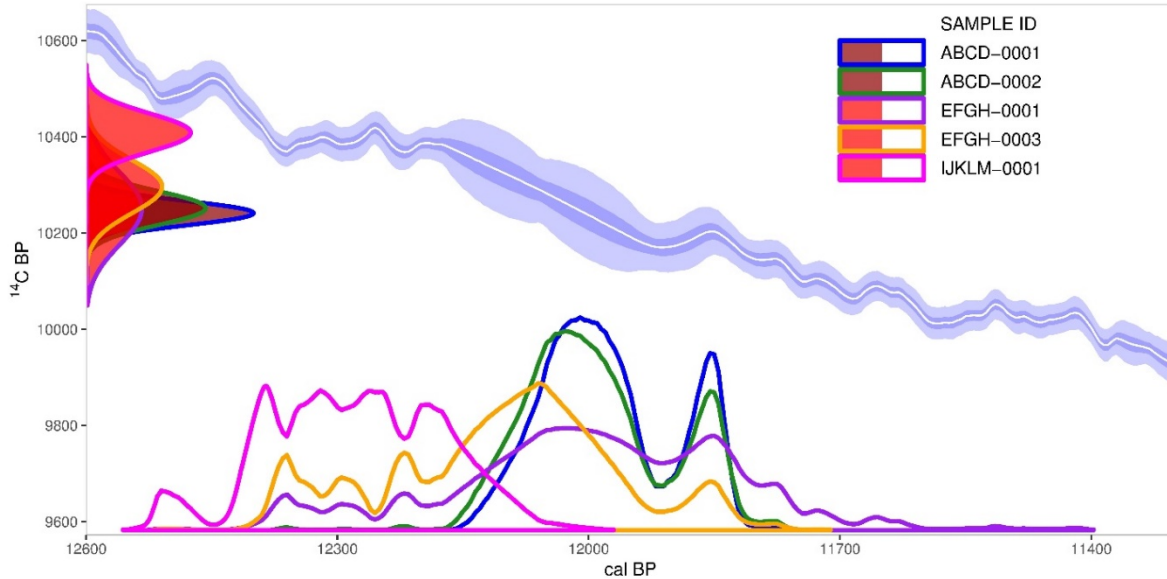


Figure S1.4. Toy dataset: Five expected ^{14}C measurements (rotated normal distributions) calibrated with the IntCal13 calibration curve (white line with blue bands). The blue calibration curve bands show the 50% and 95% error regions and the white line depicts the mean curve value. Light red geometry corresponds to three samples with “old wood” effects, and dark red geometry corresponds to two overlapping samples that date the event of interest. The undulating distributions on the x-axis depict calibrated age densities, which are used to calculate the MPMD.

Following calibration, Manhattan distances are then calculated for each pair of age densities (Table S1.10):

$$\text{Manhattan distance} = \sum_{i=1}^c |A_{x,i} - A_{y,i}|, \quad (\text{Equation S1.2})$$

where $A_{x,i}$ indexes a density value for calendar year i in age density A_x , $A_{y,i}$ indexes a density value in age density A_y for calendar year i , and c is the length of a vector that comprises the union of calendar ages shared by the pair of age densities. The expected Mean Pairwise Manhattan Distance (MPMD_E) is then calculated by taking the mean of all pairwise distances and dividing this mean by two. A value of exactly zero indicates that the age densities are identical, while a value of exactly one indicates that the set of age densities are completely nonoverlapping. Like the $\sigma_{\mu^{14}\text{C}}$ values calculated at the end of Step 3, 10,000 MPMD_E values are obtained for each year $x_{e,i}$ across the iterations.

Table S1.10. Manhattan distances between each pair of the five calibrated age distributions in the toy dataset. The mean of these values is divided by two to obtain the MPMD_E (0.508 for this toy dataset). Here, the toy dataset is used as input for a simulation iteration at 12,000 cal BP.

	ABCD-001	ABCD-002	EFGH-001	EFGH-003	IJKLM-001
ABCD-001					
ABCD-002	0.187				
EFGH-001	0.705	0.618			
EFGH-003	0.946	0.799	0.631		
IJKLM-001	1.860	1.805	1.478	1.136	

2. Guide to Running the Simulation

This simulation consists of an R script that is designed to run on a cluster. Parallelization occurs across the range of simulated years, which is 302 years across the combined events (151 years each for the LST and the YDB). Optimally, one year is assigned per available core, plus one additional core for the master process. If this is accomplished, execution time is mainly limited by the number of simulation iterations. The results in this paper were obtained by executing the R script on the ManeFrame II cluster at Southern Methodist University (SMU), utilizing one core per simulated year. Under these circumstances, a 10,000-iteration simulation completes in about 36 hours, a 1000-iteration simulation completes in just under four hours, and 100 iterations completes in about 0.5 hours. Simulations under 1000 iterations generally provide noisy output distributions of $MPMD_E$ and $^{14}C_E$. If cores are limited and multiple years are run per core, execution time will increase dramatically depending on the core that is assigned the most years over which to simulate (henceforth, maximum-core-years). Estimated execution time is roughly maximum-core-years multiplied by the above specified time estimates. For example, if maximum-core-years is three for a 10,000-iteration simulation on the ManeFrame II cluster, the expected time is 3*36 hours.

2.1. Requirements

RStan: The LBM is fit via Hamiltonian Monte Carlo simulation in Stan (15). Visit <https://www.mc-stan.org> for installation details.

R packages: *ggplot2* (16), *parallel* (17), *reshape2* (18), *rcarbon* (5), *matrixStats* (19), *patchwork* (20), and *rethinking* (21). The first five packages are available in the CRAN.

patchwork is available at: <https://github.com/thomasp85/patchwork>

rethinking is available at: <https://github.com/rmcelreath/rethinking>

Data files: *IRI.csv* (table of reported ^{14}C measurements from the Fifth International Radiocarbon Intercomparison), *RCmeasurements.csv* (table of dates reported for the Laacher See Tephra and Younger Dryas Boundary).

The script must be executed on a cluster with cores distributed across nodes. The main file output (*SimDat#.RData*) for the 10,000-iteration simulation is 587 MB, and there are minor memory spikes during the simulation (intermediate R objects are created during the simulation that are not included in the main output file).

2.2. Running the R Script

Place the R script, *IRI.csv*, and *RCmeasurements.csv* in your working directory. Ensure that RStan and all required packages are installed. Follow these steps:

1. Adjust user-arguments for simulation. Navigate to the ‘USER ARGUMENTS’ block of code in the R script to adjust the simulation as appropriate (code lines 220-305). This block contains variables that specify the number of nodes to be used, the number of cores per node, the number of simulation iterations, plotting options, the ranges of calendar years over which to simulate each event, OWM parameter values, and other variables of interest. Inline code comments further detail each variable.
2. Source the R script. This will load the csv data files and prepare parameters for the simulation. On the first run, the script fits the LBM, which may take 5-15 minutes. After the model is fitted, posterior parameter values are exported in RData file *IRI#.RData* (where # is the number of user-specified iterations for the simulation). If you leave this file in your

working directory and you plan to run the simulation again in the future, the script will read *IRI#.RData* into the simulation rather than refit the model, saving run time. Every time a simulation is run with a new number of iterations (i.e., new # values), the model will be refitted. As such, users can store multiple *IRI#.RData* files for running the simulation with different numbers of iterations. The correct file will be read for each simulation if it has already been generated in the working directory.

3. Monitor the working directory for intermediate output files. In addition to *IRI#.RData*, the script will also output *SimDatIntermediate.RData*. This contains simulation parameters to be read by each node. If you wish to delete this file, do not so until the simulation has initiated on every node (i.e., every node has imported the simulation parameters from *SimDatIntermediate.RData*). Immediately following the creation of *SimDatIntermediate.RData*, the main R script will create daughter R scripts with the filename *NodeSim#.R*. The number of these scripts that is created corresponds to the number of user-specified nodes. After these scripts appear in the working directory, move to Step 4.
4. Submit daughter scripts to the cluster. The main R script also outputs an sbatch array submit script that can be executed to request nodes for every daughter R script (*nodesim.sh*). This is formatted to run on a partition of the ManeFrame II cluster at SMU, but it can be easily edited to run on other clusters using a Slurm workload manager. Alternatively, you may submit the daughter scripts to nodes using your own method.
5. Wait for results. After you submit the daughter scripts, the main R script waits for them to complete (it scans the working directory every 30 seconds for output from the daughter scripts). When a daughter script completes, it outputs *NodeDat#.RData*. After all daughter output files are present in the working directory, the main script automatically imports them, aggregates the results, and creates one output RData file (*SimDat#.RData*, where # is the number of user specified simulation iterations).

2.3. Results and Output Files

Simulation results are contained in objects stored in *SimDat#.RData*. Comments in the script describe these objects. This file is automatically written to the working directory after the simulation completes. *SimDat#.RData* can be opened and explored in an interactive R session on a personal computer. Although the intermediate output files may be of interest (*IRI#.RData*, *SimDatIntermediate.RData*, *NodeDat#.RData*, *NodeSim#.R*, *nodesim.sh*), they do not contain the primary results and may be deleted after the simulation is completed.

3. Laboratory Measurement Bias and Repeatability Model (LBM)

This section has four parts: (1) a description of the Fifth International Radiocarbon Intercomparison (VIRI) dataset to which the LBM was fitted, (2) model formulas and prior distributions for parameters, (3) a description of the posterior parameter values, and (4) a description of Hamiltonian Monte Carlo (HMC) diagnostics with a posterior predictive check. The goal of this model is to estimate parameters that describe inter-lab variation in the measurement of the ^{14}C content of a sample as well as intra-laboratory variation over repeated measurements of a sample. This involves estimating the distributions of mean ^{14}C values and ^{14}C standard deviations across laboratories.

3.1. The VIRI Dataset

To fit the model, we first aggregated data presented in the VIRI (7, 13, 14). These data included all ^{14}C measurements across all sample materials for which ^{14}C measurements were reported (samples B, D, F, G, H, and I). In total, this spans 420 measurements performed by 80 laboratories.

We transformed these data in three steps. First, we centered all ^{14}C measurements on the median value for each sample material. Second, we used these centered measurements to investigate the presence of outliers. Outliers were defined very conservatively as measurements that fall at least six times the distance of the interquartile range (IQR) either below the first or above the third quartile within each set of ^{14}C measurements for a sample material. The values identified as outliers may have resulted from unusually poor quality control for some laboratories or from other anomalies in measurement. After outliers were identified, all measurements associated with the laboratory that produced an outlier were removed from the dataset (Figure S3.1). This reduced the number of laboratories from 80 to 68, and the number of ^{14}C measurements from 420 to 361. Finally, these median-centered measurements were converted to z-scores (Figure S3.1).

3.2. Model Formula and Prior Distributions for Parameters

Each of the 361 median-centered ^{14}C z-scores is associated with four additional variables: a categorical sample material ID (B, D, F, G, H, or I), a categorical laboratory ID, a dummy variable indicating whether than laboratory performed an AMS (0) or GPC/LSC measurement (1), and the reported measurement errors for ^{14}C values. Although measurement errors should represent uncertainty in the reported means, laboratories calculate these errors in a variety of ways that may not be comparable (12). As such, we treat them as predictor variables for the dispersion of reported ^{14}C means, with the expectation that within-laboratory repeatability ^{14}C measurements decreases with larger reported errors.

First, we defined the likelihood for median-centered ^{14}C z-scores as

$$^{14}\text{C} \sim N(\mu, \sigma). \quad (\text{Equation S3.1})$$

Median-centered ^{14}C z-scores are distributed $N(\mu, \sigma)$. We then modelled μ as a linear outcome of the ^{14}C value of sample material i , $C_s[\text{sample } i]$, and an offset from that sample material value that depends on the laboratory ID, $C_o[\text{lab } j]$. The laboratory ID offset also varies based on the AMS vs GPC/LSC dummy variable, AMS, through parameter C_{AMS} :

$$\mu = C_s[\text{sample } i] + C_o[\text{lab } j] \times (1 + (C_{AMS} - 1) \times \text{AMS}). \quad (\text{Equation S3.2})$$

Since median-centered ^{14}C z-scores likely approximate a true sample-specific value near zero, we use a prior distribution of $N(0, 1)$ for each $C_s[\text{sample } i]$. We modelled $C_o[\text{lab } j]$ as distributed $N(0, C_o^\sigma)$, with the prior for C_o^σ set to $\exp(2)$. C_{AMS} may reduce or increase the effect of $C_o[\text{lab } j]$, but it does not affect the sign of $C_o[\text{lab } j]$, taking only positive values. Values less than 1 reduce the lab specific offset $C_o[\text{lab } j]$, while values greater than 1 increase the lab specific offset $C_o[\text{lab } j]$. As such, for C_{AMS} we use a gamma distribution with the mean centered on 1 as a prior: $\text{gamma}(1, 0.5)$. The parameterization of this prior does not follow the base `dgamma` R function, but instead uses the `dgamma2` parameterization included in the *rethinking* R package (22).

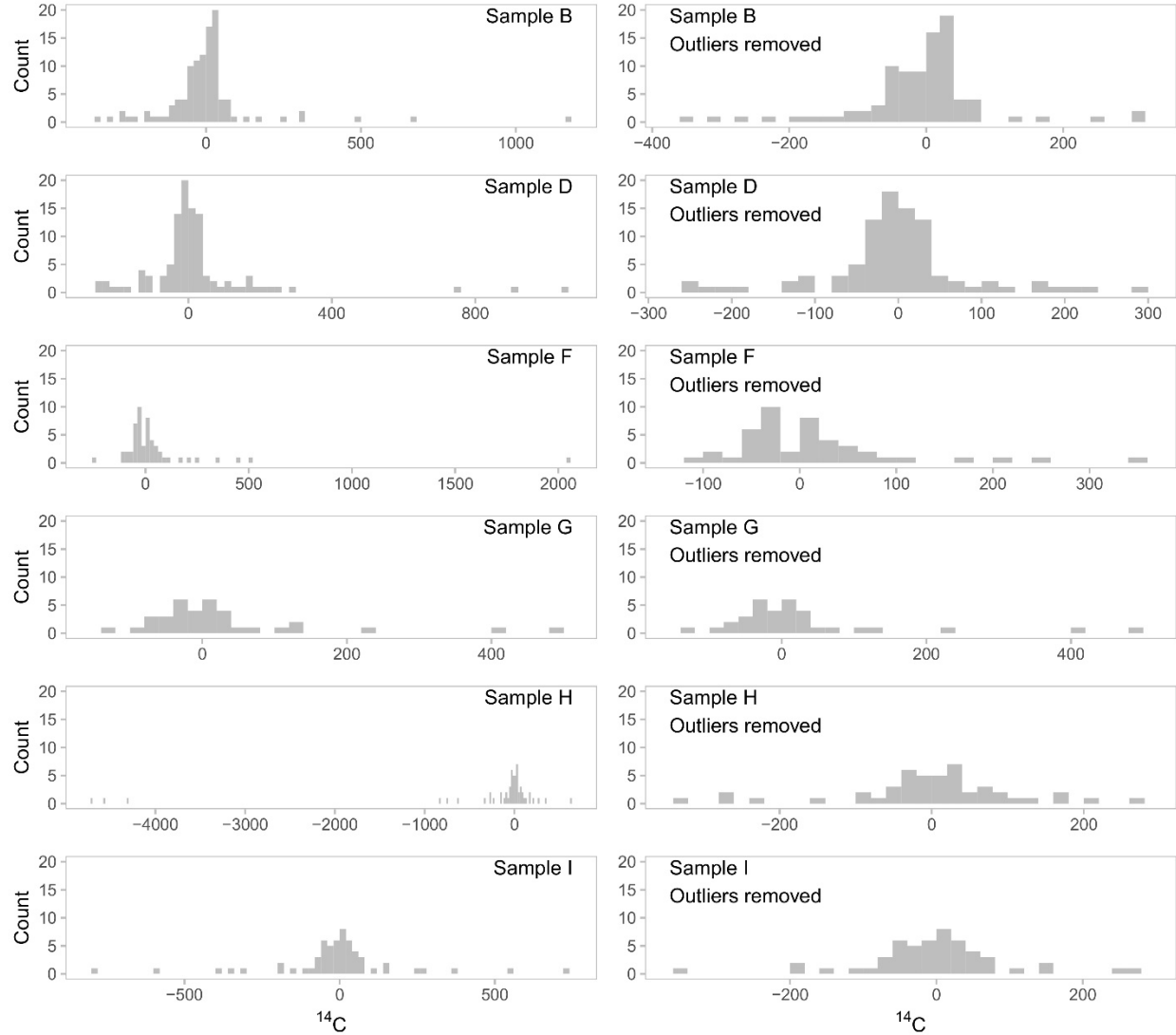


Figure S3.1. Histograms of median-centered ^{14}C z-scores for samples B, D, F, G, H, and I. Left panels show all available measurements ($n = 420$), and right panels show only those measurements that originate from laboratories that did not produce outlier values ($n = 361$). The values in the right panels were used to fit the LBM.

σ can then be interpreted as intra-laboratory variation in median-centered ^{14}C z-scores. We modelled σ as the linear outcome of a baseline parameter shared by all laboratories, σ_l , a laboratory ID specific offset parameter, $\sigma_{\text{lab}}[\text{lab } j]$, the log reported measurement error ($\log(ME)$)

multiplied by parameter σ_{ME} , and a parameter that is expressed only for GPC/LSC laboratories (σ_{AMS}). As such, the dispersion of repeated intra-laboratory ^{14}C z-scores depends on laboratory specific variation in repeatability, the reported measurement error associated with those measurements, and whether the measurement was obtained via AMS or GPC/LSC. Laboratory specific variation depends on each reported ^{14}C measurement error, which can vary from value to value within a single laboratory. To constrain σ on the positive scale, we used a log link function:

$$\log(\sigma) = \sigma_{lab}[lab\ j] + \sigma_l + \sigma_{ME} \times \log(ME) + \sigma_{AMS} \times AMS. \quad (\text{Equation S3.3})$$

We assigned the same informative normal prior distribution to σ_l , σ_l , and σ_{AMS} : $N(0, 1)$. We modelled $\sigma_{lab}[lab\ j]$ as distributed $N(0, \sigma_{lab}^{\sigma})$, with the prior for σ_{lab}^{σ} set to $\exp(2)$. Readers may note that we have not modelled covariance between the random laboratory parameters, $C_0[lab\ j]$ and $\sigma_{lab}[lab\ j]$. For the simulation, the practical implication of this decision is that these parameter values are sampled independently for simulated laboratories rather than from a multivariate distribution. Such covariance is often modelled as multivariate normal, which would be inappropriate here, as σ_{lab} should vary with *only the magnitude* of C_0 rather than the *magnitude and sign* of C_0 (i.e., a parabolic rather than monotonic relationship). In other words, we might expect within-laboratory dispersion to vary with absolute laboratory ID offset, regardless of whether the laboratory ID offset is above or below the target ^{14}C value (Figure S3.2). For the sake of model simplicity and interpretability, we did not attempt to model a parabolic relationship between these parameters.

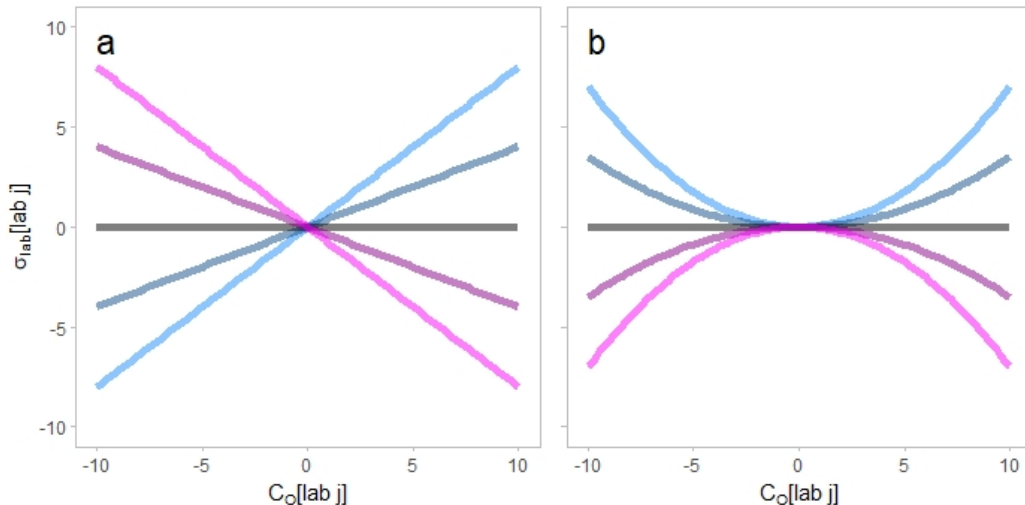


Figure S3.2. (a) Example relationships that might be expected if laboratory parameters covaried monotonically. (b) Example relationships that might be expected given a parabolic relationship between parameters. Given the lack of a covariance component in the model, laboratory parameters were estimated independently, conforming to the horizontal grey relationship in each panel (i.e., no covariance).

This model assumes that systematic offsets between mean laboratory measurements and target ^{14}C values are maintained across any sample materials that a laboratory might measure. For example, consider a laboratory faced with measuring three different sample materials: A, B, and C. If the laboratory takes measurements that are on-average $-10\ ^{14}\text{C}$ years from the target

value of sample A, this mean offset will be also be present when the same laboratory measures the ^{14}C values of sample materials B and C. If the systematic offset varies between sample materials A, B, and C, this cannot be captured by the model. This model also assumes that within-laboratory repeatability is uniform across sample materials A, B, and C. In reality, different sample material types (e.g., bone, wood, grass seeds) and variability in target ^{14}C values may affect both systematic offsets and within-laboratory repeatability. Unfortunately, the available VIRI dataset is insufficient to explore these issues in detail with this model.

The LBM was specified using the *map2stan* function in the *rethinking* R package (22) and fitted through Hamiltonian Monte Carlo (HMC) simulation in RStan (15). The model was fitted with four chains, each of which performed 5000 warmup and 2500 sampling iterations (10,000 total sampling iterations).

3.3. Posterior Parameter Values

Posterior estimates for each sample material ^{14}C value are close to each material's observed sample median (Figure S3.3a). Each posterior distribution for these sample materials includes its respective observed median value in a high-density region (since sample values are median centered, the observed median value is 0 for each distribution). The posterior distribution for C_{AMS} has a mean of 1.26, indicating that GPC/LSC laboratories generally have larger mean offsets from target ^{14}C values than do AMS laboratories (Figure S3.3b). However, this posterior is fairly dispersed, with 36.6% of the distribution falling below 1. Values below 1 correspond to a scenario where GPC/LSC laboratories have smaller mean offsets than those mean offsets associated with AMS laboratories.

The modelled laboratory offset parameters, $C_0[\text{lab } i]$, have mean posterior parameter values ranging from -29.0 to 26.3 ^{14}C years across the 68 laboratories (Table S3.1; Figure S3.4a). These posteriors show high overlap. At first glance, laboratory offset posteriors appear to show that between-laboratory variability is much higher than within-laboratory variability (Figure S3.4). However, this is only in the hypothetical scenario where a laboratory reports 0 measurement error. When measurement error is included, modelled within laboratory σ values increase rapidly and exceed the mean laboratory offsets (Figure S3.5; Figure S3.3e).

Posterior distributions for σ parameters are expressed on the log scale, which makes their combined effects on σ less intuitive to interpret than the previously discussed parameters (Figure S3.5c-e). The posterior for the global parameter for σ , σ_i , has a mean value of 2.8 when this distribution is exponentiated and transformed back into the scale of ^{14}C years (95% HPDI: 0.7—5.6). This represents within-laboratory measurement repeatability for the average AMS laboratory when reported ^{14}C measurement error is zero. When σ_{lab} distributions are added to this average value, within-laboratory repeatability varies between laboratories. For the 68 labs in this dataset, the mean posterior σ value ranges from 1.53 to 9.92 ^{14}C years (Table S3.1). However, these posterior distributions are dispersed and show considerable overlap. In general, the effect of σ_{AMS} causes GPC/LSC laboratories to have higher within-laboratory variability than AMS laboratories (Figure S3.3d; Figure S3.4b; Figure S3.5).

The generative aspect of this model allows one to simulate hypothetical pairs of laboratory parameters (Figure S3.6). As expected, GPC/LSC laboratories have generally larger mean offsets and within-laboratory σ values than AMS laboratories.

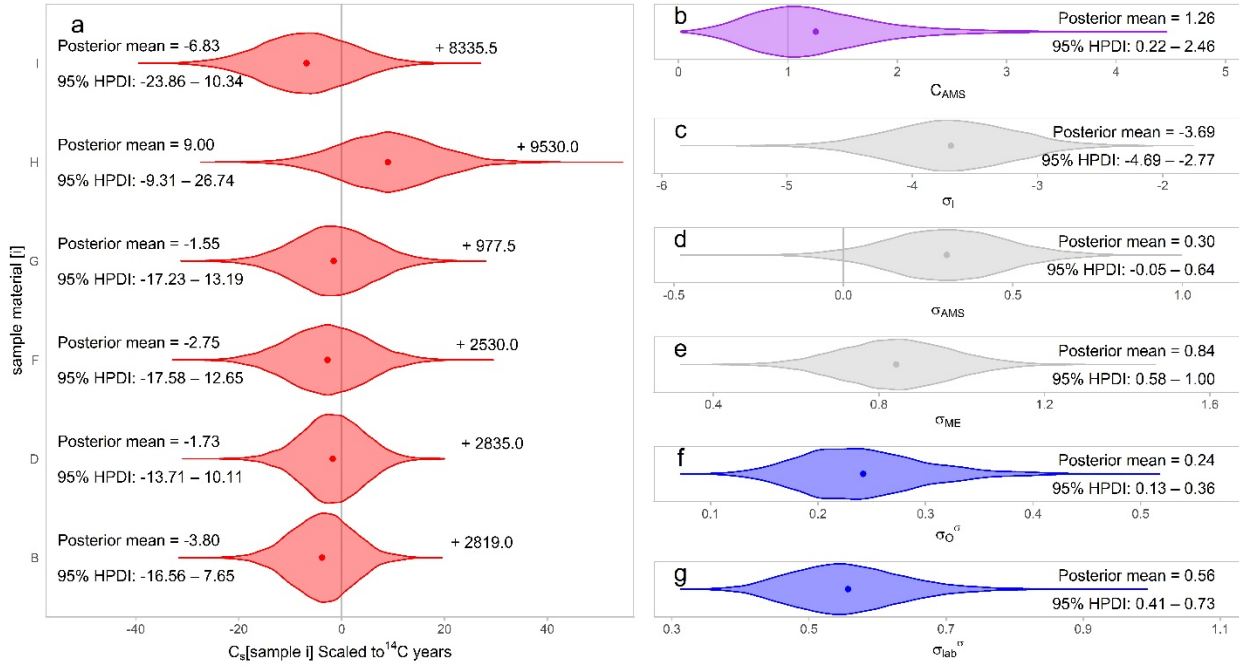


Figure S3.3. Posterior densities, posterior means (dots), and 95% highest posterior density intervals (HPDI) for model parameters. (a) Posteriors for each median-centered sample material. The sample medians are displayed to the right of each density to indicate over which ^{14}C years the non-centered distributions fall. (b) Posterior distribution for C_{AMS} , which adjusts mean laboratory offsets if they are GPC/LSC measurements. Note, most of the density sits above 1, indicating that GPC/LSC laboratory offsets are probably more dispersed than their AMS counterparts. (c-d) Posterior distributions for the standard deviation parameters (σ_l , σ_{AMS} , and σ_{ME}), which are displayed on the log scale. (f-g) Posterior distributions for the standard deviations of the distributions of each laboratory specific parameter, σ_o^σ and σ_{lab}^σ (i.e., mean laboratory-specific offsets and laboratory-specific standard deviations).

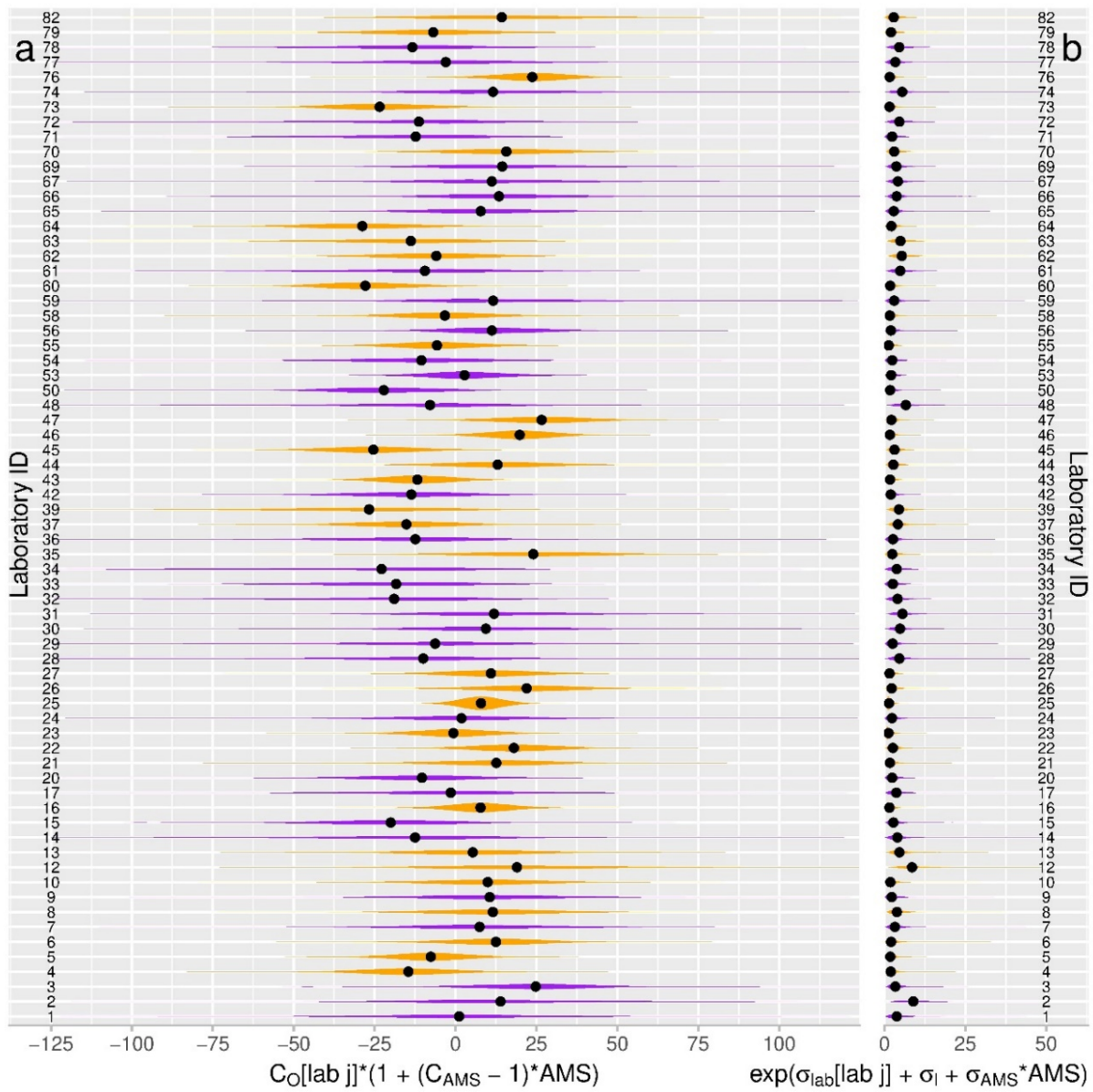


Figure S3.4. Posterior distributions for (a) mean laboratory offsets and (b) within-laboratory standard deviations. Gold densities show AMS laboratories and purple densities show GPC/LSC laboratories. GPC/LSC effects on laboratory offsets and within laboratory standard deviation values are included in these posterior distributions. Black dots mark the medians of each distribution. Note, within-laboratory standard deviations (b) assume 0 reported measurement error, and, in practice, these values become larger (see Figure S3.5). X-axes are on the ^{14}C year scale.

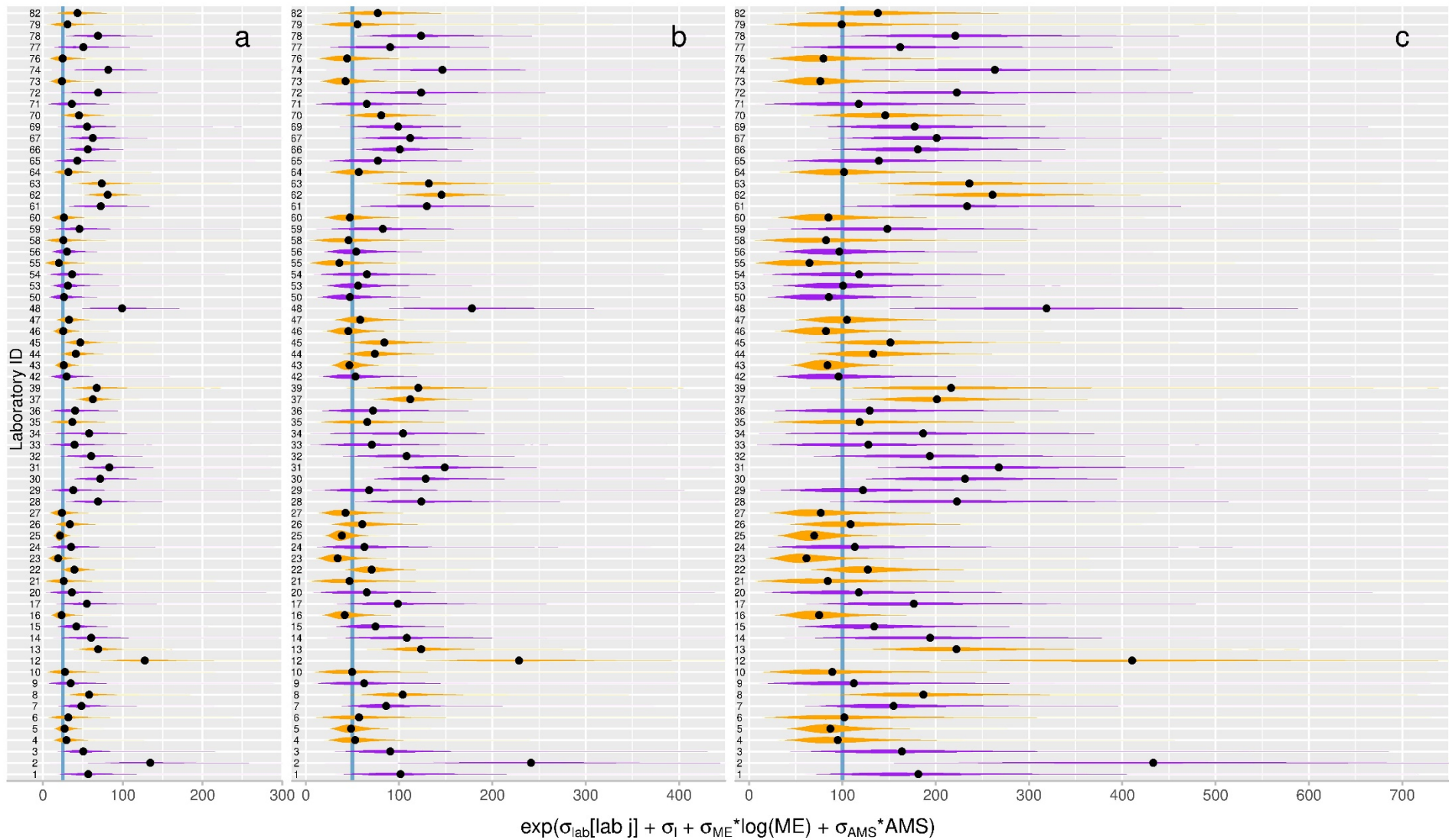


Figure S3.5. Three examples showing how reported measurement error (ME) affects within-laboratory standard deviations: (a) $\text{ME} = 25 \text{ }^{14}\text{C years}$, (b) $\text{ME} = 50 \text{ }^{14}\text{C years}$, and (c) $\text{ME} = 100 \text{ }^{14}\text{C years}$. Vertical blue lines mark the reported error values. Gold posterior densities are AMS laboratories and purple posterior densities are GPC/LSC laboratories. Black dots mark median values in each posterior density. GPC/LSC effects on within-laboratory standard deviations are included in these posterior distributions. X-axes are on the ^{14}C year scale.

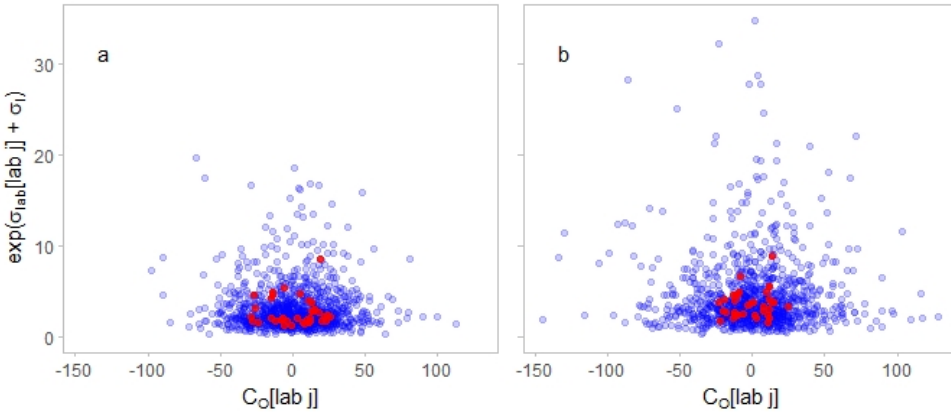


Figure S3.6. Laboratory parameters for (a) AMS and (b) GPC/LSC laboratories. Blue dots show 1000 simulated laboratories and red dots show mean posterior values for laboratories in the VIRI dataset. Both axes are displayed on the ^{14}C year scale.

Table S3.1. Posterior means and 95% highest posterior density intervals (HPDI) for VIRI laboratory parameters. The effects of GPC/LSC measurement methods are excluded here. In other words, all laboratories are treated here as AMS laboratories to express variability that is due to laboratory identity exclusive of ^{14}C measurement method.

Lab. ID [j]	Laboratory mean offset (^{14}C years)	C ₀ [lab j]	Intra-laboratory standard deviation (^{14}C years)
			exp($\sigma_{\text{lab}}[\text{lab j}] + \sigma$)
1	1.27	(-48.45 – 47.78)	3.54 (0.41 – 8.77)
2	14.87	(-38.29 – 71.87)	7.89 (1.44 – 17.99)
3	21.31	(-8.09 – 56.94)	2.88 (0.65 – 6.11)
4	-14.20	(-42.09 – 13.91)	2.32 (0.47 – 5.08)
5	-7.52	(-29.32 – 14.78)	2.09 (0.47 – 4.42)
6	11.97	(-18.54 – 41.52)	2.62 (0.41 – 6.40)
7	7.09	(-31.19 – 49.82)	2.85 (0.48 – 6.37)
8	11.62	(-25.75 – 47.68)	4.54 (0.94 – 9.87)
9	8.95	(-30.30 – 49.86)	2.18 (0.24 – 5.52)
10	9.47	(-27.11 – 45.79)	2.32 (0.25 – 5.59)
12	21.16	(-27.98 – 77.48)	9.92 (2.11 – 21.35)
13	5.61	(-31.05 – 41.74)	5.30 (1.25 – 11.18)
14	-12.61	(-65.43 – 37.58)	3.70 (0.53 – 8.91)
15	-16.92	(-52.35 – 17.87)	2.44 (0.42 – 5.30)
16	7.74	(-10.95 – 26.83)	1.82 (0.35 – 3.92)
17	-1.70	(-51.05 – 46.33)	3.49 (0.41 – 8.72)
20	-8.79	(-44.27 – 26.74)	2.24 (0.19 – 5.50)
21	11.63	(-24.49 – 43.44)	2.19 (0.18 – 5.57)
22	18.04	(-6.20 – 42.05)	3.03 (0.76 – 6.40)
23	-0.60	(-23.73 – 22.72)	1.53 (0.24 – 3.42)
24	2.00	(-38.73 – 45.11)	2.21 (0.20 – 5.35)
25	7.93	(-4.37 – 20.12)	1.60 (0.49 – 3.10)
26	21.80	(-8.74 – 50.63)	2.65 (0.58 – 5.81)
27	10.90	(-17.98 – 41.21)	1.92 (0.37 – 4.29)

28	-9.63	(-58.45 – 39.77)	4.14	(0.78 – 9.69)
29	-6.62	(-55.05 – 43.62)	2.42	(0.22 – 6.21)
30	9.20	(-35.61 – 55.32)	4.28	(0.69 – 9.66)
31	11.28	(-33.59 – 57.48)	4.85	(0.84 – 10.67)
32	-18.65	(-73.86 – 29.13)	3.62	(0.47 – 8.45)
33	-15.23	(-59.45 – 28.70)	2.42	(0.27 – 6.03)
34	-21.21	(-73.84 – 29.64)	3.47	(0.30 – 8.31)
35	23.47	(-17.02 – 63.13)	3.03	(0.33 – 7.25)
36	-10.87	(-54.42 – 29.74)	2.47	(0.33 – 6.01)
37	-15.38	(-45.41 – 15.47)	4.73	(1.16 – 9.54)
39	-29.02	(-84.32 – 20.78)	5.36	(0.81 – 11.78)
42	-11.70	(-46.12 – 24.47)	1.80	(0.26 – 4.24)
43	-11.68	(-32.10 – 9.40)	2.02	(0.44 – 4.22)
44	13.21	(-20.36 – 44.39)	3.24	(0.59 – 7.06)
45	-25.20	(-52.19 – 2.26)	3.59	(0.82 – 7.41)
46	19.72	(-0.37 – 39.30)	1.95	(0.45 – 4.03)
47	26.32	(-1.93 – 52.93)	2.53	(0.53 – 5.38)
48	-8.16	(-59.22 – 40.86)	5.93	(0.94 – 13.58)
50	-18.49	(-51.68 – 12.90)	1.58	(0.20 – 3.61)
53	2.49	(-21.70 – 24.94)	1.82	(0.34 – 3.93)
54	-8.95	(-48.71 – 30.48)	2.26	(0.25 – 5.58)
55	-5.29	(-34.24 – 22.08)	1.67	(0.14 – 4.15)
56	9.84	(-21.37 – 39.56)	1.79	(0.30 – 4.04)
58	-3.11	(-32.11 – 28.43)	2.14	(0.17 – 5.16)
59	11.95	(-35.21 – 61.90)	2.84	(0.29 – 6.99)
60	-26.96	(-53.13 – 0.31)	2.10	(0.37 – 4.65)
61	-9.55	(-58.01 – 39.37)	4.40	(0.62 – 10.24)
62	-6.03	(-38.43 – 26.03)	6.26	(1.31 – 13.27)
63	-14.42	(-60.64 – 27.33)	5.83	(1.07 – 12.76)
64	-28.35	(-60.61 – 6.38)	2.55	(0.44 – 5.71)
65	6.83	(-29.71 – 45.51)	2.62	(0.35 – 6.23)
66	13.15	(-21.49 – 52.30)	3.26	(0.54 – 7.00)
67	10.71	(-34.82 – 57.40)	3.77	(0.62 – 8.79)
69	13.29	(-30.11 – 60.55)	3.29	(0.50 – 7.46)
70	15.81	(-17.36 – 51.36)	3.53	(0.74 – 7.60)
71	-11.08	(-55.76 – 34.09)	2.24	(0.22 – 5.64)
72	-12.08	(-65.29 – 41.20)	4.21	(0.56 – 10.05)
73	-22.75	(-50.96 – 6.54)	1.92	(0.28 – 4.38)
74	12.59	(-38.32 – 67.89)	4.98	(0.68 – 11.78)
76	23.24	(0.83 – 44.15)	1.98	(0.34 – 4.50)
77	-3.51	(-51.84 – 47.22)	3.24	(0.34 – 8.18)
78	-13.89	(-60.91 – 29.29)	4.11	(0.60 – 9.37)
79	-6.77	(-42.76 – 29.40)	2.61	(0.32 – 6.37)
82	15.92	(-33.75 – 69.33)	3.67	(0.40 – 9.18)

3.4. HMC Diagnostics and Posterior Predictive Checks

To ensure convergence of HMC chains, we examined trace plots, R-hat values, and effective sample sizes. Trace plots suggest convergence of HMC chains for all parameters. All R-hat were values are below 1.01. Effective sample sizes close to 10,000 indicate efficient sampling of posterior parameter spaces. Of the 148 parameters, 101 have effective sample sizes of 10,000. The median effective sample size is also 10,000, the mean is 8362, and the minimum is 1056.4 (Figure S3.7).

We also performed a posterior predictive check by simulating data from the model and plotting these simulated data against the VIRI ^{14}C measurements (Figure S3.8). For simplicity, where a laboratory contributed multiple ^{14}C measurements for a given sample material, we used the average reported measurement error for that laboratory ID and sample (for example, laboratories 5 and 22 in the panel for Sample G). In all but nine of the 361 VIRI ^{14}C measurements (97.5%), the 95% prediction intervals overlap the observed values. This indicates that the LBM does a reasonable job recovering the observed values.

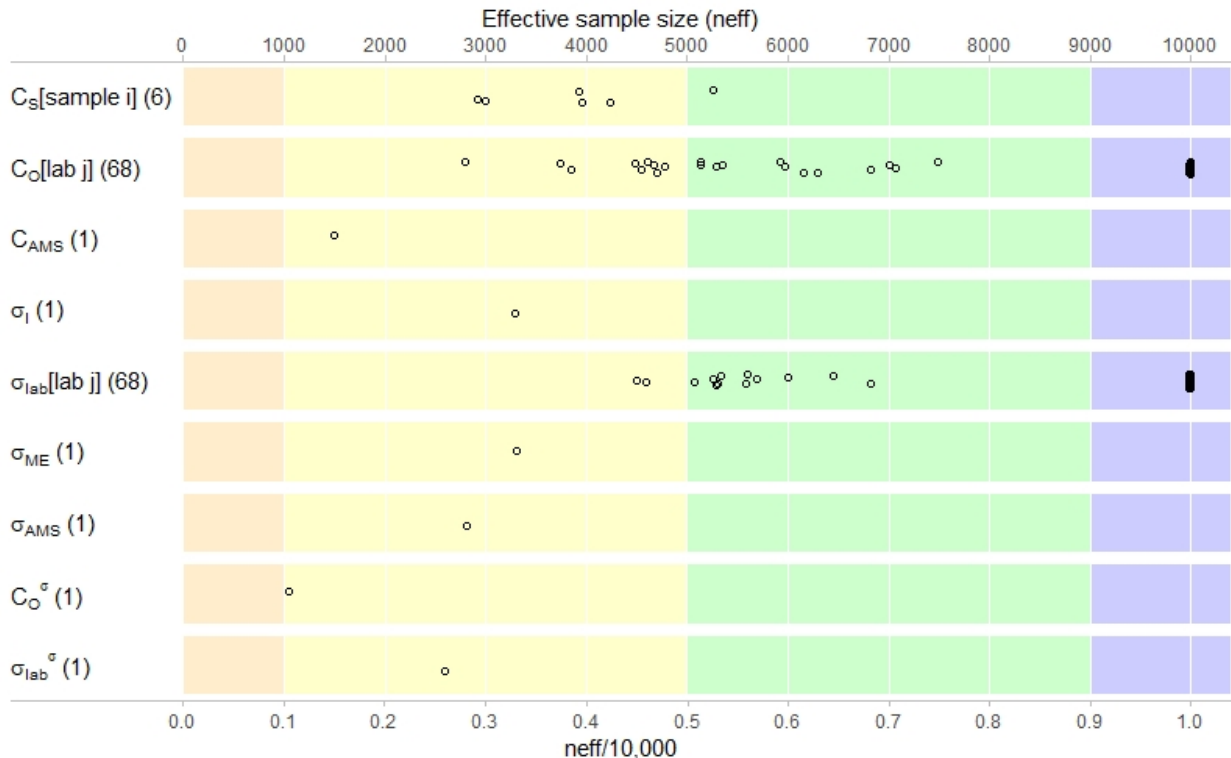


Figure S3.7. Distribution of effective sample sizes across parameters. Parenthetical values show the number of parameter distributions that were sampled for each parameter type.

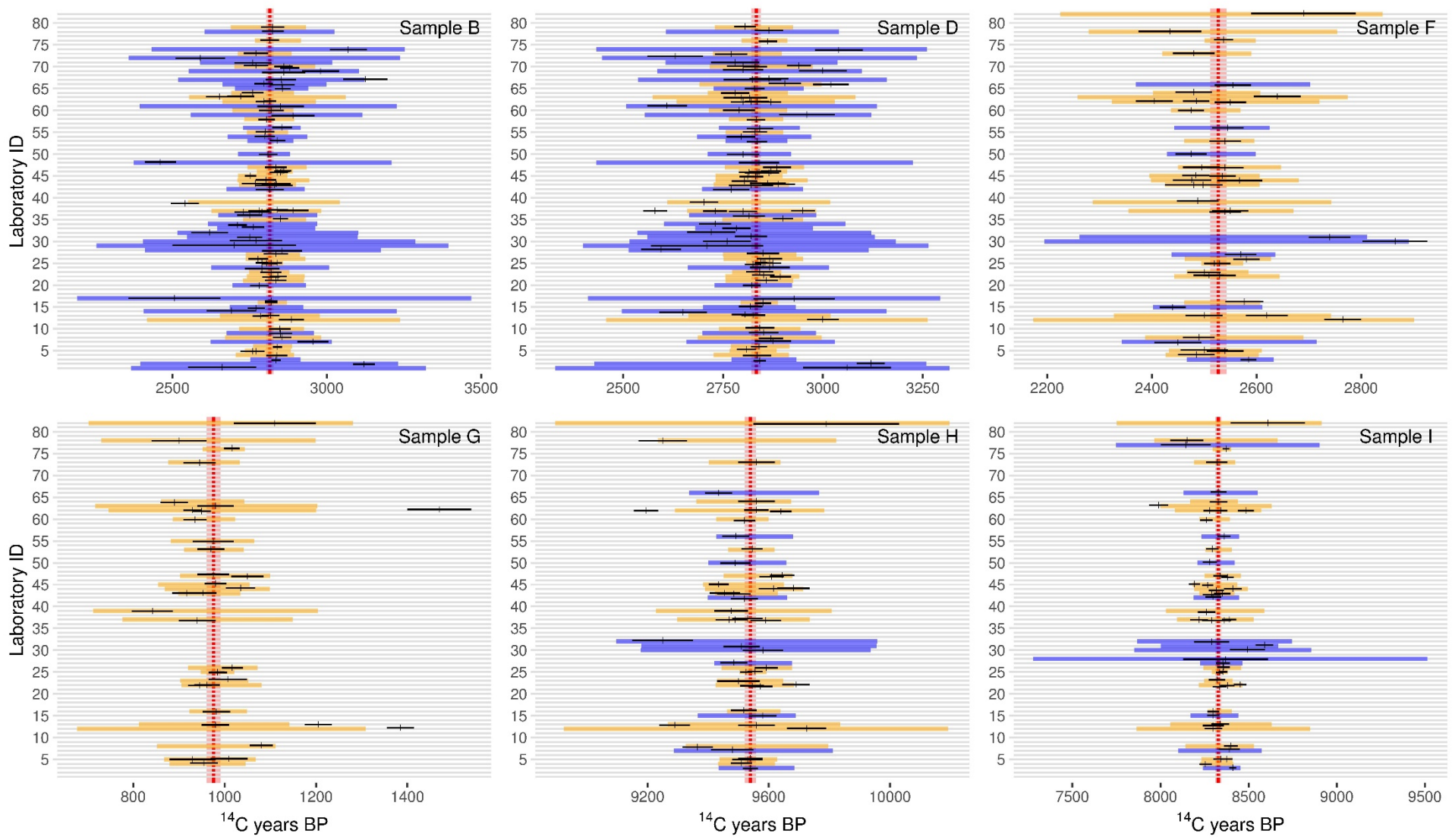


Figure S3.8. Posterior predictive check for the LBM. Each panel is a sample material reported in the VIRI study (Scott et al. 2007, 2010a, 2010b). Laboratory IDs are listed along the y-axes. Reported ^{14}C measurements and their associated errors (1σ) are indicated by vertical and horizontal black segments, respectively. Horizontal gold and purple bars show the 95% posterior prediction intervals for AMS and GPC/LSC laboratories, respectively. The dashed red lines and bands indicate the mean and 95% highest posterior density intervals for the ^{14}C value of each sample material.

4. Site and ^{14}C Sample Selection for the YDB and LST

Our simulations included only those ^{14}C measurements that are associated with samples from materials located within the YDB or LST stratigraphic layers. In this section, we list the sites with ^{14}C measurements taken on samples from these layers and describe those samples. Where applicable, we detail why certain sites or samples were excluded from the simulations.

4.1. YDB Sites and ^{14}C Samples

We compiled a preliminary list of ^{14}C measurements for the YDB based on those samples that Kennett et al. (23) present as originating from within a YDB layer. From there, we assessed each primary source to ensure the accuracy of each measurement and its provenience. The table below outlines the decisions made for each sample. Two samples that Kennett et al. (23) identified as originating from the YDB, yet were excluded in our simulations, are described in rows highlighted in orange. Twenty-one rows highlighted in blue describe samples that other publications describe as associated with a YDB layer while Kennett et al. (23) indicate otherwise. We did not include these samples in our simulations.

Lab Number	Reported ^{14}C		Material	References
	μ	σ		
Abu Hureyra, Syria				
UCIAMS-105429	11,070	40	Charcoal	(24, 25)
OxA-172	10,900	200	Charred Seed	(24, 26, 27)
OxA-430	11,020	150	Charred bone	(24, 26, 27)
OxA-468	11,090	150	Charred bone	(24, 26, 27)
BM-1718R	11,140	140	Charcoal	(24, 26, 27)
Discussion				
UCIAMS-105429 is the only sample that Kennett et al. (23) report as directly associated with the YDB layer at Abu Hureyra. However, Wittke et al. (24) indicate that this sample is <i>not</i> associated with the YDB layer. Sample OxA-172 (27) was originally interpreted by Wittke et al. (24) as being located within the YDB layer at Abu Hureyra. However, Kennett et al. (23:SI8) state that OxA-172 is “adjacent” to sample UCIAMS-105429, but not within the YDB layer. We default to Kennett et al. (23) regarding the provenience of these samples and have included sample UCIAMS-105429 but not sample OxA-172 in our simulations.				
Bunch et al. (26) identified samples OxA-430, OxA-468, and BM-1718R as close to the YDB layer via an age-depth model, although it is not clear that these samples were located within the YDB layer. Given their unsecure spatial relationship to the Abu Hureyra YDB layer, we deferred to Wittke et al. (24) and Kennett et al. (23) and excluded these samples from our simulations.				
Arlington Canyon, California, United States				
UCIAMS-47239	11,105	30	Charcoal	(28)
UCIAMS-36308	11,095	25	Wood	(28)
UCIAMS-42816	11,095	25	Wood	(28)
UCIAMS-36307	11,070	25	Wood	(28)
UCIAMS-36961	11,440	90	Carbon elongate	(28)
UCIAMS-36960	11,185	30	Carbon spherule	(28)
UCIAMS-36962	11,110	35	Wood	(28)
UCIAMS-36959	11,075	30	Glassy carbon	(28)
Beta-161032	10,860	70	Charcoal	(28)
UCIAMS-36306	11,375	25	Wood	(28)
UCIAMS-36305	11,235	25	Wood	(28)
UCIAMS-36304	11,105	30	Wood	(28)
Discussion				

Kennett et al. (23) indicate that all 12 of these samples are associated with the YDB at Arlington Canyon. We have included all 12 measurements in our simulations.

Barber Creek, North Carolina, United States

No sources report ¹⁴C measurements on samples recovered from the YDB layer.

Big Eddy, Missouri, United States

AA-27486	11,900	80	Charcoal	(29)
AA-26654	10,710	85	Charcoal	(24, 30)
AA-25778	10,260	85	Wood charcoal	(29)
AA-72612	10,959	54	Charcoal	(24, 31)

Discussion

Kennett et al. (23) designated two samples as associated with the YDB, AA-27486 and AA-26654. Wittke et al. (24) identified a peak in nanodiamonds between 327 and 335 cm below surface, leading Kennett et al. (2015) to differentiate samples within these depths from samples taken at other depths within the same stratum. In contrast, Hajic et al. (29) do not distinguish these two samples from an additional four samples within that stratum. Although located within the YDB layer, Kennett et al. (23) rejected AA-25778 as an outlier based on an OxCal age-sequence model and we have thus excluded it from our simulations.

Wittke et al. (24) identify AA-72612 as associated with the YDB, although Kennett et al. (23) indicate that this sample is from a context stratigraphically above the YDB. We excluded AA-72612 from our simulations.

Blackwater Draw, New Mexico, United States

SMU-1880	10,780	110	Soil humate	(24, 32)
----------	--------	-----	-------------	----------

Discussion

Wittke et al. (24) report that sample SMU-1880 is located within the YDB at Blackwater Draw (measurement originally reported by Johnson & Holliday (32)). However, Kennett et al. (23) do not include this sample in their narrative description, figures, or tables. Their supplemental OxCal code indicates that this sample was incorporated into an age-sequence model as a potential outlier. No other potential YDB samples are reported in the literature. Since Kennett et al. (23) do not explicitly identify SMU-1880 as associated with the YDB, we do not include this measurement in our simulations.

Blackville, South Carolina, United States

No sources report ¹⁴C measurements on samples recovered from the YDB layer.

Bull Creek, Oklahoma, United States

Beta-184854	11,070	60	Sediment organics	(33)
-------------	--------	----	-------------------	------

Discussion

Bement et al. (33) identified a Late Holocene peak in nanodiamonds not associated with the YDB.

Daisy Cave, California, United States

No sources report ¹⁴C measurements on samples recovered from the YDB layer.

Geldrop-Aalsterhut (Aalsterhut), Netherlands

GrA-49524	10,840	75	Charcoal	(34)
GrA-49509	10,865	55	Charcoal	(34)
GrA-49515	11,020	75	Charcoal	(34)
GrA-49570	10,735	45	Charcoal	(34)
GrA-49521	10,765	50	Charcoal	(34)
GrA-49516	10,765	50	Charcoal	(34)
GrA-49507	10,920	50	Charcoal	(34)
GrA-49527	10,960	60	Charcoal	(34)
GrA-49529	10,755	55	Charcoal	(34)
GrA-49573	10,860	45	Charcoal	(34)
GrA-49574	10,845	45	Charcoal	(34)
GrA-49569	10,895	45	Charcoal	(34)
GrA-49514	10,880	110	Charcoal	(34)
GrA-49575	10,900	50	Charcoal	(34)

Discussion

van Hoesel et al. (34) report 14 ^{14}C sample measurements from the charcoal-rich Usselo Horizon, which they identify as a stratigraphic marker with the potential to evaluate the Younger Dryas Impact hypothesis. Kennett et al. (23) exclude 11 of these sample measurements on the basis that they originate from the upper portion of the Usselo Horizon, which does not have nanodiamond markers. In their OxCal age-sequence model, Kennett et al. (23) placed these three YDB samples stratigraphically below the remaining 11 samples. In our simulations, we only included ^{14}C measurements from these three samples.

Indian Creek, Montana, United States

No sources report ^{14}C measurements on samples recovered from the YDB layer.

Lake Cuitzeo, Michoacán, Mexico

No sources report ^{14}C measurements on samples recovered from the YDB layer.

Lake Hind, Manitoba, Canada

UCIAMS-29317	10,610	25	Charcoal	(35)
--------------	--------	----	----------	------

Discussion

Kennett et al. (23) indicate that the single YDB ^{14}C sample is located below a peat layer, citing Firestone et al. (35). Firestone et al. (35), however, do not describe the sample used for the ^{14}C measurement. Firestone et al. (35) describe black mats, microspherules, glass-like carbon, and magnetic grains associated with the YDB, but they do not describe the context of the sample.

Lindenmeier, Colorado, United States

I-141	10,780	135	Charcoal	(36–38)
-------	--------	-----	----------	---------

Discussion

Kinzie et al. (37) state that there were no ^{14}C samples obtained from the nanodiamond rich layer that they define as the YDB. They indicate that sample I-141 is stratigraphically directly above the YDB (37). We follow Kennett et al. (23), who indicate that this sample dates the YDB layer, and have included it in our simulations.

I-141 was first published as $10,780 \pm 375$ ^{14}C BP (36) and later corrected to $10,780 \pm 135$ ^{14}C BP (38). Like Kennett et al. (23), we use the corrected error term.

Lingen, Lower Saxony, Germany

Beta-369246	10,870	40	Charcoal	(23)
-------------	--------	----	----------	------

Discussion

Wittke et al. (24) identify the YDB layer at 42–45cmbs by an abundance of charcoal combined with the presence of impact-related spherules. Kennett et al. (23) rely on this identification for their association of this sample with the YDB.

Lommel, Belgium

UCIAMS-46303	11,480	100	Charcoal	(24)
N/A	10,950	50	N/A	(24, 39)

Discussion

Kennett et al. (23) do not identify any ^{14}C samples from within the YDB, conflicting with a previous publication. Wittke et al. (24) report an AMS measurement on charcoal from the Lommel YDB layer (UCIAMS-46303). They also include an AMS measurement on charcoal of $10,950 \pm 50$ ^{14}C BP, although it lacks provenience information or a laboratory ID (24). Wittke et al. (24) cite van Geel et al. (39) as the source for this measurement. However, van Geel et al. (39) appear to have estimated the ^{14}C age of the onset of the Younger Dryas rather than report a ^{14}C measurement on a sample material. This likely explains why this value is not associated with a provenience or laboratory ID, it is not a ^{14}C measurement.

Kennett et al. (23) indicate that UCIAMS-46303 is stratigraphically below the YDB, and they do not include the latter ^{14}C estimate. No explanation is provided for these discrepancies with Wittke et al. (24). Due to the uncertain provenience of these ^{14}C samples, we followed Kennett et al. (23), and did not include any ^{14}C samples for the Lommel YDB in our simulations.

Melrose, Pennsylvania, United States

No sources report ^{14}C measurements on samples recovered from the YDB layer.

Mucuñuque, Venezuela

No sources report ^{14}C measurements on samples recovered from the YDB layer.

Murray Springs, Arizona, United States

A-1045	10,760	100	Charcoal + F ₂	(24, 40)
--------	--------	-----	---------------------------	----------

TX-1045	10,260	140	Humates + F ₂	(40)
TX-1044	12,600	2440	Charcoal + F ₂	(40)
TX-1462	10,930	170	Charcoal	(24, 40)

Discussion

Wittke et al. (24) indicate that charcoal sample TX-1462 dates the YDB, but this sample is missing entirely from the narrative, figures, and tables in Kennett et al. (23). An additional conflict is that TX-1462 is apparently included in their OxCal age-sequence model for Murray Springs (23), despite being absent elsewhere in the text. Further confusion arises from the fact that Wittke et al. (24) did not include TX-1045 or TX-1044 in their age estimations of the YDB. Of note are several Murray Springs ¹⁴C measurements that are incorrectly listed as OSL ages in Wittke et al. (24): Table S1 (AA-26212, A-1045, and TX-1462). We suspect that this is a typographic error that did not impact their analyses.

We deferred to Kennett et al.'s (23) list of YDB ¹⁴C samples for Murray Springs, thereby excluding TX-1462. Given the extreme ¹⁴C measurement error for TX-1044, we also excluded this sample in the simulations presented in our main paper. We did, however, include this sample in simulations of an alternative dataset presented in Section 5.

Ommen, Netherlands

UCIAMS-46307	11,440	35	Charcoal	(24)
--------------	--------	----	----------	------

Discussion

Kennett et al. (23) report that no ¹⁴C samples were recovered from the Ommen YDB. This conflicts with Wittke et al. (24), who report that AMS sample UCIAMS-46307 was recovered directly from charcoal in the YDB. Kennett et al. (23) report that this sample originates from a context stratigraphically *below* the YDB. For our simulations, we deferred to Kennett et al. (23) and did not include any samples from Ommen.

Santa Maira, Spain

Beta-75225	11,020	140	Charcoal	(41)
------------	--------	-----	----------	------

Discussion

We followed Kennett et al. (23) and included this single sample for the Santa Maira YDB.

Sheriden Cave, Ohio, United States

UCI-38249-(C)	10,915	30	Bone Clovis point	(42)
Beta-127909	10,840	80	Wood charcoal	(43)
Beta-127910	10,960	60	Wood charcoal	(43)

Discussion

Kennett et al. (23) indicate that all 3 of these samples are associated with the YDB at Sheriden Cave, which is visible as a discontinuous ash layer. We have included all 3 measurements in our simulations.

Talega, California, United States

Beta-196150	11,070	50	Charcoal	(44) in (23, 24)
-------------	--------	----	----------	------------------

Discussion

We followed Kennett et al. (23) and included this single sample for the Talega YDB.

Topper, South Carolina, United States

AA-100294	10,958	65	Charcoal	(45)
-----------	--------	----	----------	------

Goodyear (45) provided one ¹⁴C sample from charcoal associated with the Clovis layer at Topper. Wittke et al. (24) define the YDB as immediately above the Clovis layer from which this date derived. We deferred to Kennett et al. (23) and included this ¹⁴C sample in our simulations.

4.2. LST Sites and ¹⁴C Samples

Many of the samples described here were originally summarized in Baales et al. (2). Three rows highlighted in orange describe ¹⁴C samples recovered from within the LST and summarized by Baales et al. (2) yet excluded in our simulations for reasons specified in the associated discussion paragraphs. Ten rows highlighted in blue describe ¹⁴C samples recovered from stratigraphic contexts near the LST, but not from within it. Since these samples likely do not date the Laacher See volcanic eruption, we excluded them from our simulations.

Laboratory Number	Reported ^{14}C		Material	Original Reference
	μ	σ		
Brohl Valley				
HV-11774	11,075	185	Plant remains	(46)
HD-17900	11,277	26	Tree 1/4, rings 1–38	(47)
KN-3800	11,240	100	<i>Populus</i>	(48)
KN-3801	11,260	95	<i>Populus</i>	(48)
KN-3802	11,280	100	<i>Populus</i>	(48)
KN-3803	11,510	90	<i>Populus</i>	(48)
Unknown	11,085	90	Charcoal	(49, 50)
HD-17100	11,206	20	1a ca. 50 rings	(47)
HD-17145	11,223	22	3a ca. 50 rings	(47)
HD-17101	11,121	28	5b ca. 50 rings	(47)
Discussion				
Neither Frechen (49) nor Schweitzer (50) report the laboratory number for the unknown sample.				
Glees				
GrA-?	10,680	85	Charcoal	(51)
Discussion				
Frechen (51) provides the laboratory but not the sample number.				
Kruft				
HD-19098	11,063	30	<i>Populus</i> 9 rings 1-20	(47, 52)
HD-18438	11,065	22	<i>Populus</i> 8 outer rings	(47, 52)
HD-19092	11,066	28	<i>Populus</i> 9 rings 21-30	(47, 52)
HD-18622	11,073	33	<i>Populus</i> 9 rings 31-40	(47, 52)
HD-19037	11,075	28	<i>Populus</i> 9 rings 41-50	(47, 52)
HD-18648	11,037	27	<i>Populus</i> 1 rings 31-40	(47, 52)
Discussion				
Four of these measurements (HD-19098, HD-19092, HD-18622, and HD-19037) originate from the same tree (<i>Populus</i> 9). For this reason, we only included the sample corresponding to rings 1-20 (HD-19098) in our simulation. This sample logically corresponds to the only <i>Populus</i> 9 measurement that could plausibly date the calendar year of the Laacher See eruption. The other three samples must precede the eruption it in the order indicated by their ring sequences.				
Miesenhein IV				
OxA-3584	11,190	90	<i>Alces alces</i> bone	(53)
OxA-3585	11,310	95	<i>Alces alces</i> bone	(53)
OxA-3586	11,190	100	<i>Alces alces</i> bone	(53)
Discussion				
Hedges et al. (53) note that the <i>Alces</i> remains predate the Laacher See eruption as there was time for moss accumulation prior to deposition of the LST. While not enough time elapsed to fully surround the remains in the pre-LST layer, the event must necessarily have followed the death of the animal, and we have therefore excluded these measurements.				
Nette Valley				
W-525	10,800	300	Charcoal	(51)
N/A	10,880	95	Charcoal	(54)
Discussion				
In their supplementary data, van den Bogaard & Schmincke (54) note that the second ^{14}C measurement is from a personal communication with Geyh in 1976.				
Soppensee				
ETH-5290	10,760	80	Macrofossils	(55, 56)
ETH-6930	11,190	80	Macrofossils	(55, 56)
ETH-6932	10,540	150	Macrofossils	(55, 56)
ETH-12617	11,040	90	Macrofossils and wood/bark	(56)
ETH-12615	11,370	90	Macrofossils and wood/bark	(56)
ETH-12613	11,220	90	Macrofossils and wood/bark	(56)

ETH-12610	11,180	100	Macrofossils and wood/bark	(56)
Discussion				
Hajdas et al. (56) report the bottom four ^{14}C measurements on samples from 1-2 cm sediment slices that also contain ash from the Laacher See eruption. However, the relationship between the sample materials and the ash within each slice is unknown. ETH-5290 and ETH-6930 are from materials "stratigraphically close" to Laacher See ash (55), although it is unclear how close the ash is to each sample or if the samples originate from within ash. Hajdas et al. (56) subsequently estimated that ETH-5290 postdates the LST by 20 ^{14}C years and ETH-6930 predates the LST by 60 ^{14}C years. ETH-6932 was originally reported by Hajdas et al. (55), but they did not describe this sample as associated with Laacher See ash. Hajdas et al. (56) later estimated that this sample predates the LST by 140 ^{14}C years.				
Although these measurements all appear to originate from sample organisms that died chronologically near the Laacher See eruption, the exact chronological relationships between each sample and deposition of the LST are unclear. In some cases, samples appear to postdate the LST, which is an issue that our simulations do not account for. As such, we excluded these measurements from our simulations.				
Thelenberg				
HD-?	10,950	190	Charcoal	(51)
Discussion				
Frechen (51) provides the laboratory but not the sample number.				
Tönnisstein				
W-528	11,150	200	Charcoal	(57)
GrA-?	11,025	90	Charcoal	(51)
Discussion				
Frechen (51) provides the laboratory but not the sample number for the latter sample.				

5. Simulations of Alternative Dataset_O

The simulated distributions of dataset_E presented in the main paper are contingent on features of their associated dataset_O, including the quoted ^{14}C measurement errors, the number of “old wood” dates, the number of participating laboratories, and the types of laboratories (i.e., AMS or GPC/LSC). The inclusion or exclusion of samples could also affect the inferred congruity between MPMD_O and $^{14}\text{C}_O$ values and MPMD_E and $^{14}\text{C}_E$ distributions. In other words, alternative dataset_O could produce simulated MPMD_E and $^{14}\text{C}_E$ distributions that suggest that MPMD_O and $^{14}\text{C}_O$ are either more consistent or less consistent with a synchronous event. This presents a potential problem, as variability in reasonable researcher decisions must correspond to variability in results. This section presents a limited “multiverse analysis” (*sensu* (58)), in which we detail the results of alternative simulations to illustrate the degree to which the findings in our main paper vary with data inclusion decisions. Our multiverse analysis is “limited” because we cannot anticipate every possible argument that might be made for including or excluding certain measurements, and we therefore only analyzed those dataset_O that we felt most likely to arise from other researchers’ decisions.

5.1. Potential Data Inclusion Decisions and Their Corresponding Dataset_O

The main paper already addresses some potential researcher decision-driven variability in the form of the six different simulations (A-C1 and A-C2). These simulations address how results vary when “old wood” offsets are ignored (simulations A1-2), when “old wood” effects are assumed to be small (simulations B1-2), when “old wood” effects are assumed to be generally large (simulations C1-2), when variability in laboratory measurement is ignored (simulations A-C1), and when variability in laboratory measurement is included (simulations A-C2). However, these amount to different decisions regarding simulation parameters rather than data inclusion. These six simulations, representing variability in simulation parameter decisions, will be repeated for each of three alternative alternative datasets detailed below. We refer to these as Alternative Datasets_O 1, 2, and 3.

Alternative Dataset_O 1 includes the five ^{14}C measurements that were excluded from the main dataset_O, as discussed in the main paper: TX-1044 ($12,600 \pm 2440$ ^{14}C BP) from Murray Springs and AA-25778 ($10,260 \pm 85$ ^{14}C BP) from Big Eddy, as well as Kruft samples HD-19092 ($11,066 \pm 28$ ^{14}C BP), HD-18622 ($11,073 \pm 33$ ^{14}C BP), and HD-19037 ($11,075 \pm 28$ ^{14}C BP). The former two samples correspond to the YDB dataset. TX-1044 is a non-AMS measurement on charcoal, and we have scored this measurement as a potential “old wood” sample. It was excluded in the main dataset_O due to its anomalously large error, which is at least an order of magnitude larger than any other error in the YDB dataset_O, and importantly, much larger than the errors reported in the VIRI dataset to which the LBM was fitted. As such, it is unknown whether the LBM provides realistic parameter values for how much intra- and inter-laboratory measurement variability should be expected with an error this large. We excluded AA-25778 from the main dataset_O since this measurement came from a wood charcoal specimen with potential redeposition issues, so its spatial association with the YDB layer is not secure (24). We have scored this as another potential “old wood” sample. The three Kruft dates all correspond to LST measurements from a series of adjacent tree rings from the same wood specimen, designated as *Populus* 9 (2, 52). We included the most recent *Populus* 9 date in the main dataset_O (HD-19098 $11,063 \pm 30$ ^{14}C BP), as it comes from the outermost rings and is logically the closest of these dates to the actual calendar date of the LST. The three excluded *Populus* 9 measurements must logically date to earlier than HD-19098 and have a known chronological order that predates the LST, the sequence of which is not captured in the simulation. For Alternative Dataset_O 1, we have included these measurements and scored all three as potential “old wood” dates.

Alternative Dataset_O 1 is the most inclusive set of measurements that we could construct for the LST and YDB. As detailed above, these five additional measurements have potential problems that lead us to exclude them from the simulations detailed in the main paper. However, since it could be argued that any one or all these measurements may be validly associated with the events of interest, we consider this possibility. Notably, $MPMD_O$ and $^{14}C\%$ suggest an LST Alternative Dataset_O 1 that is more tightly clustered than the LST dataset_O in the main paper (Table S5.1). In contrast, for the YDB, the values for Alternative Dataset_O 1 suggest a more dispersed set of measurements than those in the main paper dataset_O.

Alternative Dataset_O 2 excludes three YDB ^{14}C measurements that were included in the main text dataset: Beta-184854 ($11,070 \pm 60$ ^{14}C BP) from Bull Creek, TX-1045 ($10,260 \pm 140$ ^{14}C BP) from Murray Springs, and AA-27864 ($11,900 \pm 80$ ^{14}C BP) from Big Eddy. These values were excluded due to the possibility that dispersion in YDB dataset_O may be driven by unreliable measurements. As such, removing these measurements could lead to a dataset_O that is more consistent with simulated dataset_E distributions for a synchronous depositional event, contrary to the findings we present in the main text. In effect, Alternative Dataset_O 2 is an attempt to bias dataset_O in a manner favorable to the synchronicity requirement of the hypothesized Younger Dryas Impact, based on reasonable arguments that a researcher might make about excluding observations in dataset_O.

Beta-184854 and TX-1045 are from soil organic matter (SOM), which represent values for the time-averaged death and deposition dates of many small organisms within each sample's respective stratum. Dates corresponding to SOM measurements do not represent a single event, and they generally postdate the depositional event of interest due to continued input of organic matter into a geological layer after sedimentary deposition (Wang et al. 1996). This potential issue is supported by the observation that TX-1045 is 350 ^{14}C years younger than the next youngest measurement in YDB dataset_O, UCIAMS-29317 ($10,610 \pm 25$ ^{14}C BP). Unlike TX-1045, Beta-184854 is not anomalously young, but we have excluded it since the measurement is associated with similar SOM material. AA-27864 is not a SOM measurement, but rather a measurement on charcoal. We have excluded it because it is anomalously old, at 460 ^{14}C years older than the next oldest measurement in YDB dataset_O, UCIAMS-36961. Although we do not feel that it is justified to remove AA-27486 based on its age alone—hence, why we included it in our main dataset_O—we anticipate that other researchers might exclude it. In combination, our removal of these three measurements produces YDB $MPMD_O$ and $^{14}C\%$ values that appear more consistent with synchronicity than those values for the main text dataset_O (Table S5.1).

Alternative Dataset_O 3 eliminates the Arlington Canyon measurements ($n = 12$) from YDB dataset_O and the Brohl Valley measurements ($n = 10$) from LST dataset_O. Samples from these two sites represent 40.0% and 52.6% of each respective dataset_O, contributing a disproportionately large share of measurements. As such, any site-level factors that affect the dispersion of ^{14}C measurements within each site could have an outsized effect on either YDB or LST dataset_O. When measurements from these two sites are removed, $MPMD_O$ and $^{14}C\%$ appear more clustered and consistent with synchronicity for the LST (Table S5.1). For the YDB, $MPMD_O$ appears more consistent with synchronicity, but $^{14}C\%$ becomes more dispersed and looks less consistent with synchronicity.

Table S5.1. Summary statistics for the three alternative dataset_o alongside the dataset presented in the main paper.

Dataset	<i>n</i> ¹⁴ C measurements (average lab error)		MPMD _o		¹⁴ C δ	
	LST	YDB	LST	YDB	LST	YDB
Main Dataset	19 (94.5)	30 (59.0)	0.71	0.75	196.94	282.02
Alternative Dataset 1	22 (85.6)	32 (134.2)	0.68	0.78	182.56	416.64
Alternative Dataset 2	19 (94.5)	27 (55.2)	0.71	0.72	196.94	190.65
Alternative Dataset 3	9 (115.4)	18 (74.2)	0.60	0.70	156.94	315.32

5.2. Another Simulation Parameter Consideration for the LBM

The simulations presented in the main text use parameters from the LBM to generate variability that would be expected given minor systematic biases in measurement between laboratories, as well as variability in the repeatability of measurements between laboratories. Additionally, simulations are presented without the LBM for a hypothetical situation where all laboratories provide perfect measurements of target ¹⁴C values. Here, we address an aspect of the LBM that concerns a major difference between YDB and LST dataset_o: the method of measurement, which we consider at the level of AMS vs GPC/LSC measurements. For YDB dataset_o, only three of the 30 measurements are GPC or LSC (10%). In contrast, all 19 LST measurements are GPC or LSC.

The LBM posterior parameter values suggest that GPC/LSC laboratories generally have larger systematic biases and poor repeatability than AMS laboratories (see Section 3). Consequently, dataset_o that are dominated by GPC/LSC values lead to simulated distributions of dataset_E with higher dispersion on-average. This played a strong role in the simulated outcomes for the LST; The LST results presented in the main paper are consistent with synchronicity in part because distributions of dataset_E were relatively dispersed due to the high number of observed GPC/LSC measurements. In contrast, the AMS-dominated YDB dataset_o is associated with relatively clustered sets of expected values. In short, the GPC/LSC distinction that we built into the LBM played a strong role in the differences in simulated expectations between the YDB and LST.

To explore the consequences of this LBM modelling decision, we ran additional simulations with every measurement in each dataset_o scored as an AMS measurement. This was done for main text dataset_o and for the three alternative dataset_o presented above. The goal of these “all measurements as AMS” simulations was to explore to what degree our decision to model this aspect of measurement method influences the dispersion dataset_E, while at the same time retaining other aspects of the LBM. It should be noted that the LBM used for these simulations does not in principle ignore AMS vs GPC/LSC distinctions, as we use the same fitted LBM model with the same parameters. Rather, we simply treat all measurements in each dataset_o as AMS measurements.

5.3. Results of Alternative Dataset_o Simulations

In total, this “multiverse analysis” entailed 42 separate simulations over six different parameterizations (A1-C1 and A2-C2) and across seven different dataset_o (the main text dataset_o scored as all AMS measurements, as well as the three alternative dataset_o, each run both with the reported AMS/GPC/LSC distinctions and with all measurements scored as AMS). When describing the results for each alternative dataset_o, we focus on simulation C2, much like the

results described in the main paper. We focus on simulation C2 because it contains the most sources of variability, which likely most closely approximates the large number of sources that must affect real ^{14}C datasets (i.e., C2 is characterized the most realism of the six simulations). The remaining five simulations show expectations when these sources of variability are excluded (or their effects are relaxed, as is the case for the OWM simulations with λ set to 0.04).

5.3.1. Alternative Dataseto 1

Alternative Dataseto 1 includes five measurements that were excluded from the main paper dataseto, three for the LST and two for the YDB. Including these five measurements produces an LST dataseto that is more consistent with synchronicity and a YDB dataseto that is less consistent with synchronicity. For the LST simulations that included the LBM, the percentage of iterations that produced $MPMD_E$ that exceed $MPMD_o$ range from 5.97% to 15.48% (simulations A2 and C2, respectively; Figure S5.1). In these same simulations, the percentage of iterations that produced $^{14}\text{C}_E^g$ exceeding $^{14}\text{C}_O^g$ varies between 5.95% and 14.15% (simulations A2 and C2, respectively; Figure S5.2). In contrast, for YDB simulations that included the LBM, these proportions vary between 0.02- 0.03% for $MPMD_E$ (simulations A2 and C2, respectively) and remain below 0.01% for $\sigma_{\mu^{14}\text{C}}$.

Between the two events, the effect on $MPMD_E$ of including the ^{14}C measurements that we excluded in the main paper had its largest effect on the LST simulations. In simulation C2, the number of iterations that produced $MPMD_E$ exceeding $MPMD_o$ increased by 134.59%. Across individual calendar years in simulation C2, the number of LST $MPMD_E$ exceeding $MPMD_o$ varies between 971-2608 of 10,000 (9.71-26.08%) iterations. In contrast, the YDB simulations produced fewer $MPMD_E$ exceeding $MPMD_o$ when the two ^{14}C measurements that were withheld from the main dataseto are included. In simulation C2, the number of iterations with $MPMD_E$ greater $MPMD_o$ decreased by 30.81% for the YDB. The number of C2 iterations that produced $MPMD_E$ exceeding $MPMD_o$ varies across calendar years: 1-6 of 10,000 (0.01-0.06%) iterations.

For the LST, the number of $^{14}\text{C}_E^g$ exceeding $^{14}\text{C}_O^g$ increased when the three additional ^{14}C measurements are included. In LST simulation C2, the number of $^{14}\text{C}_O^g$ meeting this criterion increased by 32.55%. Across individual calendar years in LST simulation C2, the number of iterations that produced $^{14}\text{C}_E^g$ exceeding $^{14}\text{C}_O^g$ ranges from 1097-1759 of 10,000 (10.97-17.59%) iterations. In contrast, for YDB simulation C2, the number of simulated $^{14}\text{C}_E^g$ exceeding $^{14}\text{C}_O^g$ decreased by 75.35% when the two additional ^{14}C measurements are included. Across individual calendar years for YDB simulation C2, the number of $^{14}\text{C}_E^g$ exceeding $^{14}\text{C}_O^g$ varies between 0-3 of 10,000 (0.00-0.03%) iterations. Sixty-nine of 101 calendar years did not contain a single iteration that yielded an $^{14}\text{C}_E^g$ greater than $^{14}\text{C}_O^g$.

The LST dataseto is more consistent with synchronicity when the three additional ^{14}C measurements are included (Figure S5.3). In simulation C2, the $MPMD_o$ and $^{14}\text{C}_O^g$ sit within 1.65 z-scores from mean $MPMD_E$ and $^{14}\text{C}_E^g$. For the other LST simulations with the LBM, A2 and B2, simulated values fall within 1.65-2 z-scores above the simulated mean values. In contrast, YDB $MPMD_o$ and $^{14}\text{C}_O^g$ are never less than 4.5 z-scores from the simulated mean $MPMD_E$ and $^{14}\text{C}_E^g$ (based on simulated expectations, the probability of observing values 4.5 z-scores above the mean is about 3.4E-6). In sum, the effect of including the two additional ^{14}C measurements in YDB dataseto makes YDB dataseto moderately less consistent with synchronicity. In contrast, including the three additional LST ^{14}C measurements in LST dataseto produces an LST dataseto that is more consistent with synchronous deposition.

Scoring all Alternative Dataseto 1 ^{14}C measurements as AMS reduces the degree to which each event is consistent with synchronicity. This is especially true for the LST simulations. For

those LST simulations that included the LBM, the percentage of iterations that produced $MPMD_E$ exceeding $MPMD_0$ ranges from 1.34% to 5.54% (simulations A2 and C2, respectively; Figure S5.4). The percentage of iterations that produced ^{14}CE exceeding $^{14}C_0$ ranges from 1.37% to 6.25% for LST simulations that include the LBM (simulations A2 and C2, respectively). For YDB simulations that included the LBM, these percentages sit at about 0.02% for $MPMD_E$ and less than 0.01% for ^{14}CE (Figures S5.4 and S5.5).

Scoring all ^{14}C measurements as AMS has a larger effect on simulated $MPMD_E$ than ^{14}CE (Figure S5.4). For LST simulation C2, the number of iterations that produced $MPMD_E$ exceeding $MPMD_0$ decreased by 64.23% when all ^{14}C measurements were scored as AMS. Across individual calendar years for simulation C2, the number of iterations that produced these larger values varied between 239-1307 of 10,000 (2.39-13.07%) simulated values. For YDB simulation C2, the number of iterations with $MPMD_E$ exceeding $MPMD_0$ decreased by 21.26% after all ^{14}C measurements were scored as AMS. The number of iterations that produced these larger values varies across individual calendar years for YDB simulation C2: 0-5 of 10,000 (0.00-0.05%) iterations after all ^{14}C measurements were scored as AMS.

Simulated ^{14}CE were marginally smaller after all ^{14}C measurements were treated as AMS measurements (Figure S5.5). In LST simulation C2, the number of iterations associated with ^{14}CE exceeding $^{14}C_0$ decreased by 55.86%. Within LST simulation C2, there was variation across individual calendar years in the number of simulated ^{14}CE exceeding $^{14}C_0$: 410-850 of 10,000 (4.10-8.50%) iterations when all ^{14}C measurements are treated as AMS measurements. For the YDB, the number of iterations that produced ^{14}CE exceeding $^{14}C_0$ decreased by 60.00% for simulation C2 after all ^{14}C measurements were scored as AMS. In 87 of the 101 individual calendar years, with 10,000 iterations each, YDB simulation C2 did not produce a single ^{14}CE exceeding $^{14}C_0$ with all ^{14}C measurements scored as AMS. The remaining 14 iterations only produced one ^{14}CE exceeding $^{14}C_0$.

The effect of scoring all ^{14}C measurements as AMS makes LST dataset₀ generally less probable across simulations, given a true synchronous event (Figure S5.6). This is especially true for simulations A2 and B2, where LST $MPMD_0$ and $^{14}C_0$ sit right at or just beyond three z-scores from mean simulated $MPMD_E$ and ^{14}CE . When these ^{14}C measurements are correctly scored as GPC/LSC measurements, $MPMD_0$ and $^{14}C_0$ remain within two z-scores of simulated mean $MPMD_E$ and ^{14}CE (Figure S5.3). For simulation C2, $^{14}C_0$ remains within 1.65 z-scores from simulated mean ^{14}CE for the LST. There is more variability for $MPMD_E$ in simulation C2, where $MPMD_0$ varies between about 1-2.5 z-scores from simulated mean $MPMD_E$. While YDB dataset₀ becomes less probable when all ^{14}C measurements are scored as AMS, the difference from when they are correctly classified as either AMS or GPC/LSC is marginal. In all simulations, $MPMD_0$ and $^{14}C_0$ remain at least 4.5 z-scores above mean simulated $MPMD_E$ and ^{14}CE .

5.3.2. Alternative Dataset₂

Alternative Dataset₂ includes all the LST ^{14}C measurements but excludes three ^{14}C measurements from YDB dataset₀. Two ^{14}C measurements were excluded since they are associated with SOM samples (Beta-184854 and TX-1045), and the third ^{14}C measurement was excluded because it is anonymously old (AA-27486). Excluding these three ^{14}C measurements produces a YDB dataset₀ with tighter clustering (Table S5.1). As such, the LST simulations resemble those in the main text, with minor deviations due to simulation variance. The YDB simulations, however, yielded results that differ from those in the main text.

Alternative Dataset_O 2 still did not produce YDB $MPMD_E$ exceeding $MPMD_O$ when the LBM is excluded (with the exception of a single simulated $MPMD_E$ in C1; Figure S5.7:A1-C1). For simulations that included the LBM, the number of $MPMD_E$ exceeding $MPMD_O$ increased by 70% (simulation B2) to 109% (simulation C2) relative to the simulated results for the main text dataset_O. However, $MPMD_E$ still rarely exceeds $MPMD_O$, which remain almost two orders of magnitude less probable than $MPMD_O$ in the LST simulations (Figure S5.9). Across these simulations, C2 produced the most YDB $MPMD_E$ exceeding $MPMD_O$. However, this still entails very few values. For individual calendar years, 4-17 of 10,000 (0.04-0.17%) $MPMD_E$ exceed $MPMD_O$ in Alternative Dataset_O 2. The high value of 17 only occurred for one calendar year, 12,736 cal BP. In contrast, across individual calendar years, LST simulation C2 produced 516-921 of 10,000 (5.16-9.21%) $MPMD_E$ exceeding $MPMD_O$ for Alternative Dataset_O 2.

Relative to $MPMD_E$, $^{14}C_E$ for Alternative Dataset_O 2 exceed $^{14}C_O$ more often than in the simulations for the main text dataset_O (Figure S5.8). For simulations that included the LBM, the number of $^{14}C_E$ exceeding $^{14}C_O$ increased by 664% (simulation A2) to 3456% (simulation C2) relative to the simulated results for the main text dataset_O. However, even with this dramatic increase in $^{14}C_E$ exceeding $^{14}C_O$, this is still a relatively small proportion of $^{14}C_E$. Simulation C2 produced the most $^{14}C_E$ exceeding $^{14}C_O$. For individual calendar years, 29-66 of 10,000 (0.29-0.66%) $^{14}C_E$ exceeded $^{14}C_O$ for YDB Alternative Dataset_O 2. The high value of 66 occurred for only a single calendar year, 12,832 cal BP. In contrast, LST simulation C2 produced comparatively more $^{14}C_E$ exceeding $^{14}C_O$ for Alternative Dataset_O 2. The number of iterations with $^{14}C_E$ exceeding $^{14}C_O$ span 850-1310 of 10,000 (8.5-13.10%) across calendar years.

Even with the three potentially problematic YDB measurements removed, simulated $MPMD_E$ and $^{14}C_E$ still suggest that YDB Alternative Dataset_O 2 is much less probable LST Alternative Dataset_O 2, given a synchronous event in both scenarios (Figure S5.9). LST $MPMD_O$ and $^{14}C_O$ generally fall within two standard deviations of mean simulated $MPMD_E$ and $^{14}C_E$ for simulation C2. In contrast, YDB Alternative Dataset_O 2 YDB $MPMD_O$ always sits at least three standard deviations above mean $MPMD_E$, and YDB $^{14}C_O$ always sits at least two standard deviations above mean simulated $^{14}C_E$.

The results of the Alternative Dataset_O 2 simulations shift when all measurements are treated as AMS, making LST $MPMD_O$ and $^{14}C_O$ less probable in the context of the simulations. Across calendar years, LST $MPMD_E$ exceed $MPMD_O$ in 122-279 of 10,000 (1.22-2.79%) simulated values for C2. For comparison, for simulation C2, YDB $MPMD_E$ exceed $MPMD_O$ in only 3-14 of 10,000 (0.03-0.14%) iterations (Figure S5.10). The LST $^{14}C_E$ exceed $^{14}C_O$ in 304-580 of 10,000 (3.04-5.80%) iterations across calendar years for simulation C2. For YDB simulation C2, $^{14}C_E$ exceed $^{14}C_O$ in just 27-70 of 10,000 (0.27-0.70%) iterations (Figure S5.11).

Scoring all Alternative Dataset_O 2 measurements as AMS results in simulated LST values that suggest that the LST $MPMD_O$ and $^{14}C_O$ are less probable than when they are scored as GPC/LSC (Figure S5.12). This is especially true when the LBM is excluded (simulations A1-C1) or when the LBM is included but “old wood” effects are minimal or left unconsidered (simulations A2-B2). In these cases, $MPMD_O$ and $^{14}C_O$ for the LST never fall below three standard deviations from mean simulated $MPMD_E$ and $^{14}C_E$ (i.e., the probability of observing those values, given a synchronous event, remains below about 0.001). For simulation C2, LST $MPMD_O$ and $^{14}C_O$ fall between two and three standard deviations above simulated mean $MPMD_E$ and $^{14}C_E$, depending on the calendar year. Scoring all Alternative Dataset_O 2 measurements as AMS has very little effect on the simulated results for the YDB (Figure S5.12).

In sum, the Alternative Dataset_O 2 simulations suggest that excluding the three potentially problematic YDB measurements has a minimal effect on the simulated inferences regarding the differences between YDB dataset_O and LST dataset_O. LST dataset_O remains at least an order of magnitude more probable, given a synchronous event, than does YDB dataset_O. This difference is mostly retained when measurements are all scored as AMS, although LST dataset_O becomes less consistent with synchronicity. For simulation C2, when all measurements are scored as AMS, the probability of LST dataset_O begins to approach that of YDB dataset_O, although it remains a more probable set of observations given a synchronous event.

5.3.3. Alternative Dataset_O 3

Alternative Dataset_O 3 includes all ^{14}C measurements from the dataset used in the main text, with the exclusion of measurements from Arlington Canyon and Brohl Valley. Measurements from these sites were excluded as they comprise a disproportionately large share of the measurements in the YDB and LST datasets. LST $MPMD_O$ becomes dramatically more consistent with synchronicity when Brohl Valley is excluded, and there is little change in the level of agreement between YBD $MPMD_O$ and $MPMD_E$ when Arlington Canyon is removed (Figure S5.13). For simulation C2 of LST Alternative Dataset_O 3, the number of iterations with $MPMD_E$ exceeding $MPMD_O$ is 561.10% higher than it is for the LST main text dataset. Across individual calendar years with 10,000 iterations each, 2710-6471 (27.10-64.71%) iterations produced $MPMD_E$ exceeding $MPMD_O$ in simulation C2. In contrast, for YDB Alternative Dataset_O 3 simulation C2, the number of iterations with $MPMD_E$ exceeding $MPMD_O$ increased by 46.67%. Across individual calendar years in simulation C2, only 2-14 of 10,000 (0.02-0.14%) iterations produced $MPMD_E$ exceeding $MPMD_O$ for YDB Alternative Dataset_O 3.

Much like $MPMD_E$, $^{14}\text{C}_E$ also tended to exceed the $^{14}\text{C}_O$ more often when the Brohl Valley and Arlington Canyon ^{14}C measurements are excluded (Figure S5.14). However, the effect of excluding these measurements is not as pronounced on $^{14}\text{C}_E$ as it is on $MPMD_E$. In LST simulation C2, the number of iterations that produced $^{14}\text{C}_E$ exceeding $^{14}\text{C}_O$ increased by 165.21% when the Brohl Valley samples are excluded. This varies across individual calendar years in LST simulation C2, with 2188-3424 of 10,000 (21.88-34.24%) iterations producing $^{14}\text{C}_E$ exceeding $^{14}\text{C}_O$. For YDB simulation C2, the number of $^{14}\text{C}_E$ exceeding $^{14}\text{C}_O$ increased by only 3.52% when the Arlington Canyon measurements are excluded. This increase amounts to only five iterations, and the difference may be attributable to simulation variance as much as it is to the effect of excluding the Arlington Canyon measurements. For YDB simulation C2, the number of iterations that produced $^{14}\text{C}_E$ exceeding $^{14}\text{C}_O$ varies across calendar years: 0-5 of 10,000 (0.00-0.05%) iterations produced these greater $^{14}\text{C}_E$ values.

For Alternative Dataset_O 3, the observed LST measurements are relatively probable not only for simulation C2, but also simulations A2 and B2 (Figure S5.15). In simulation C2, $MPMD_O$ and $^{14}\text{C}_O$ never fall more than one standard score above mean simulated $MPMD_E$ and $^{14}\text{C}_E$. In contrast $MPMD_O$ and $^{14}\text{C}_O$ for the YDB remain at least three z-scores mean simulated $MPMD_E$ and $^{14}\text{C}_E$ (Figure S5.15).

Scoring all Alternative Dataset_O 3 measurements as AMS produces produces simulated results that are less consistent with synchronicity than when measurements are correctly scored as GPC/LSC (Figure S5.16). This is most pronounced LST Alternative Dataset_O 3. In this case, across individual calendar years for simulation C2, 1520-5560 of 10,000 (15.20-55.60%) iterations produced $MPMD_E$ exceeding $MPMD_O$. In comparison, 2710-6471 of 10,000 (27.10-64.71%) iterations are greater than $MPMD_O$ when all measurements are scored as GPC/LSC. For YDB simulation C2, across individual calendar years, 0-9 of 10,000 (0.00-9.00%) iterations produced $MPMD_E$ exceeding $MPMD_O$ when all measurements are scored as AMS. For

comparison, when the YDB measurements are correctly scored as either AMS or GPC/LSC, calendar year variability sits at 2-14 of 10,000 (0.02-0.14%) of iterations. As such, for YDB dataset_O, scoring all values as AMS has a relatively minor effect on the degree to which dataset_O is consistent with synchronicity.

Simulated $^{14}\text{C}_E$ change in a manner similar to simulated $MPMD_E$ when Alternative Dataset_O 3 measurements are all scored as AMS (Figure S5.17). For LST simulation C2, 1360-2419 of 10,000 (13.60-24.19%) iterations produced $^{14}\text{C}_E$ exceeding $^{14}\text{C}_O$ across calendar years when all measurements are scored as AMS. For comparison, this calendar year variation changes to 2188-3424 of 10,000 (21.88-34.24%) iterations when all Alternative Dataset_O 3 measurements are correctly scored as GPC/LSC. For YDB simulation C2, 0-4 of 10,000 (0.00-0.04%) iterations produced $^{14}\text{C}_E$ exceeding $^{14}\text{C}_O$ across calendar years when all measurements are scored as AMS. When all measurements are correctly scored as either AMS or GPC/LSC, this changes to 0-5 of 10,000 (0.00-0.05%) iterations across calendar years for simulation C2. Therefore, scoring all YDB measurements as AMS has little to no effect on the simulated $^{14}\text{C}_E$ for Alternative Dataset_O 3. Either scenario results in a similar degree of incongruity between dataset_E and dataset_O.

In sum, scoring all measurements on AMS has a negligible effect on the degree to which the YDB and LST measurements in Alternative Dataset_O 3 are consistent with synchronicity (Figure S5.18). The LST $MPMD_O$ and $^{14}\text{C}_O$ remain within one z-score from simulated mean $MPMD_O$ and $^{14}\text{C}_O$ for simulation C2. However, unlike when these measurements are correctly scored as GPC/LSC, the A2 and B2 simulations resulted in $MPMD_O$ and $^{14}\text{C}_O$ appearing relatively inconsistent with synchronicity—they remain at least two z-scores above mean simulated $MPMD_E$ and $^{14}\text{C}_E$ (Figure S5.18). Much like the standard Alternative Dataset_O 3 simulations, when the YDB measurements are scored as entirely AMS, the simulations show that the $MPMD_O$ and $^{14}\text{C}_O$ remain at least three z-scores above mean simulated $MPMD_E$ and $^{14}\text{C}_E$ across all simulations (Figure S5.18). Regardless of whether all measurements are scored as AMS, excluding the Brohl Valley data results in LST dataset_O being more consistent with synchronicity, while the effect of excluding the Arlington Canyon data results in YDB dataset_O being marginally less consistent with synchronicity.

5.3.4. Main Dataset_O with all measurements scored as AMS

This employed the dataset_O specified in the main paper, with the lone difference being that all ^{14}C measurements were scored as AMS. This had the effect of reducing $MPMD_E$ and $^{14}\text{C}_E$ relative to $MPMD_E$ and $^{14}\text{C}_E$ presented in the main paper (compare Figures S5.19- S5.20 against Figures 4-5). However, this reduction was greater for the LST simulations than the YDB simulations. For LST simulation C2, the number of $MPMD_E$ exceeding $MPMD_O$ shrank by 74.12% after scoring all measurements as AMS. Across calendar years, expected LST $MPMD_E$ exceeded $MPMD_O$ in 114-262 of 10,000 (1.14-2.62%) simulated values when all measurements are scored as AMS. In contrast, for YDB simulation C2, the number of $MPMD_E$ exceeding $MPMD_O$ fell by 33.10% after scoring all measurements as AMS. For individual calendar years in the YDB C2 simulation, $MPMD_E$ exceeded $MPMD_O$ in 1-6 of 10,000 (0.01-0.06%) simulated values when all measurements are scored as AMS.

When all measurements are scored as AMS, $^{14}\text{C}_E$ became smaller for the LST simulations, although they may have become slightly larger for the YDB simulations (the YDB $^{14}\text{C}_E$ are slightly larger on-average when all measurements are scored as AMS, but the change is small enough where this may be due mostly to simulation variance). For LST simulation C2, the number of $^{14}\text{C}_E$ exceeding $^{14}\text{C}_O$ shrank by 58.91% after scoring all measurements as AMS. Across calendar

years, LST $^{14}\text{C}_E$ exceeded $^{14}\text{C}_0$ in 295-580 of 10,000 (2.95-5.80%) simulated values when all measurements are scored as AMS. In contrast, for YDB simulation C2, the number of $^{14}\text{C}_E$ exceeding $^{14}\text{C}_0$ increased by 42.25% after scoring all measurements as AMS. For individual calendar years in the YDB C2 simulation, $^{14}\text{C}_E$ exceeded $^{14}\text{C}_0$ in 0-5 of 10,000 (0.00-0.05%) simulated values when all measurements are scored as AMS.

The effect of scoring all measurements as AMS makes LST dataset₀ less consistent with synchronicity, while YDB dataset₀'s incongruity with synchronicity differs little from the main text dataset₀. This is a product of the fact that 100% of the LST measurements are GPC/LSC, whereas only 3 of 30 YDB measurements are GPC/LSC. With this alternative dataset₀, LST $MPMD_0$ and $^{14}\text{C}_0$ fall 2-3 z-scores above mean simulated $MPMD_E$ and $^{14}\text{C}_E$ for simulation C2 (Figure S5.21). In contrast, when measurements are correctly scored as non-AMS, $MPMD_0$ and $^{14}\text{C}_0$ rarely exceed 1.65 z-scores from mean simulated $MPMD_E$ and $^{14}\text{C}_E$ in simulation C2 (Figure 6). YDB $MPMD_0$ and $^{14}\text{C}_0$ stay at least 3 z-scores above mean simulated $MPMD_E$ and $^{14}\text{C}_E$ in simulation C2, regardless of whether all measurements are scored as AMS.

5.4. Discussion

The alternative dataset₀ simulations highlight that inferences from our simulations vary with reasonable data inclusion decisions, although the variation that we investigated here does not substantially alter the qualitative inferences presented in the main text: The observed YDB ^{14}C measurements are highly improbable, given a synchronous event. In contrast, the LST ^{14}C measurements, while not highly probable, are orders of magnitude more probable than the YDB measurements, given a synchronous event. This difference is especially interesting for Alternative Dataset₀ 2, in which YDB $MPMD_0$ is only 0.01 greater than LST $MPMD_0$, and YDB $^{14}\text{C}_0$ falls *below* LST $^{14}\text{C}_0$. This highlights the context-dependent aspect of these simulations—the degree of clustering in ^{14}C measurements that should be expected depends on many variables associated with those measurements, including their reported measurement error, the number of possible “old wood” samples, the number of laboratories that contributed measurements, and the measurement methods employed by those laboratories. Although the $MPMD_0$ and $^{14}\text{C}_0$ values for Alternative Dataset 2 might suggest that the YDB measurements are more consistent with synchronicity than are the LST measurements, aspects of YDB dataset₀ strongly suggest that they should be much more clustered than this if these measurements are associated with a synchronous event.

Inferences also necessarily change given different choices about simulation design, which are theoretically infinite. We designed the simulations to include those variables that should have the largest effects on the dispersion of ^{14}C measurements, but it is possible to imagine arguments for other variables that we excluded, or arguments for different effects associated with the variables that we did include (e.g., the OWM entails choices about which value to specify for λ , as well as the choice to model “old wood” effects with an exponential distribution). We aimed to demonstrate a range of inferences given different simulation assumptions, but this range could be further extended with other simulation designs. An important observation for these simulations is that the *expected* dispersion within a set of synchronous ^{14}C measurements generally declines when fewer sources of variability are considered. This is especially true of the laboratory variability described in the LBM. As such, we largely ignored the implications of the simulations that excluded the LBM, as it is unrealistic to expect a variety of laboratories with different protocols to measure ^{14}C with perfect precision and accuracy. Such a scenario would necessarily underestimate the amount of dispersion expected in set of ^{14}C measurements. This expectation is supported by multiple studies comparing many laboratories' ^{14}C measurements (7–12). We

displayed the results from simulations that excluded the LBM to illustrate underestimation effects on $MPMD_E$ and $^{14}C_E$ when this variability is ignored.

In addition to the inclusion or exclusion of the LBM, there is also the issue of choices in specifying the LBM (described in Section 3). Much like simulation design choices, the LBM would characterize inter- and intra-laboratory measurement variability differently under alternative specifications. We aimed to include those variables most likely to affect the dispersion of ^{14}C values in this context, although other choices might plausibly be made. For example, rather than model the effect of AMS vs GPC/LSC measurements, one could model the effects of AMS vs GPC vs LSC measurements. We lumped the latter two measurement methods together due to the amount of data available in the VIRI dataset, which is lacking when these measurements are considered separately. Additionally, for practical purposes, a primary measurement distinction commonly drawn by researchers working with ^{14}C datasets is that of AMS compared to earlier counting methods, such as GPC and LSC. As such, we incorporated this distinction into our model.

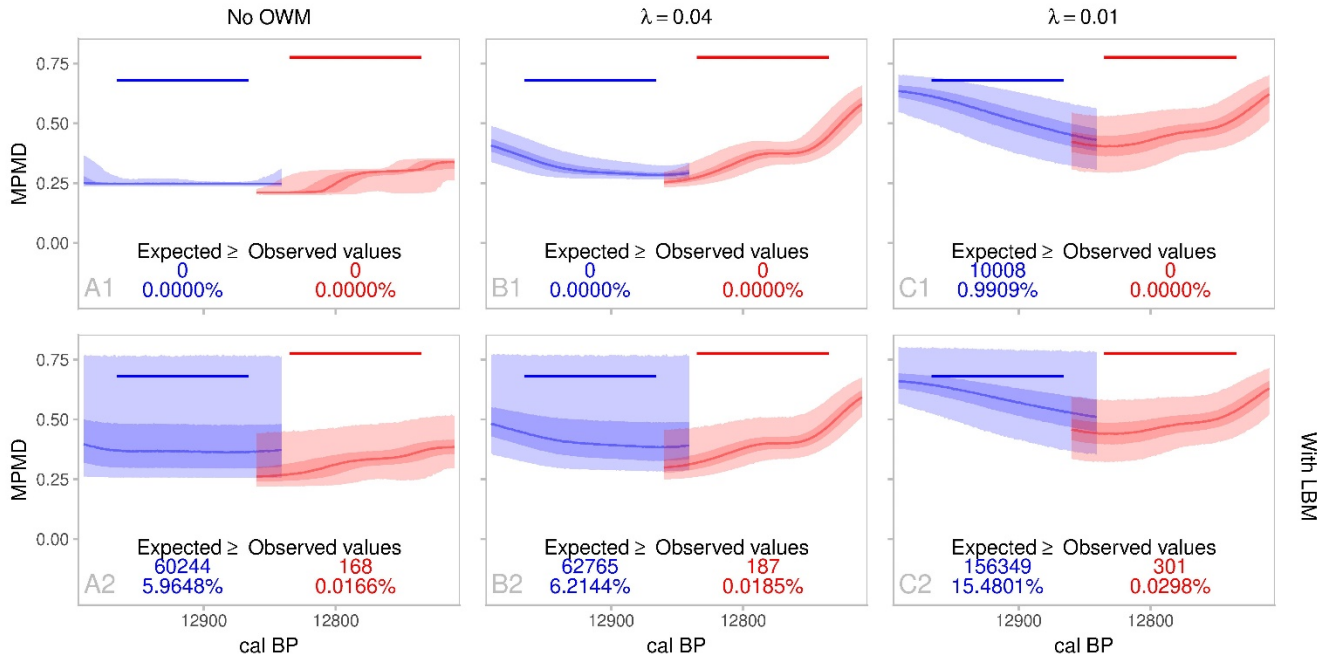


Figure S5.1. Alternative Dataset₀ 1: $MPMD_E$ distributions for the LST (blue) and YDB (red). Bands shows 50% and 95% highest density intervals and thin lines trace the modes for each distribution. Thick lines mark $MPMD_0$ across 101 possible years for each event. The top row excludes the LBM. The first column excludes the OWM, while the middle and right columns include the OWM with $\lambda = 0.04$ and 0.01 . Grey text indicates simulation name. The number and percentage of iterations where $MPMD_E$ exceeded $MPMD_0$ are displayed at the bottom of each panel. $MPMD_E$ distributions extend 25 years on either side of each range of possible years to show how expectations vary in years near the temporal ranges of interest.

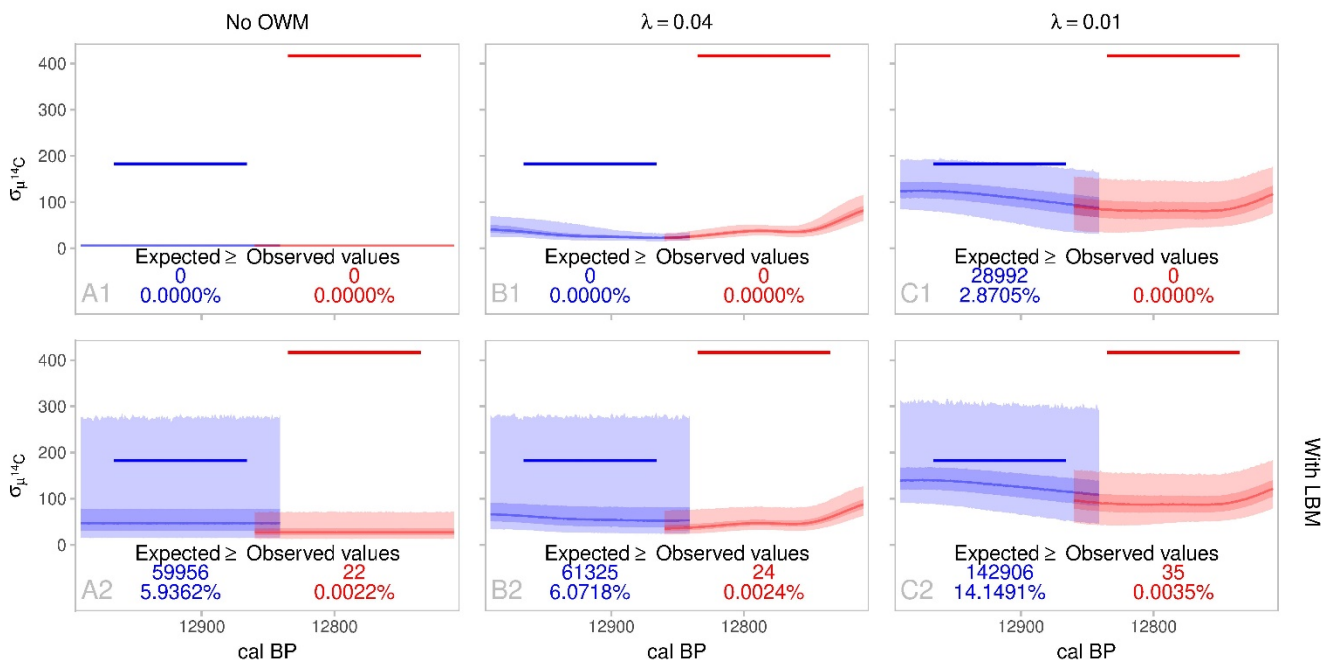


Figure S5.2. Alternative Dataset₀ 1: ${}^{14}C_E$ distributions for the LST (blue) and YDB (red). Bands shows 50% and 95% highest density intervals and thin lines trace the modes for each distribution. Thick lines mark ${}^{14}C_0$ across 101 possible years for each event. The top row excludes the LBM. The first column excludes the OWM, while the middle and right columns include the OWM with $\lambda = 0.04$ and 0.01 . Grey text indicates simulation name. The number and percentage of iterations where ${}^{14}C_E$ exceeded ${}^{14}C_0$ are displayed at the bottom of each panel. ${}^{14}C_E$ distributions extend 25 years on either side of each range of possible years to show how expectations vary in years near the temporal ranges of interest.

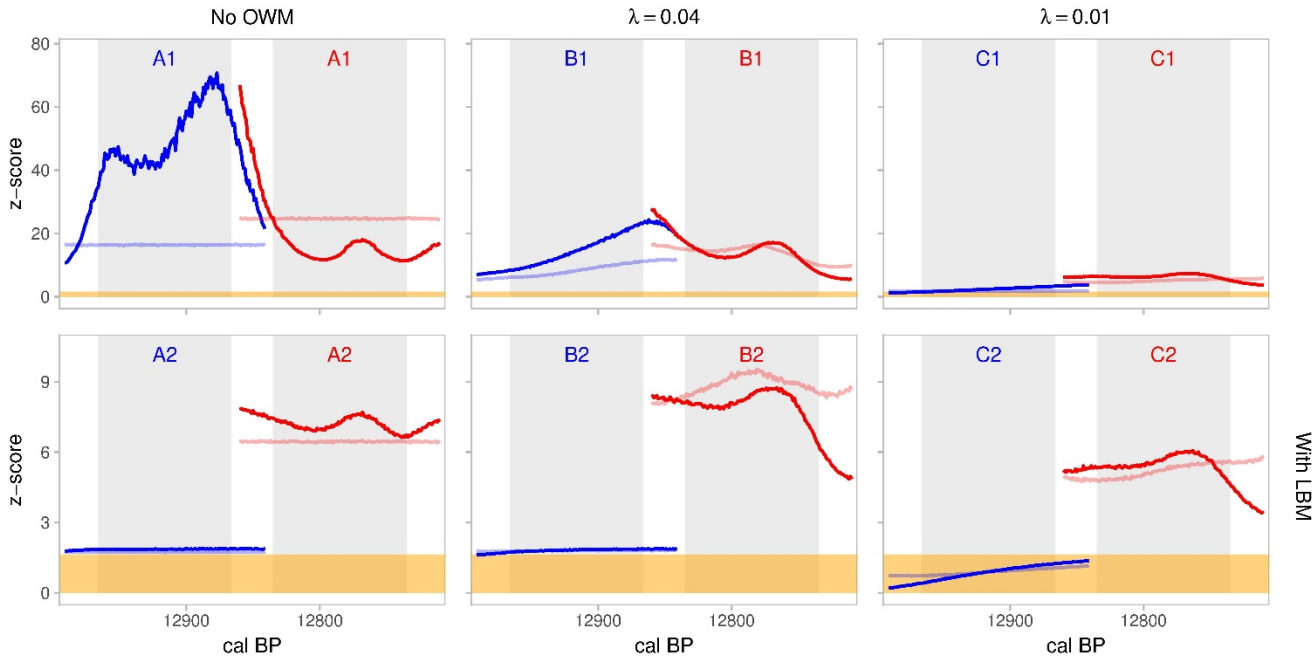


Figure S5.3. Alternative Dataset₀ 1: Distance of MPMD_E (opaque lines) and $^{14}\text{C}_E$ (transparent lines) from the mean of each simulated MPMD_E $^{14}\text{C}_E$ distribution. To approximate normality, all MPMD values are on the logit scale and all ^{14}C values are on the log scale. Blue geometry corresponds to the LST and red geometry corresponds to the YDB. Gold regions mark the lower 95% of each simulated distribution (i.e., only 5% of simulated MPMD_E and $^{14}\text{C}_E$ sit above this region). The top row of panels excludes the LBM. The first column excludes the OWM, while the middle and right columns include the OWM with $\lambda = 0.04$ and 0.01 . Note, y-axis scales change between each row of panels.

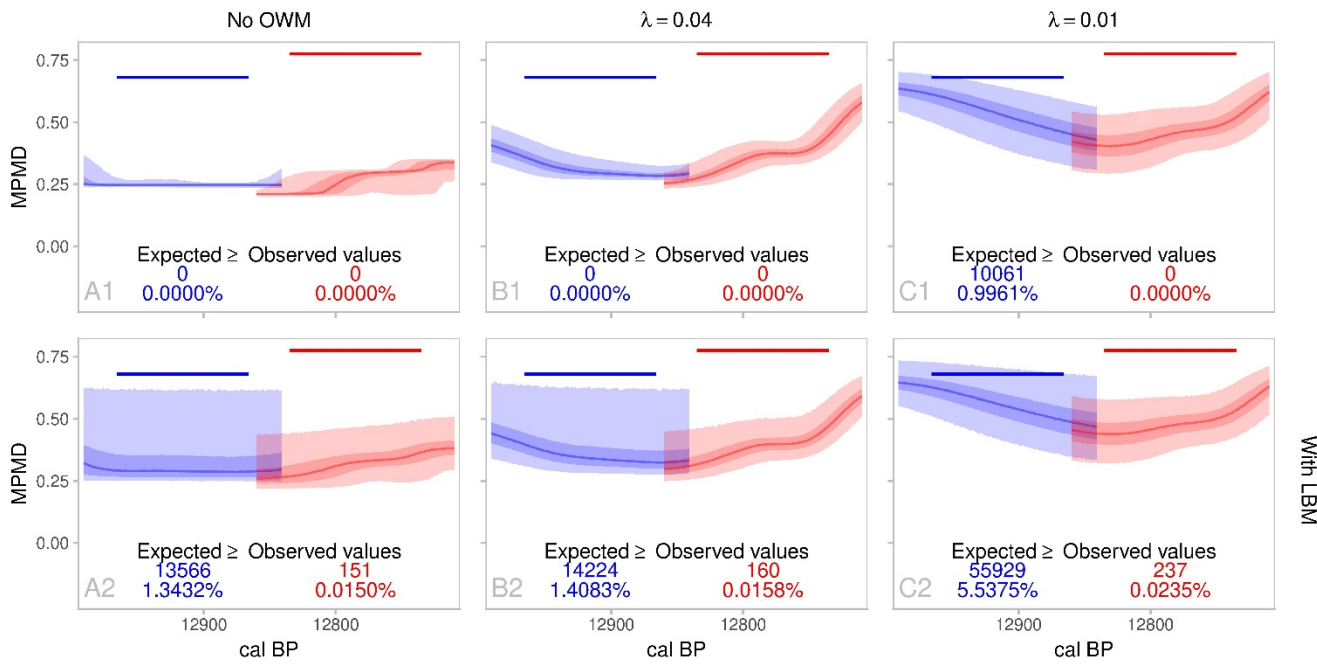


Figure S5.4. Alternative Dataset₀ 1, all measurements scored as AMS: MPMD_E distributions for the LST (blue) and YDB (red). Bands shows 50% and 95% highest density intervals and thin lines trace the modes for each distribution. Thick lines mark MPMD_O across 101 possible years for each event. The top row excludes the LBM. The first column excludes the OWM, while the middle and right columns include the OWM with $\lambda = 0.04$ and 0.01 . Grey text indicates simulation name. The number and percentage of iterations where MPMD_E exceeded MPMD_O are displayed at the bottom of each panel. MPMD_E distributions extend 25 years on either side of each range of possible years to show how expectations vary in years near the temporal ranges of interest.

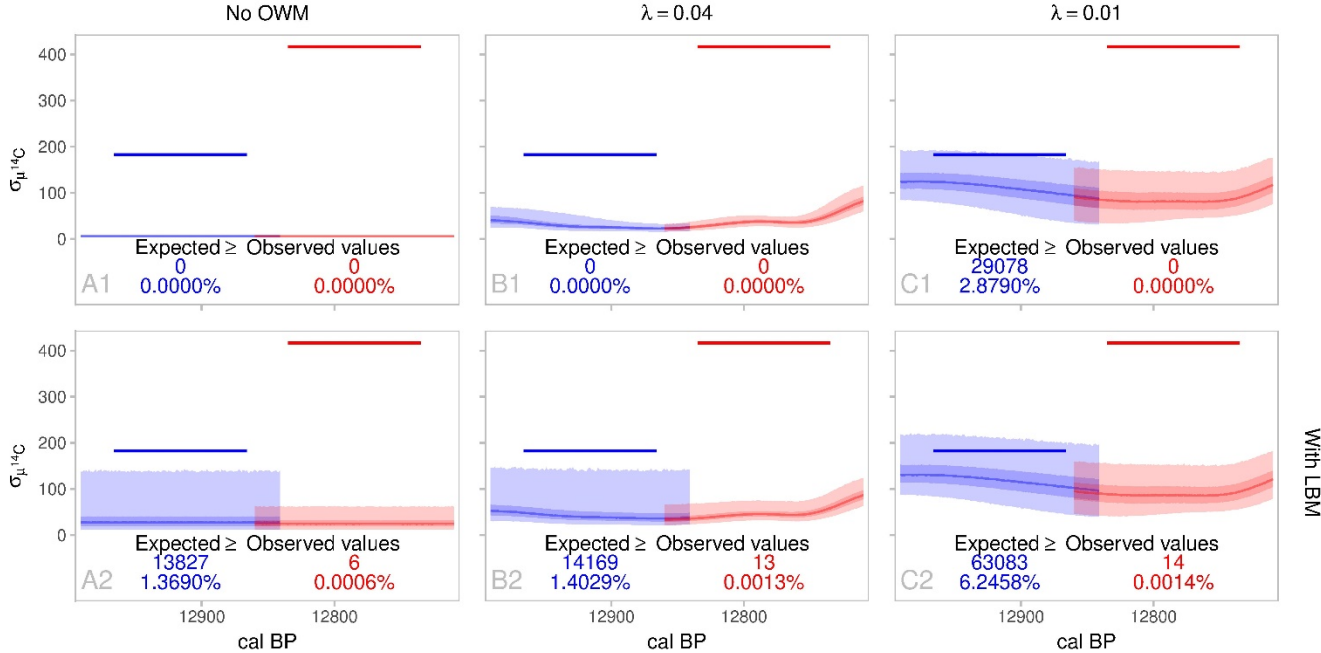


Figure S5.5. Alternative Dataseto 1, all measurements scored as AMS: $^{14}\text{C}_E$ distributions for the LST (blue) and YDB (red). Bands shows 50% and 95% highest density intervals and thin lines trace the modes for each distribution. Thick lines mark $^{14}\text{C}_E$ across 101 possible years for each event. The top row excludes the LBM. The first column excludes the OWM, while the middle and right columns include the OWM with $\lambda = 0.04$ and 0.01 . Grey text indicates simulation name. The number and percentage of iterations where $^{14}\text{C}_E$ exceeded $^{14}\text{C}_O$ are displayed at the bottom of each panel. $^{14}\text{C}_E$ distributions extend 25 years on either side of each range of possible years to show how expectations vary in years near the temporal ranges of interest.

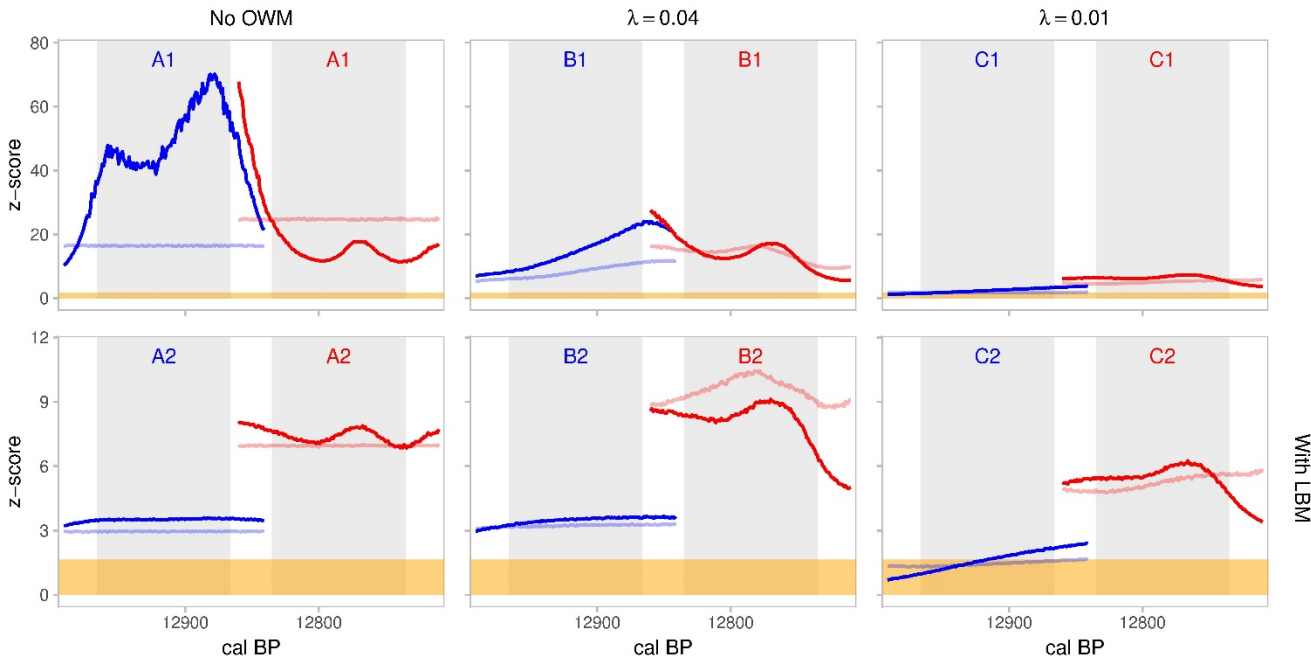


Figure S5.6. Alternative Dataseto 1, all measurements scored as AMS: Distance of MPMD_O (opaque lines) and $^{14}\text{C}_E$ (transparent lines) from the mean of each simulated MPMD_E $^{14}\text{C}_E$ distribution. To approximate normality, all MPMD values are on the logit scale and all $^{14}\text{C}_E$ values are on the log scale. Blue geometry corresponds to the LST and red geometry corresponds to the YDB. Gold regions mark the lower 95% of each simulated distribution (i.e., only 5% of simulated MPMD_E and $^{14}\text{C}_E$ sit above this region). The top row of panels excludes the LBM. The first column excludes the OWM, while the middle and right columns include the OWM with $\lambda = 0.04$ and 0.01 . Note, y-axis scales change between each row of panels.



Figure S5.7. Alternative Dataset₂: $MPMD_E$ distributions for the LST (blue) and YDB (red). Bands shows 50% and 95% highest density intervals and thin lines trace the modes for each distribution. Thick lines mark $MPMD_0$ across 101 possible years for each event. The top row excludes the LBM. The first column excludes the OWM, while the middle and right columns include the OWM with $\lambda = 0.04$ and 0.01 . Grey text indicates simulation name. The number and percentage of iterations where $MPMD_E$ exceeded $MPMD_0$ are displayed at the bottom of each panel. $MPMD_E$ distributions extend 25 years on either side of each range of possible years to show how expectations vary in years near the temporal ranges of interest.

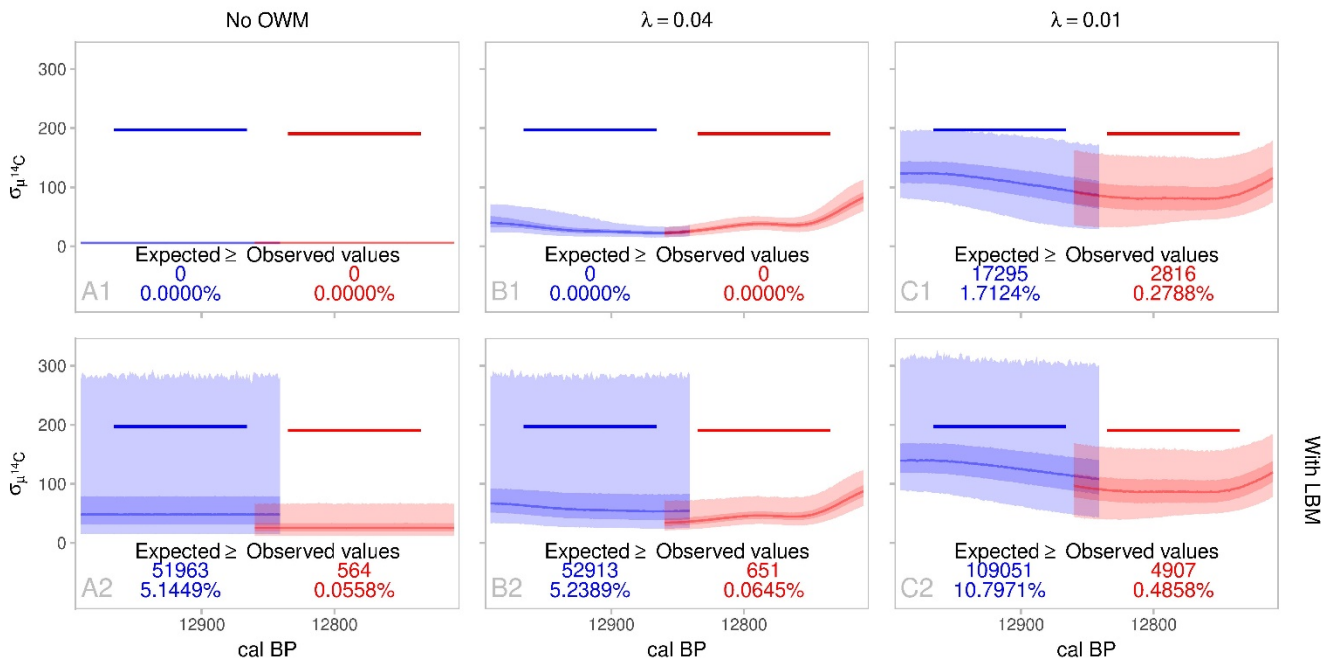


Figure S5.8. Alternative Dataset₂: $^{14}C_E$ distributions for the LST (blue) and YDB (red). Bands shows 50% and 95% highest density intervals and thin lines trace the modes for each distribution. Thick lines mark $^{14}C_0$ across 101 possible years for each event. The top row excludes the LBM. The first column excludes the OWM, while the middle and right columns include the OWM with $\lambda = 0.04$ and 0.01 . Grey text indicates simulation name. The number and percentage of iterations where $^{14}C_E$ exceeded $^{14}C_0$ are displayed at the bottom of each panel. $^{14}C_E$ distributions extend 25 years on either side of each range of possible years to show how expectations vary in years near the temporal ranges of interest.

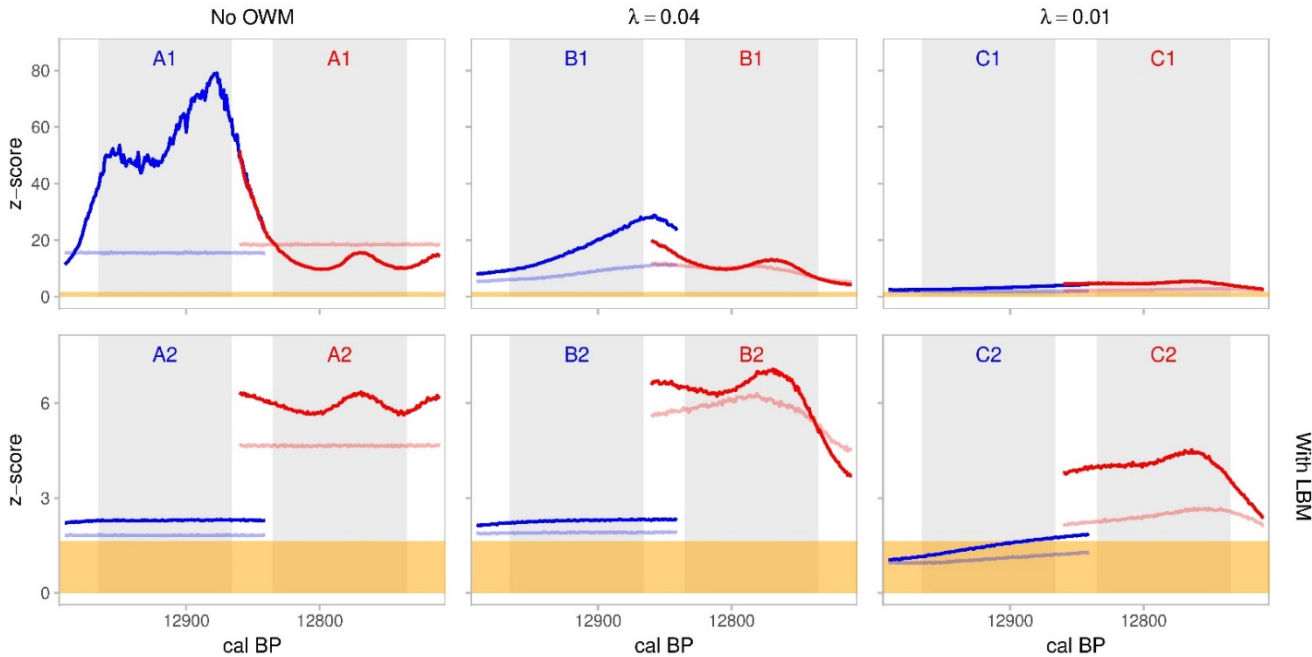


Figure S5.9. Alternative Dataset 2: Distance of MPMD_O (opaque lines) and ¹⁴C_E (transparent lines) from the mean of each simulated MPMD_E ¹⁴C_E distribution. To approximate normality, all MPMD values are on the logit scale and all ¹⁴C values are on the log scale. Blue geometry corresponds to the LST and red geometry corresponds to the YDB. Gold regions mark the lower 95% of each simulated distribution (i.e., only 5% of simulated MPMD_E and ¹⁴C_E sit above this region). The top row of panels excludes the LBM. The first column excludes the OWM, while the middle and right columns include the OWM with $\lambda = 0.04$ and 0.01 . Note, y-axis scales change between each row of panels.

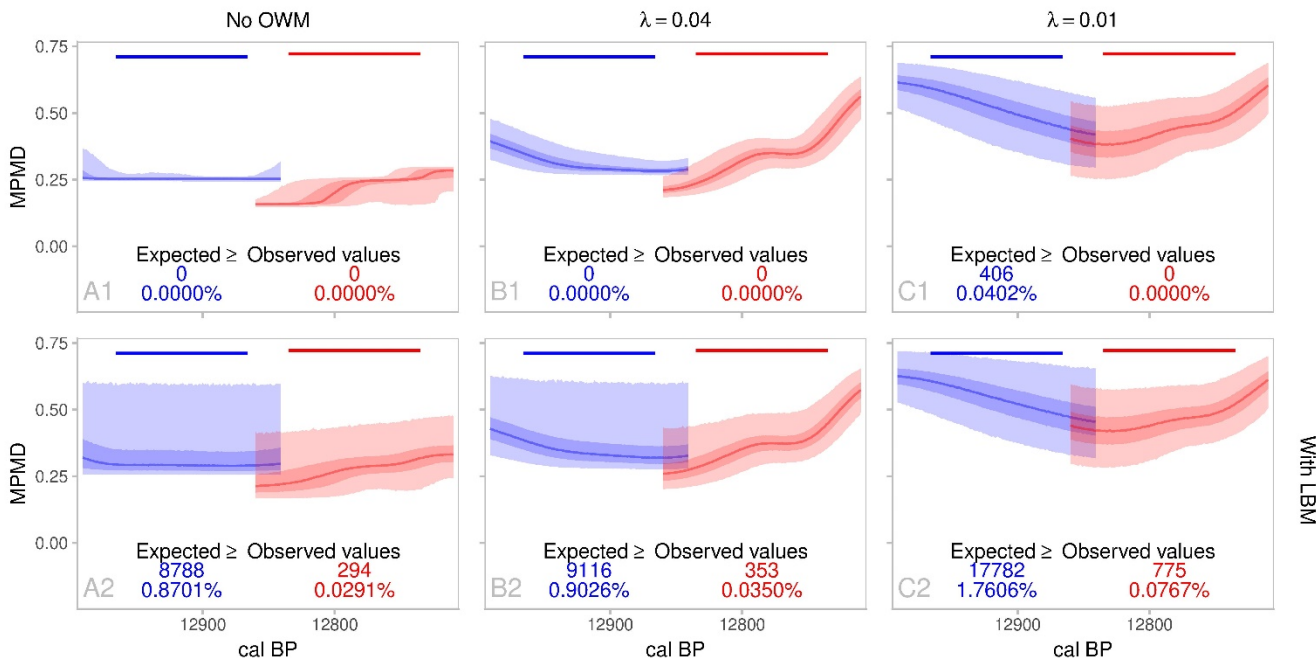


Figure S5.10. Alternative Dataset 2, all measurements scored as AMS: MPMD_E distributions for the LST (blue) and YDB (red). Bands shows 50% and 95% highest density intervals and thin lines trace the modes for each distribution. Thick lines mark MPMD_O across 101 possible years for each event. The top row excludes the LBM. The first column excludes the OWM, while the middle and right columns include the OWM with $\lambda = 0.04$ and 0.01 . Grey text indicates simulation name. The number and percentage of iterations where MPMD_E exceeded MPMD_O are displayed at the bottom of each panel. MPMD_E distributions extend 25 years on either side of each range of possible years to show how expectations vary in years near the temporal ranges of interest.

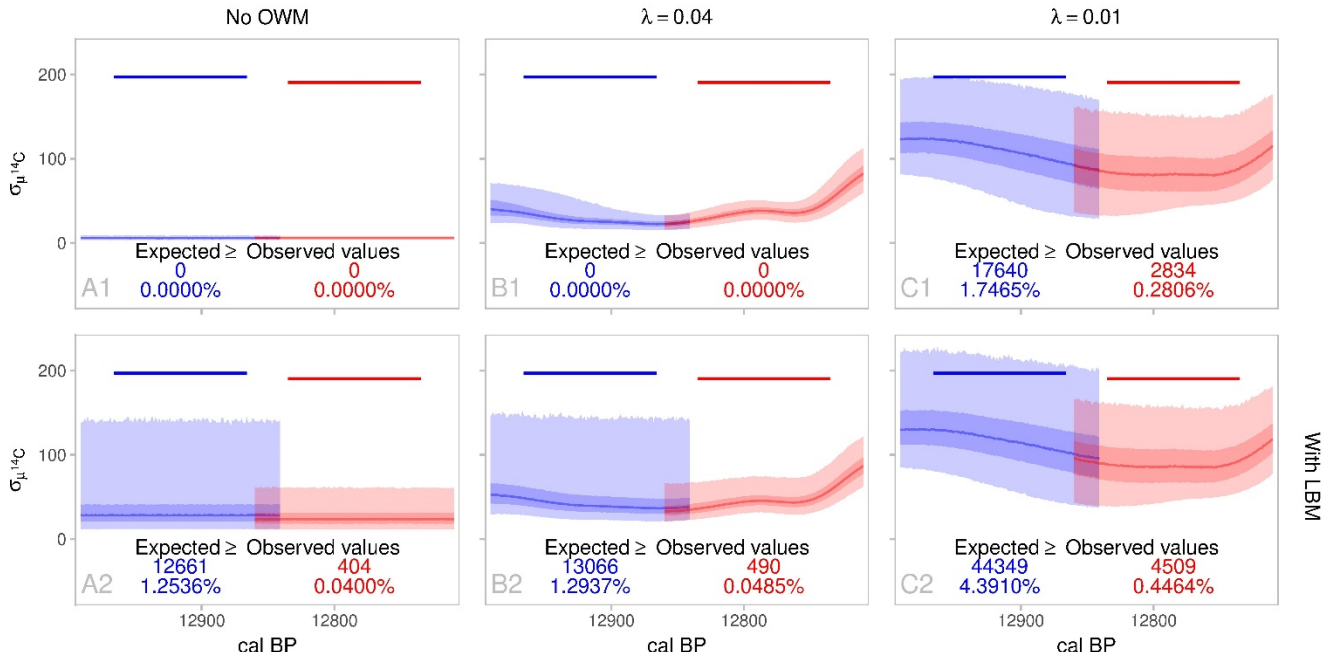


Figure S5.11. Alternative Dataseto 2, all measurements scored as AMS: $^{14}C_E^Q$ distributions for the LST (blue) and YDB (red). Bands shows 50% and 95% highest density intervals and thin lines trace the modes for each distribution. Thick lines mark $^{14}C_E^Q$ across 101 possible years for each event. The top row excludes the LBM. The first column excludes the OWM, while the middle and right columns include the OWM with $\lambda = 0.04$ and 0.01 . Grey text indicates simulation name. The number and percentage of iterations where $^{14}C_E^Q$ exceeded $^{14}C_O^Q$ are displayed at the bottom of each panel. $^{14}C_E^Q$ distributions extend 25 years on either side of each range of possible years to show how expectations vary in years near the temporal ranges of interest.

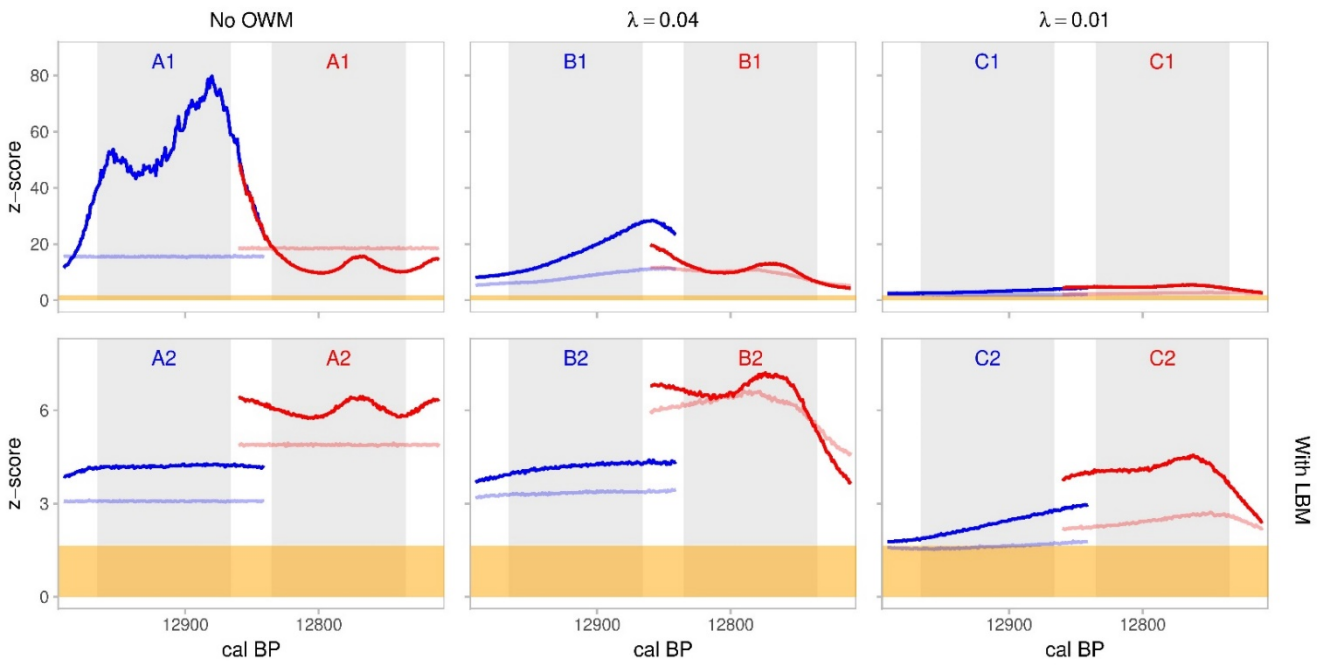


Figure S5.12. Alternative Dataseto 2, all measurements scored as AMS: Distance of MPMD_E (opaque lines) and $^{14}C_E^Q$ (transparent lines) from the mean of each simulated MPMD_E $^{14}C_E^Q$ distribution. To approximate normality, all MPMD values are on the logit scale and all ^{14}C values are on the log scale. Blue geometry corresponds to the LST and red geometry corresponds to the YDB. Gold regions mark the lower 95% of each simulated distribution (i.e., only 5% of simulated MPMD_E and $^{14}C_E^Q$ sit above this region). The top row of panels excludes the LBM. The first column excludes the OWM, while the middle and right columns include the OWM with $\lambda = 0.04$ and 0.01 . Note, y-axis scales change between each row of panels.

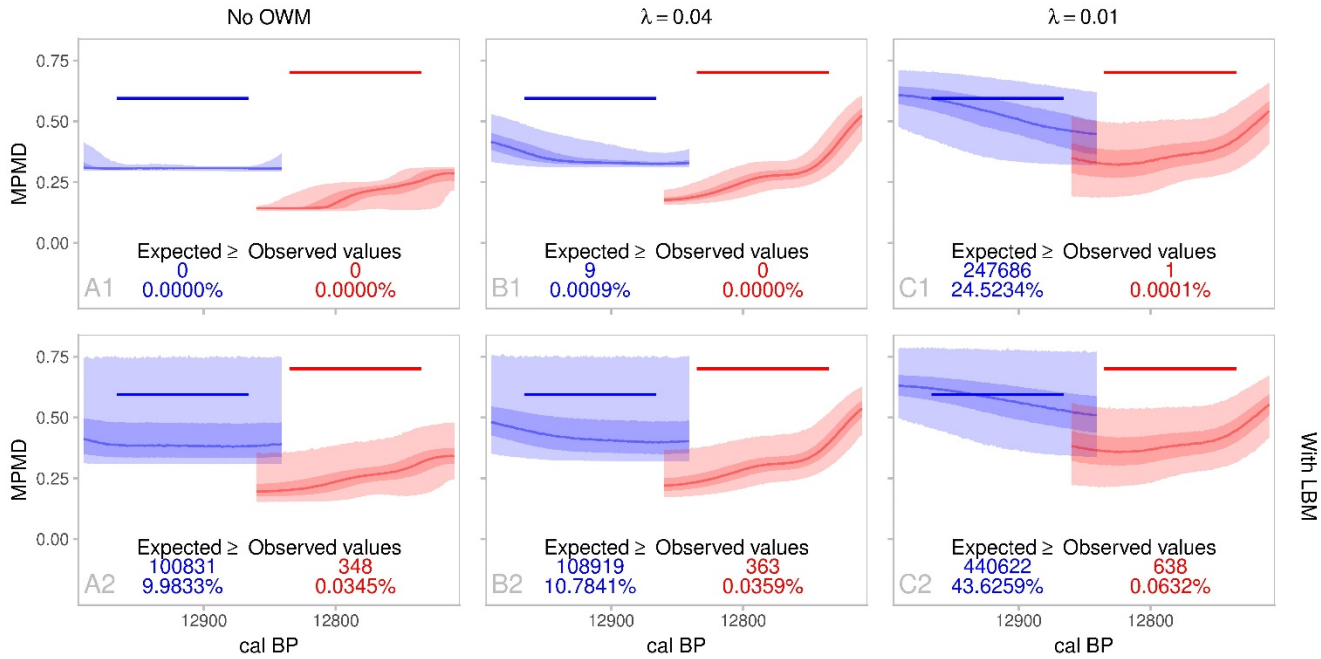


Figure S5.13. Alternative Dataset₀ 3: $MPMD_E$ distributions for the LST (blue) and YDB (red). Bands shows 50% and 95% highest density intervals and thin lines trace the modes for each distribution. Thick lines mark $MPMD_0$ across 101 possible years for each event. The top row excludes the LBM. The first column excludes the OWM, while the middle and right columns include the OWM with $\lambda = 0.04$ and 0.01 . Grey text indicates simulation name. The number and percentage of iterations where $MPMD_E$ exceeded $MPMD_0$ are displayed at the bottom of each panel. $MPMD_E$ distributions extend 25 years on either side of each range of possible years to show how expectations vary in years near the temporal ranges of interest.

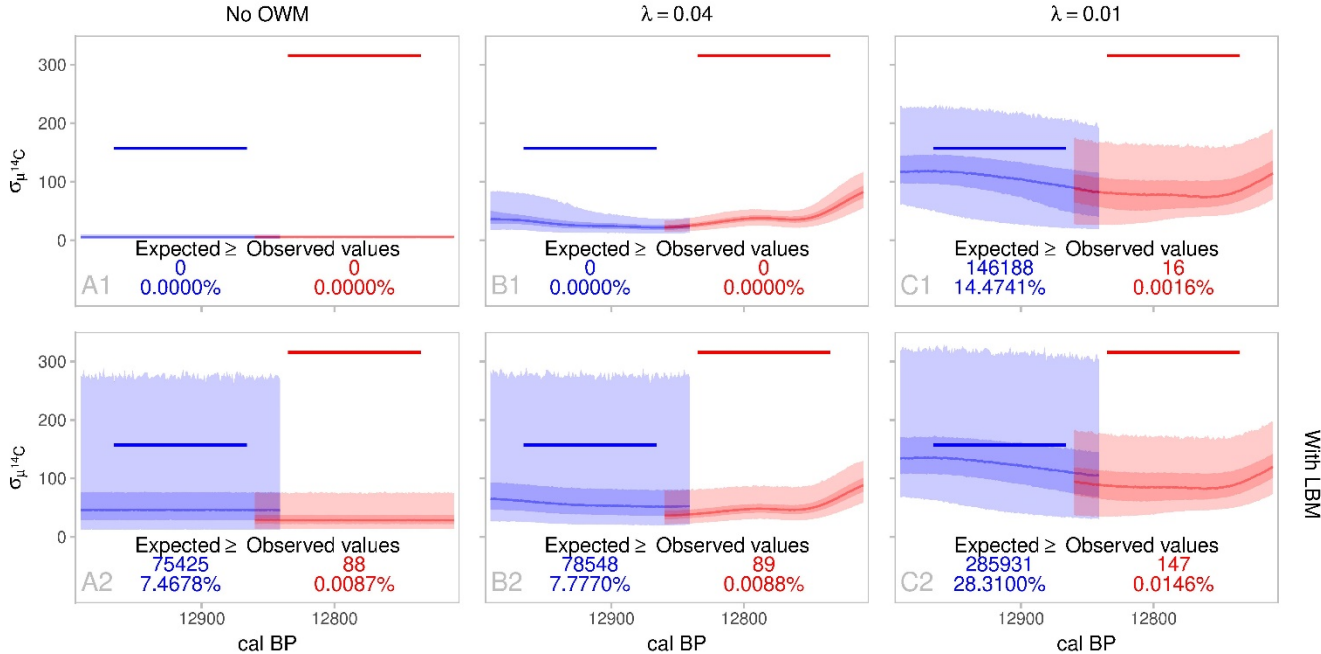


Figure S5.14. Alternative Dataset₀ 3: $^{14}C_E^\sigma$ distributions for the LST (blue) and YDB (red). Bands shows 50% and 95% highest density intervals and thin lines trace the modes for each distribution. Thick lines mark $^{14}C_0^\sigma$ across 101 possible years for each event. The top row excludes the LBM. The first column excludes the OWM, while the middle and right columns include the OWM with $\lambda = 0.04$ and 0.01 . Grey text indicates simulation name. The number and percentage of iterations where $^{14}C_E^\sigma$ exceeded $^{14}C_0^\sigma$ are displayed at the bottom of each panel. $^{14}C_E^\sigma$ distributions extend 25 years on either side of each range of possible years to show how expectations vary in years near the temporal ranges of interest.

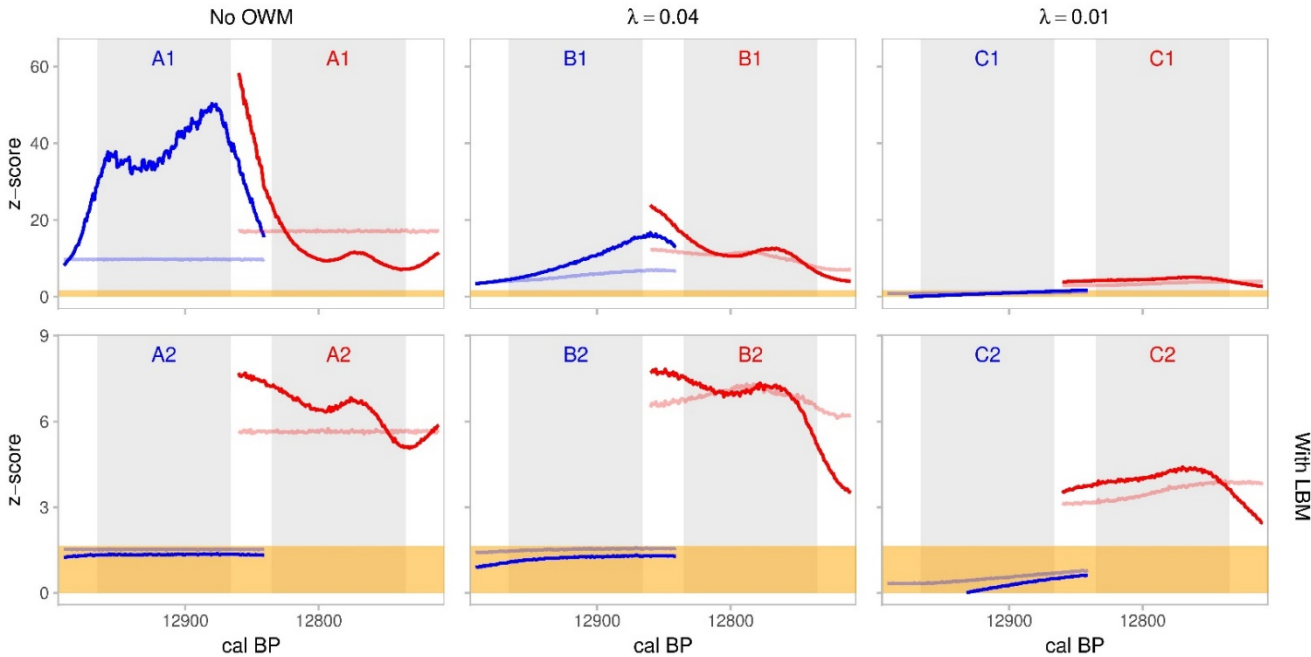


Figure S5.15. Alternative Dataset₃: Distance of MPMD₀ (opaque lines) and ¹⁴C_E (transparent lines) from the mean of each simulated MPMD_E ¹⁴C_E distribution. To approximate normality, all MPMD values are on the logit scale and all ¹⁴C values are on the log scale. Blue geometry corresponds to the LST and red geometry corresponds to the YDB. Gold regions mark the lower 95% of each simulated distribution (i.e., only 5% of simulated MPMD_E and ¹⁴C_E sit above this region). The top row of panels excludes the LBM. The first column excludes the OWM, while the middle and right columns include the OWM with $\lambda = 0.04$ and 0.01 . Note, y-axis scales change between each row of panels.

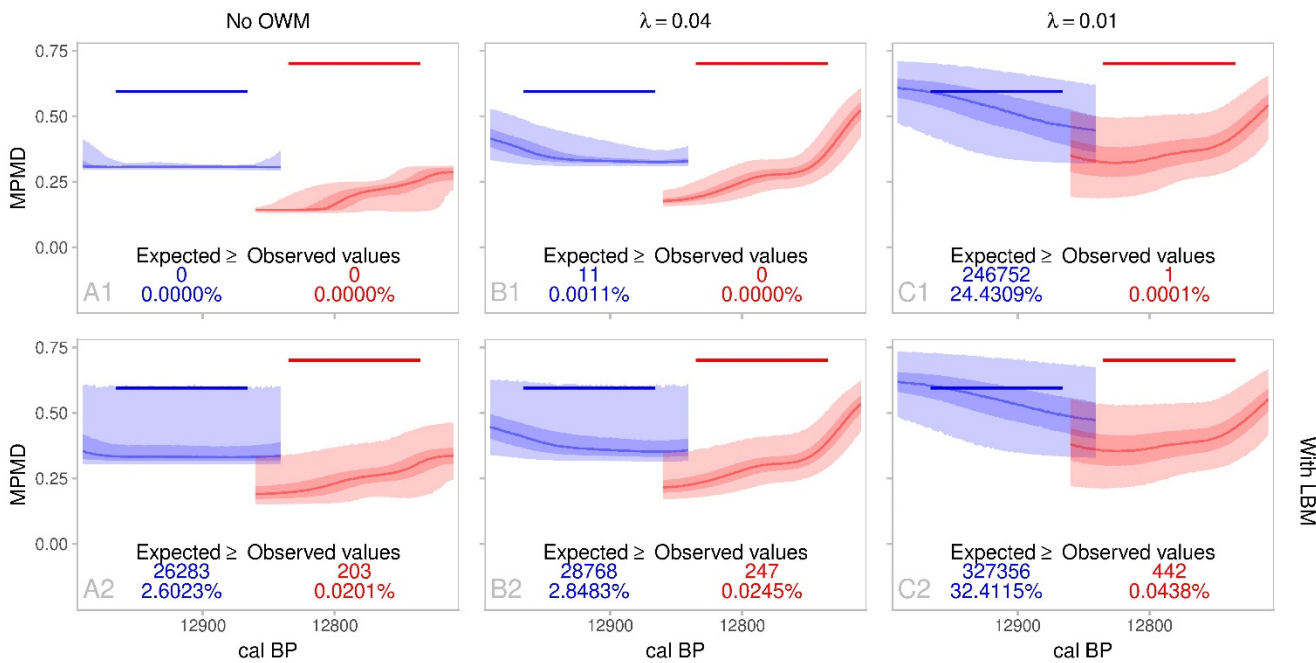


Figure S5.16. Alternative Dataset₃, all measurements scored as AMS: MPMD_E distributions for the LST (blue) and YDB (red). Bands shows 50% and 95% highest density intervals and thin lines trace the modes for each distribution. Thick lines mark MPMD₀ across 101 possible years for each event. The top row excludes the LBM. The first column excludes the OWM, while the middle and right columns include the OWM with $\lambda = 0.04$ and 0.01 . Grey text indicates simulation name. The number and percentage of iterations where MPMD_E exceeded MPMD₀ are displayed at the bottom of each panel. MPMD_E distributions extend 25 years on either side of each range of possible years to show how expectations vary in years near the temporal ranges of interest.

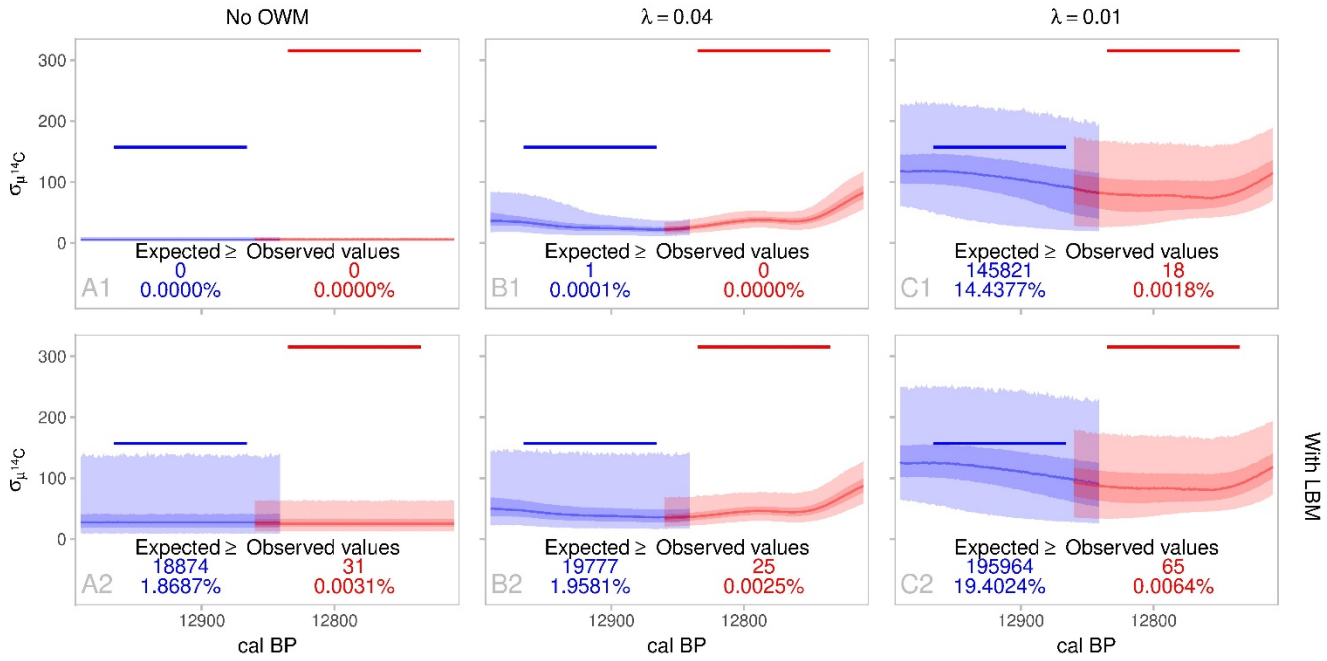


Figure S5.17. Alternative Dataset₀ 3, all measurements scored as AMS: $^{14}\text{C}_E^\alpha$ distributions for the LST (blue) and YDB (red). Bands shows 50% and 95% highest density intervals and thin lines trace the modes for each distribution. Thick lines mark $^{14}\text{C}_E^\alpha$ across 101 possible years for each event. The top row excludes the LBM. The first column excludes the OWM, while the middle and right columns include the OWM with $\lambda = 0.04$ and 0.01 . Grey text indicates simulation name. The number and percentage of iterations where $^{14}\text{C}_E^\alpha$ exceeded $^{14}\text{C}_O^\alpha$ are displayed at the bottom of each panel. $^{14}\text{C}_E^\alpha$ distributions extend 25 years on either side of each range of possible years to show how expectations vary in years near the temporal ranges of interest.

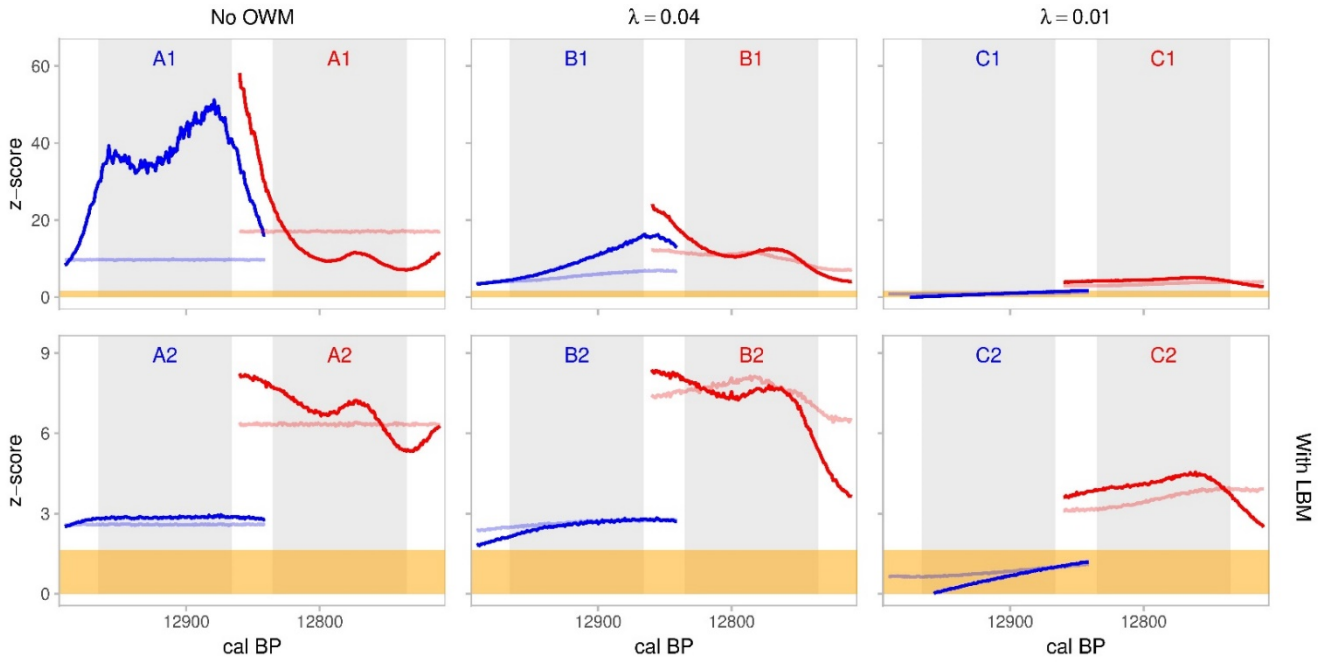


Figure S5.18. Alternative Dataset₀ 3, all measurements scored as AMS: Distance of MPMD₀ (opaque lines) and $^{14}\text{C}_O^\alpha$ (transparent lines) from the mean of each simulated MPMD_E $^{14}\text{C}_E^\alpha$ distribution. To approximate normality, all MPMD values are on the logit scale and all $^{14}\text{C}^\alpha$ values are on the log scale. Blue geometry corresponds to the LST and red geometry corresponds to the YDB. Gold regions mark the lower 95% of each simulated distribution (i.e., only 5% of simulated MPMD_E and $^{14}\text{C}_E^\alpha$ sit above this region). The top row of panels excludes the LBM. The first column excludes the OWM, while the middle and right columns include the OWM with $\lambda = 0.04$ and 0.01 . Note, y-axis scales change between each row of panels.

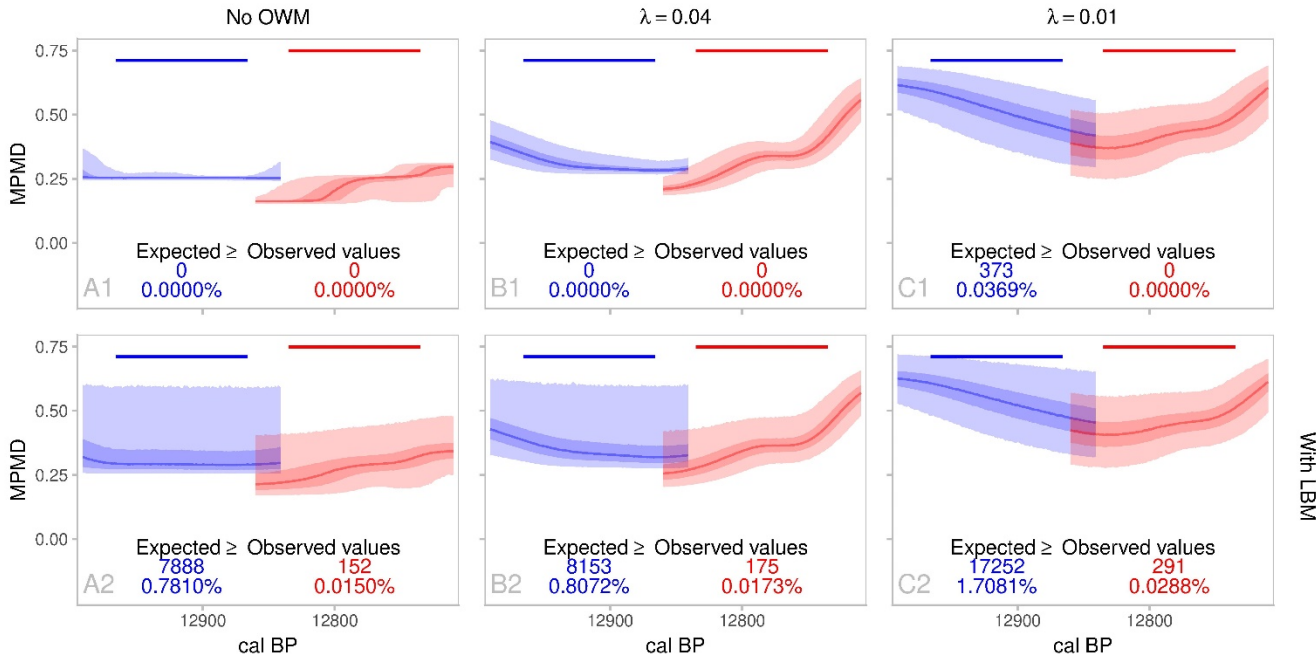


Figure S5.19. Main text dataset₀, all measurements as AMS: $MPMD_E$ distributions for the LST (blue) and YDB (red). Bands shows 50% and 95% highest density intervals and thin lines trace the modes for each distribution. Thick lines mark $MPMD_0$ across 101 possible years for each event. The top row excludes the LBM. The first column excludes the OWM, while the middle and right columns include the OWM with $\lambda = 0.04$ and 0.01 . Grey text indicates simulation name. The number and percentage of iterations where $MPMD_E$ exceeded $MPMD_0$ are displayed at the bottom of each panel. $MPMD_E$ distributions extend 25 years on either side of each range of possible years to show how expectations vary in years near the temporal ranges of interest.

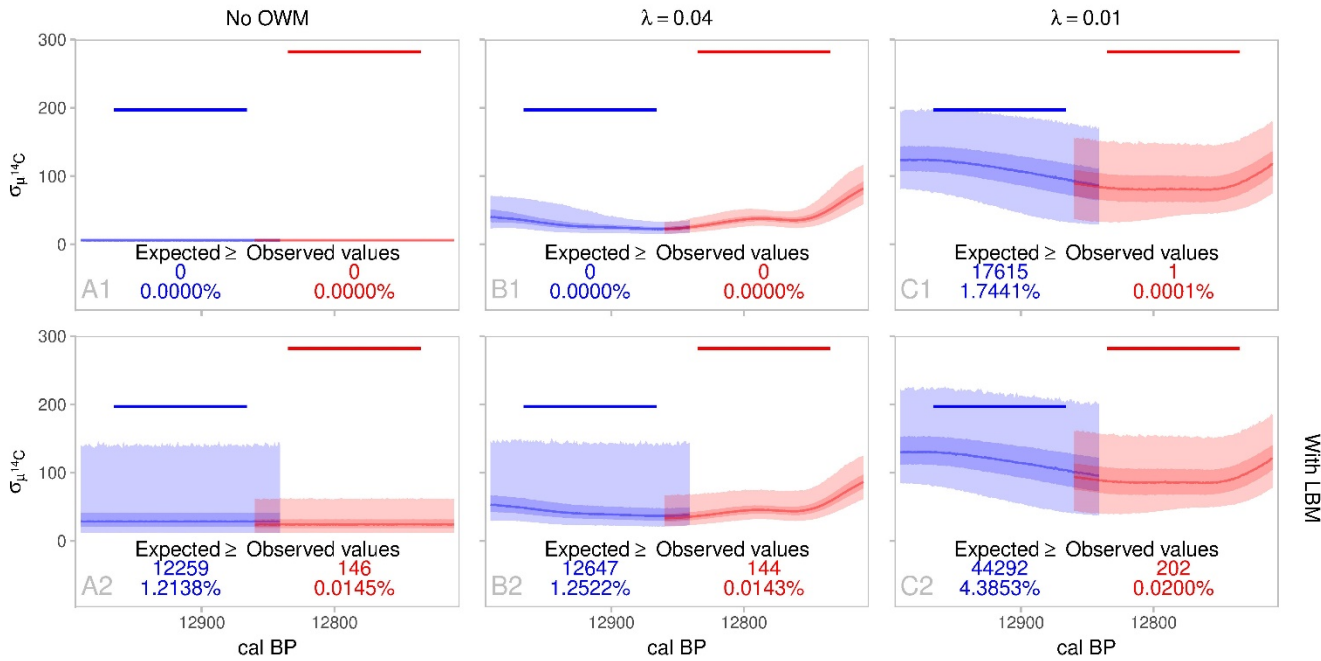


Figure S5.20. Main text dataset₀, all measurements as AMS: $^{14}C_E$ distributions for the LST (blue) and YDB (red). Bands shows 50% and 95% highest density intervals and thin lines trace the modes for each distribution. Thick lines mark $^{14}C_0$ across 101 possible years for each event. The top row excludes the LBM. The first column excludes the OWM, while the middle and right columns include the OWM with $\lambda = 0.04$ and 0.01 . Grey text indicates simulation name. The number and percentage of iterations where $^{14}C_E$ exceeded $^{14}C_0$ are displayed at the bottom of each panel. $^{14}C_E$ distributions extend 25 years on either side of each range of possible years to show how expectations vary in years near the temporal ranges of interest.

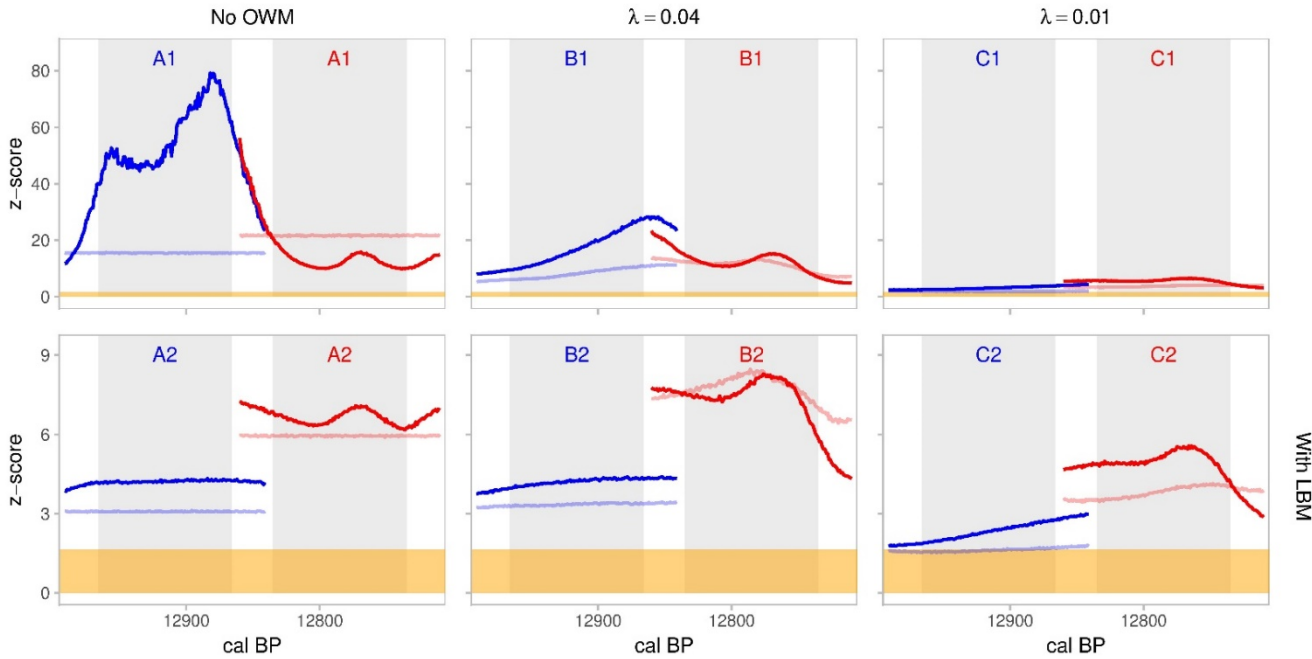


Figure S5.21. Main text dataset₀, all measurements as AMS: Distance of MPMD_O (opaque lines) and $^{14}\text{C}_E$ (transparent lines) from the mean of each simulated MPMD_E $^{14}\text{C}_E^T$ distribution. To approximate normality, all MPMD values are on the logit scale and all ^{14}C values are on the log scale. Blue geometry corresponds to the LST and red geometry corresponds to the YDB. Gold regions mark the lower 95% of each simulated distribution (i.e., only 5% of simulated MPMD_E and $^{14}\text{C}_E^T$ sit above this region). The top row of panels excludes the LBM. The first column excludes the OWM, while the middle and right columns include the OWM with $\lambda = 0.04$ and 0.01 . Note, y-axis scales change between each row of panels.

6. References for Supplemental Information Appendix

1. Reimer PJ, et al. (2013) IntCal13 and Marine13 radiocarbon age calibration curves 0–50,000 years cal BP. *Radiocarbon* 55(4):1869–1887.
2. Baales M, et al. (2002) Impact of the Late Glacial Eruption of the Laacher See Volcano, Central Rhineland, Germany. *Quat Res* 58(03):273–288.
3. Caudullo G, de Rigo D (2016) *Populus tremula* in Europe: distribution, habitat, usage and threats. *European Atlas of Forest Tree Species.*, eds San-Miguel-Ayanz J, de Rigo D, Caudullo G, Houston T, Mauri A (Publication Office of the European Union, Luxembourg), pp 138–139.
4. von Wühlisch G (2009) *EUFORGEN Technical Guidelines for genetic conservation and use for Eurasian aspen (Populus tremula)* (Biodiversity International, Rome).
5. Bevan A, Crema ER (2018) *rcarbon v1.2.0: Methods for calibrating and analyzing radiocarbon dates* Available at: <https://CRAN.R-project.org/package=rcarbon>.
6. McDonald L, Chivall D, Miles D, Bronk Ramsey C (2018) Seasonal variations in the ^{14}C content of tree rings: influences on radiocarbon calibration and single-year curve construction. *Radiocarbon*:1–10.
7. Scott EM, Cook GT, Naysmith P (2010) The Fifth International Radiocarbon Intercomparison (VIRI): An Assessment of Laboratory Performance in Stage 3. *Radiocarbon* 52(03):859–865.
8. Boaretto E, et al. (2003) How reliable are radiocarbon laboratories? A report on the Fourth International Radiocarbon Inter-comparison (FIRI)(1998–2001). *Antiquity* 77(295):146–154.
9. Scott EM, Aitchison TC, Harkness DD, Cook GT, Baxter MS (1990) An Overview of All Three Stages of the International Radiocarbon Intercomparison. *Radiocarbon* 32(03):309–319.
10. Scott EM, Harkness DD, Cook Gt (1998) Interlaboratory comparisons: lessons learned. *Radiocarbon* 40(1):331–340.
11. International Study Group, et al. (1982) An inter-laboratory comparison of radiocarbon measurements in tree rings. *Nature* 298:619–623.
12. Scott EM, Cook GT, Naysmith P (2007) Error and Uncertainty in Radiocarbon Measurements. *Radiocarbon* 49(02):427–440.
13. Scott EM, Cook GT, Naysmith P, Bryant C, O'Donnell D (2007) A Report on Phase 1 of the 5th International Radiocarbon Intercomparison (VIRI). *Radiocarbon* 49(02):409–426.
14. Scott EM, Cook GT, Naysmith P (2010) A Report on Phase 2 of the Fifth International Radiocarbon Intercomparison (VIRI). *Radiocarbon* 52(03):846–858.
15. Stan Development Team (2018) *RStan 2.17.2: The R interface for Stan* Available at: <http://mc-stan.org>.

16. Wickham H (2016) *ggplot2: Elegant Graphics for Data Analysis* (Springer-Verlag, New York).
17. R Core Team (2018) *R: A language and environment for statistical computing*. (R Foundation for Statistical Computing, Vienna, Austria) Available at: URL <http://www.R-project.org/>.
18. Wickham H (2007) Reshaping data with the reshape package. *Journal of Statistical Software* 21(12):1–20.
19. Bengtsson H, et al. (2018) *matrixStats: Functions that Apply to Rows and Columns of Matrices (and to Vectors)* Available at: <https://cran.rstudio.com/web/packages/matrixStats/index.html>.
20. Pedersen TL (2018) *patchwork: The Composer of ggplots*.
21. McElreath R (2016) *rethinking v1.59: Statistical Rethinking book package* Available at: <https://www.github.com/user/rmcelreath/rethinking>.
22. McElreath R (2017) *rethinking v1.59: Statistical Rethinking book package* Available at: <https://www.github.com/user/rmcelreath/rethinking>.
23. Kennett JP, et al. (2015) Bayesian chronological analyses consistent with synchronous age of 12,835–12,735 Cal B.P. for Younger Dryas boundary on four continents. *Proc Natl Acad Sci USA* 112(32):E4344–E4353.
24. Wittke JH, et al. (2013) Evidence for deposition of 10 million tonnes of impact spherules across four continents 12,800 y ago. *Proc Natl Acad Sci USA* 110(23):E2088–E2097.
25. Bunch TE, et al. (2012) Very high-temperature impact melt products as evidence for cosmic airbursts and impacts 12,900 years ago. *Proc Natl Acad Sci USA* 109(28):E1903–E1912.
26. Bunch TE, et al. (2012) Very high-temperature impact melt products as evidence for cosmic airbursts and impacts 12,900 years ago. *Proc Natl Acad Sci USA* 109(28):E1903–E1912.
27. Moore AMT, Hillman GC, Legge AJ, Huxtable J (2000) *Village on the Euphrates: from foraging to farming at Abu Hureyra* (Oxford University Press, Oxford).
28. Kennett D, et al. (2008) Wildfire and abrupt ecosystem disruption on California’s Northern Channel Islands at the Ållerød–Younger Dryas boundary (13.0–12.9ka). *Quat Sci Rev* 27(27–28):2530–2545.
29. Hajic ER, Mandel RD, Ray JH, Lopinot NH (2007) Geoarchaeology of stratified paleoindian deposits at the Big Eddy site, Southwest Missouri, U.S.A. *Geoarchaeology* 22(8):891–934.
30. Lopinot NH, Ray JH, Conner MD (1998) *The 1997 Excavations at the Big Eddy site (23CE426) in southwest Missouri* (Southwest Missouri State University, Springfield, Missouri).
31. Lopinot NH, Ray JH, Connor MD (2000) *The 1999 Excavations at the Big Eddy Site (23CE426)* (Southwest Missouri State University).
32. Johnson E, Holliday VT (1997) Analysis of Paleoindian bonebeds at the Clovis Site: New data from old excavations. *Plains Anthropologist* 42:329–352.

33. Bement LC, et al. (2014) Quantifying the distribution of nanodiamonds in pre-Younger Dryas to recent age deposits along Bull Creek, Oklahoma Panhandle, USA. *Proc Natl Acad Sci USA* 111(5):1726–1731.
34. van Hoesel A, et al. (2012) Nanodiamonds and wildfire evidence in the Usselo horizon postdate the Allerod-Younger Dryas boundary. *Proc Natl Acad Sci USA* 109(20):7648–7653.
35. Firestone RB, et al. (2007) Evidence for an extraterrestrial impact 12,900 years ago that contributed to the megafaunal extinctions and the Younger Dryas cooling. *Proc Natl Acad Sci USA* 104(41):16016–16021.
36. Haynes V, Agogino G (1960) Geological significance of a new radiocarbon date from the Lindenmeier site. *Proceedings No. 9* (Denver Museum of Natural History).
37. Kinzie CR, et al. (2014) Nanodiamond-Rich Layer across Three Continents Consistent with Major Cosmic Impact at 12,800 Cal BP. *J Geol* 122(5):475–506.
38. Walton A, Trautman MA, Friend JP (1961) Isotopes, Inc. Radiocarbon Measurements I. *Radiocarbon* 3:47–59.
39. van Geel P, Coope GR, van der Hammen T (1989) Palaeoecology and stratigraphy of the late glacial type section at Usselo (The Netherlands). *Review of Paleobotany and Palynology* 60:25–129.
40. Haynes CV (2007) Radiocarbon dating at Murray Springs and Curry Draw. *Murray Springs: A Clovis Site with Multiple Activity Areas in the San Pedro Valley, Arizona*, eds Haynes CV, Huckell BB (University of Arizona Press), pp 229–239.
41. Aura Tortosa JE, Miret i Estruch C, Morales Pérez JV (2008) Coves de Santa Maira (Castell de Castells, La Marina Alta, Alacant). Campaña de 2008. *Saguntum, PLAV* 40:227–232.
42. Waters MR, Stafford TW, Redmond BG, Tankersley KB (2009) The age of the Paleoindian assemblage at Sheriden Cave, Ohio. *Am Antiq* 74(1):107–111.
43. Tankersley KB, Redmond BG (1999) Radiocarbon dating of a Paleoindian projectile point from Sheriden Cave, Ohio. *Curr Res Pleist* 16:76–77.
44. Bergin KA (2011) The Archaeology of the Talega Site (CA-ORA-907), Orange County, California: Perspective on the Prehistory of Southern California. *Viejo California Associates, Mission Viejo Prepared for the District of the US Army Corps of Engineers, Los Angeles*.
45. Goodyear AC (2013) Update on the 2012-2013 activities of the Southeastern Paleoamerican Survey. *Legacy* 17:10–12.
46. Heine K (1993) Warmzeitliche Bodenbildung im Bölling/Alleröd im Mittelrheingebiet. *Verhandlungen d Naturhistorischen Vereins der Rheinlande und Westfalens= Decheniana* 146:315–324.

47. Kromer B, Spurk M, Remmele S, Barbetti M, Joniello V (1998) Segments of Atmospheric ^{14}C Change as Derived from Late Glacial and Early Holocene Floating Tree-Ring Series. *Radiocarbon* 40(01):351–358.
48. Street MJ (1993) Analysis of Late Palaeolithic and Mesolithic Faunal Assemblages in the Northern Rhineland, Germany. Ph.D. dissertation (University of Birmingham).
49. Frechen J (1952) Die Herkunft der spätglazialen Bimstufe in mittel- und süddeutschen Mooren. *Geologisches Jahrbuch* 67:209–230.
50. Schweitzer H-J (1958) Entstehung und Flora des Trasses im nördlichen Laachersee-Gebiet. *E&G Quat Sci J* 9(1).
51. Frechen J (1959) Die Tuffe des Laacher Vulkangebietes als quartärgeologische Leitgesteine und Zeitmarken. *Fortschr Geol Rheinld u Westf* 4:363–70.
52. Baales M, Bittmann F, Kromer B (1998) Verkohlte Bäume im Trass der Laacher See-Tephra bei Kruft (Neuwieder Becken): Ein Beitrag zur Datierung des Laacher See-Ereignisses und zur Vegetation der Allerød-Zeit am Mittelrhein. *Archäol Korresp* 28(2):191–204.
53. Hedges REM, Housley RA, Ramsey CB, Klinken GJV (1993) RADIOCARBON DATES FROM THE OXFORD AMS SYSTEM: ARCHAEOOMETRY DATELIST 16. *Archaeometry* 35(1):147–167.
54. van den Bogaard P, Schmincke H-U (1985) Laacher See Tephra: A widespread isochronous late Quaternary tephra layer in central and northern Europe. *Geol Soc Am Bull* 96(12):1554.
55. Hajdas I, et al. (1993) AMS radiocarbon dating and varve chronology of Lake Soppensee: 6000 to 12000 ^{14}C years BP. *Climate Dynamics* 9(3):107–116.
56. Hajdas I, et al. (1995) Radiocarbon age of the Laacher See tephra: $11,230 \pm 40$ BP. *Radiocarbon* 37(2):149–154.
57. Rubin M, Alexander C (1960) U. S. Geological Survey Radiocarbon Dates V. *American Journal of Science Radiocarbon Supplement* 2:129–185.
58. Steegen S, Tuerlinckx F, Gelman A, Vanpaemel W (2016) Increasing Transparency Through a Multiverse Analysis. *Perspect Psychol Sci* 11(5):702–712.

J.E. Aura Tortosa, C. Miret i Estruch, J.V. Morales Pérez, Coves de Santa Maira (Castell de Castells, La Marina Alta, Alacant). Campaña de 2008. *SAGVNTVM Pap Lab Arqueol Valencia* 40, 227–232 (2008).

M. Baales, F. Bittmann, B. Kromer, Verkohlte bäume im trass Laacher See-Tephra bei Kruft. *Archäol Korres* 28, 191–204 (1998).

M. Baales, O. Jöris, M. Street, F. Bittmann, B. Weninger, J. Wiethold, Impact of the Late Glacial eruption of the Laacher See Volcano, Central Rhineland, Germany. *Quat Res* 58, 273–288 (2002).

L.C. Bement, et al., Quantifying the distribution of nanodiamonds in pre-Younger Dryas to recent age deposits along Bull Creek, Oklahoma panhandle, USA. *Proc Natl Acad Sci USA* **111**, 1726–1731 (2014).

H. Bengtsson, et al., “*matrixStats* v0.52.2: Functions that Apply to Rows and Columns of Matrices (and to Vectors)”. Github. Available at <https://github.com/HenrikBengtsson/matrixStats> (deposited 23 July 2018).

K.A. Bergin, et al., *The Archaeology of the Talega Site (CA-ORA-907), Orange County, California: Perspective on the Prehistory of Southern California*. Prepared for the District of the US Army Corps of Engineers, Los Angeles (Viejo California Associates, Mission Viejo, 2011).

A. Bevan, E.R. Crema, “*rcarbon* v1.2.0: Methods for calibrating and analyzing radiocarbon dates.” CRAN. Available at <https://CRAN.R-project.org/package=rcarbon> (deposited 1 October 2018).

E. Boaretto, et al., How reliable are radiocarbon dates? A report on the Fourth International Radiocarbon Inter-comparison (FIRI) (1998–2001). *Antiq* **77**, 146–154 (2003).

T.E. Bunch, et al., Very high-temperature impact melt products as evidence for cosmic airbursts and impacts 12,900 years ago. *Proc Natl Acad Sci USA* **109**, 1903–1912 (2012).

G. Caudullo, D. de Rigo, “*Populus tremula* in Europe: Distribution, habitat, usage and threats” in *European Atlas of Forest Tree Species*, J. San-Miguel-Ayanz, D. de Rigo, G. Caudullo, T. Houston, A. Mauri, Eds. (Publication Office of the European Union, 2016), pp. 138–139.

R.B. Firestone, et al., Evidence for an extraterrestrial impact 12,900 years ago that contributed to the megafaunal extinctions and the Younger Dryas cooling. *Proc Natl Acad Sci USA* **104**, 16016–16021 (2007).

J. Frechen, Die Herkunft der spätglazialen Bimstufe in mittel- und süddeutschen Mooren. *Geol Jahrb* **67**, 209–230 (1952).

J. Frechen, Die Tuffe des Laacher Vulkangebietes als quartärgeologische Leitgesteine und Zeitmarken. *Fortschritte der Geol Rheinl Westfal* **4**, 363–370 (1959).

A.C. Goodyear, Update on the 2012–2013 activities of the Southeastern Paleoamerican Survey. *Leg* **17**, 10–12 (2013).

I. Hajdas, et al., AMS radiocarbon dating and varve chronology of Lake Soppensee: 6000 to 12000 14C years BP. *Clim Dyn* **9**, 107–116 (1993).

I. Hajdas, et al., Radiocarbon age of the Laacher See Tephra: $11,230 \pm 40$ BP. *Radiocarb* **37**, 149–154 (1995).

E.R. Hajic, R.D. Mandel, J.H. Ray, N.H. Lopinot, Geoarchaeology of stratified Paleoindian deposits at the Big Eddy site, southwest Missouri, USA. *Geoarchaeol* **22**, 891–934 (2007).

C.V. Haynes, Jr., “Radiocarbon dating at Murray Springs and Curry Draw” in *Murray Springs: A Clovis Site with Multiple Activity Areas in the San Pedro Valley, Arizona*, C.V. Haynes, Jr., B.B. Huckell, Eds. (University of Arizona Press, 2007), pp. 229–239.

V. Haynes, G. Agogino, G., *Geological Significance of a New Radiocarbon Date from the Lindenmeier Site*. Proc Denver Mus Nat Hist No. 9 (Denver Museum of Natural History, 1960).

R.E.M. Hedges, R.A. Housley, C. Bronk Ramsey, G.J. v. Klinken, Radiocarbon dates from the Oxford AMS system: *Archaeometry Datalist 16*. *Archaeom* **35**, 147–167 (1993).

K. Heine, Warmzeitliche Bodenbildung im Bölling/Alleröd im Mittelrheingebiet. *Verh Naturhist Ver Rheinl Westfal-Dechen* **146**, 315–324 (1993).

International Study Group, An inter-laboratory comparison of radiocarbon measurements in tree rings. *Nat* **298**, 619–623 (1982).

E. Johnson, V.T. Holliday, Analysis of Paleoindian bonebeds at the Clovis Site: New data from old excavations. *Plains Anthropol* **42**, 329–352 (1997).

C.R. Kinzie, et al., Nanodiamond-rich layer across three continents consistent with major cosmic impact at 12,800 Cal BP. *J Geol* **122**, 475–505 (2014).

B. Kromer, M. Spurk, S. Remelle, M. Barbetti, V. Toniello, Segments of atmospheric ^{14}C change as derived from late Glacial and early Holocene floating tree-ring series. *Radiocarb* **40**, 351–358 (1998).

N.H. Lopinot, J.H. Ray, M.D. Conner, *The 1997 Excavations at the Big Eddy Site (23CE426) in Southwest Missouri*. Cen Archaeol Res Spec Pub No. 2. (Southwest Missouri State University, 1998).

N.H. Lopinot, J.H. Ray, M.D. Conner, *The 1999 Excavations at the Big Eddy Site (23CE426)*. Cen Archaeol Res Spec Pub No. 3. (Southwest Missouri State University, 2000).

D.J. Kennett, et al., Wildfire and abrupt ecosystem disruption on California's Northern Channel Islands at the Ållerød-Younger Dryas boundary (13.0–12.9 ka). *Quat Sci Rev* **27**, 2530–2545 (2008).

J.P. Kennett, et al., Bayesian chronological analyses consistent with synchronous age of 12,835–12,735 Cal B.P. for Younger Dryas boundary on four continents. *Proc Natl Acad Sci USA* **112**, 4344–4353 (2015).

L. McDonald, D. Chivall, D. Miles, C. Bronk Ramsey, Seasonal variations in the ^{14}C content of tree rings: Influences on radiocarbon calibration and single-year curve construction. *Radiocarb* DOI:10.1017/RDC.2018.64 (2018).

R. McElreath, “*rethinking* v1.59: Statistical Rethinking book package”. Github. Available at <https://www.github.com/user/rmcclreath/rethinking> (deposited 24 June 2016).

A.M.T. Moore, G.C. Hillman, A.J. Legge, J. Huxtable, *Village on the Euphrates: from foraging to farming at Abu Hureyra* (Oxford University Press, 2000).

T.L. Pedersen, “*patchwork* v0.0.1: The Composer of ggplots”. Github. Available at <https://github.com/thomasp85/patchwork> (deposited 22 September 2018).

R Core Team, “*parallel* v3.5.2.” R Project for Statistical Computing. Available at <https://www.r-project.org/> (deposited 20 December 2018).

P.J. Reimer, et al., IntCal13 and Marine13 radiocarbon age calibration curves 0–50,000 years cal BP. *Radiocarb* **55**, 1869–1887 (2013).

M. Rubin, C. Alexander, U. S. Geological Survey Radiocarbon Dates V. *Radiocarb* **2**, 129–185 (1960).

H.-J. Schweitzer, Entstehung und flora des trasses im nördlichen Laachersee-gebiet. *E&G – Quat Sci J* **9**, 28–48 (1958).

E.M. Scott, T.C. Aitchison, D.D. Harkness, G.T. Cook, M.S. Baxter, An overview of all three stages of the International Radiocarbon Intercomparison. *Radiocarb* **32**, 309–319 (1990).

E.M. Scott, D.D. Harkness, G.T. Cook, Interlaboratory comparisons: lessons learned. *Radiocarb* **40**, 331–340 (1998).

- E.M. Scott, G.T. Cook, P. Naysmith, Error and uncertainty in radiocarbon measurements. *Radiocarb* **49**, 427–440 (2007a).
- E.M. Scott, G. Cook, P. Naysmith, The Fifth International Radiocarbon Intercomparison (VIRI): An assessment of laboratory performance in Stage 3. *Radiocarb* **53**, 859–865 (2010a).
- E.M. Scott, G. Cook, P. Naysmith, A report on Phase 2 of the Fifth International Radiocarbon Intercomparison (VIRI). *Radiocarb* **52**, 846–858 (2010b).
- E.M. Scott, G.T. Cook, P. Naysmith, C. Bryant, D. O'Donnell, A report on Phase 1 of the 5th International Radiocarbon Intercomparison (VIRI). *Radiocarb* **49**, 409–426 (2007b).
- Stan Development Team (2018), “RStan 2.17.2: The R interface for Stan.” Github. Available at <https://github.com/stan-dev/rstan/releases> (deposited 20 December 2017).
- S. Steegen, F. Tuerlinckx, A. Gelman, W. Vanpaemel, Increasing transparency through a multiverse analysis. *Perspect Psychol Sci* **11**, 701–712 (2016).
- M.J. Street, *Analysis of Late Palaeolithic and Mesolithic Faunal Assemblages in the Northern Rhineland, Germany*. Ph.D. dissertation (University of Birmingham, 1993).
- K.B. Tankersley, B.G. Redmond, Radiocarbon dating of a Paleoindian projectile point from Sheriden Cave, Ohio. *Curr Res Pleistocene* **16**, 76–77 (1999).
- P. van den Bogaard, H.-U. Schmincke, Laacher See Tephra: A widespread isochronous late Quaternary tephra layer in central and northern Europe. *Geol Soc Am Bull* **96**, 1554–1571 (1985).
- B. van Geel, G.R. Coope, T. van der Hammen, Palaeoecology and stratigraphy of the late glacial type section at Usselo (The Netherlands). *Rev Palaeobot Palynol* **60**, 25–129 (1989).
- A. van Hoesel, et al., Nanodiamonds and wildfire evidence in the Usselo horizon postdate the Allerød-Younger Dryas boundary. *Proc Natl Acad Sci USA* **109**, 7648–7653 (2012).
- G. von Wühlisch, EUFORGEN Technical Guidelines for Genetic Conservation and use of Urasian Aspen (*Populus tremula*) (Biodiversity International, 2009).
- A. Walton, M.A. Trautman, J.P. Friend, Isotopes, Inc. Radiocarbon Measurements I. *Radiocarb* **3**, 47–59 (1961).
- Y. Wang, R. Amundson, S. Trumbore, Radiocarbon dating of soil organic matter. *Quat Res* **45**, 282–288 (1996).
- M.R. Waters, T.W. Stafford, B.G. Redmond, K.B. Tankersley, The age of the Paleoindian assemblage at Sheriden Cave, Ohio. *Am Antiq* **74**, 107–111 (2009).
- H. Wickham, “reshape2 1.4.3: Flexibly Reshape Data: A Reboot of the Reshape Package.” CRAN. Available at <https://cran.r-project.org/web/packages/reshape2/index.html> (deposited 11 December 2017).
- H. Wickham, et al., “ggplot2 v3.1.0: Create Elegant Data Visualisations Using the Grammar of Graphics.” CRAN. Available at <https://cran.r-project.org/web/packages/ggplot2/index.html> (deposited 25 October 2018).
- J.H. Wittke, et al., Evidence for deposition of 10 million tonnes of impact spherules across four continents 12,800 y ago. *Proc Natl Acad Sci USA* **110**, 2088–2097 (2013).